The *Suzaku* Technical Description

Version: October, 2012

Announcement of Opportunity #8

Institute of Space and Astronautical Science (ISAS/JAXA)
and the
X-ray Astrophysics Laboratory
NASA/Goddard Space Flight Center

Copies of this guide are available in `html`, `postscript` and `pdf` formats.

Contents

1 Introduction **2**

2 Changes Since AO-7 **5**

3 Mission Description **8**

3.1 Brief Introduction to *Suzaku* 8

3.2 Operational Constraints 13

3.2.1 Telemetry Rates 13

3.2.2 Summary 14

3.3 Calibration 14

4 Observation Policies **16**

4.1 Data Rights 17

4.2 Target of Opportunity Proposals 18

4.3 Pointing Constraints 18

4.4 Events After Submission 20

5 Writing A Successful *Suzaku* Proposal **22**

5.1 First Checks 22

5.1.1 `Viewing` 22

5.1.2 Previous Observations 22

5.2 Proposal Ingredients 23

5.3 `PIMMS` & `WebPIMMS` 23

5.4 `XSPEC` Simulations 24

5.4.1 WebSPEC Simulations . . . 24
5.5 Examples . . . 25
5.5.1 Faint Oxygen Emission from the Local Hot Bubble . . . 25
5.5.2 Hard Tails of XRBs . . . 26
5.6 XISSIM . . . 40
5.7 MAKI . . . 41
5.8 RPS . . . 41
5.9 Checklist . . . 42
5.10 Additional Requirements for US Proposers . . . 43

6 X-Ray Telescopes (XRT) 44
6.1 Basic XRT Components . . . 44
6.1.1 Reflectors . . . 46
6.1.2 Pre-Collimator . . . 47
6.1.3 Thermal Shields . . . 48
6.2 In-Flight Performance . . . 49
6.2.1 Focal Positions . . . 49
6.2.2 Optical Axis . . . 49
6.2.3 Effective Area . . . 51
6.2.4 Vignetting . . . 54
6.2.5 Angular Resolution . . . 58
6.2.6 Stray Light . . . 62

7 X-Ray Imaging Spectrometer (XIS) 70
7.1 XIS Overview . . . 70
7.1.1 XIS Basics . . . 70
7.1.2 XIS Components . . . 72
7.1.2.1 Sensors . . . 72
7.1.2.2 Cooling System . . . 74
7.1.2.3 Electronics . . . 74
7.1.3 CCD Pixels & Coordinates . . . 74
7.1.4 Major Events . . . 75

7.2 XIS Observation Planning . . . 77
7.2.1 User Options . . . 77
7.2.1.1 Clocking Modes . . . 78
7.2.1.2 Editing Modes . . . 81
7.2.1.3 PPU Ratio . . . 82
7.2.1.4 Lower Event Threshold . . . 83
7.2.1.5 Area Discrimination . . . 83
7.2.2 Systematic Observational Effects and their Mitigation . . . 84
7.2.2.1 Photon Pile-Up . . . 84
7.2.2.2 Telemetry Saturation . . . 86
7.2.2.3 Out-Of-Time Events . . . 88
7.2.2.4 Self Charge Filling . . . 89
7.3 XIS Performance & Calibration . . . 91
7.3.1 Spaced-Row Charge Injection (SCI) . . . 91
7.3.1.1 CTI Monitoring & Trend . . . 91
7.3.1.2 SCI Operations History . . . 92
7.3.1.3 SCI Notes for Users & Proposers . . . 93
7.3.2 Energy Gain and Resolution . . . 94
7.3.2.1 Energy Calibration Results (1) — Normal Mode (No Options) 94
7.3.2.2 Energy Calibration Results (2) — Other Clocking Modes . 99
7.3.2.3 Energy Calibration Results (3) — Other Editing Modes . . 104
7.3.2.4 Energy Calibration Notes for Users & Proposers . . . 104
7.3.3 Contamination & Low Energy Quantum Efficiency Degradation . . . 106
7.3.3.1 Contamination Calibration Results . . . 106
7.3.3.2 Contamination Notes for Users & Proposers . . . 110
7.3.4 Non X-Ray Background . . . 112
7.3.4.1 NXB Calibration Results . . . 112
7.3.4.2 NXB Notes for Users & Proposers . . . 113
7.3.5 Flux Calibration . . . 117
7.3.6 Putative Micro-Meteorite Hits . . . 117
7.4 XIS Onboard Processing . . . 119

7.4.1 Pulse Height Determination & Hot Pixel Rejection 119
7.4.2 On-Board Event Analysis 120
7.4.3 Discriminators 121

8 Hard X-Ray Detector (HXD) 123
8.1 GSO/BGO Counter Units 125
8.2 PIN-Si Diodes 125
8.3 HXD Field of View 126
8.4 In-Orbit HXD Background 126
8.5 Background Modeling 129
8.5.1 PIN Background Model 130
8.5.1.1 Modeling Methods 130
8.5.1.2 Comparison With Sky Data 130
8.5.2 GSO Background Model 132
8.5.2.1 Modeling Methods 132
8.5.2.2 Comparison With Dark Objects 132
8.5.3 Theoretical Sensitivity 132
8.6 Data Analysis Procedure 133
8.7 Wide-Band All-Sky Monitor (WAM) 133

A Acronyms 137

B Important Web/E-Mail Addresses 141

List of Figures

3.1 The 96 minute *Suzaku* orbit. 9

3.2 [Left] Schematic picture of the bottom of the *Suzaku* satellite. [Right] A side view of the instrument and telescopes on *Suzaku*. 9

3.3 XIS effective area of one XRT + XIS system, for both the FI and BI chips.(No contamination included.) 10

3.4 The Encircled Energy Function (EEF) showing the fractional energy within a given radius for one quadrant of the XRT-I telescopes on *Suzaku* at 4.5 and 8.0 keV. 12

3.5 Total effective area of the HXD detectors, PIN and GSO, as a function of energy. 13

5.1 Simulation of an HXD observation of a 10 mCrab source with a Crab-like spectrum. Here, the cornorm of the two background files has been set to 0. 37

5.2 Simulation with the highest estimated background, for both the PIN and the GSO. 38

5.3 Simulation with the lowest estimated background, for both the PIN and the GSO. 40

6.1 Layout of the XRTs on the *Suzaku* spacecraft. 45

6.2 A *Suzaku* X-ray telescope. 46

6.3 A thermal shield. 48

6.4 Focal positions on the XISs when the satellite points at MCG−6-30-15 using the XIS aim point. 49

6.5 Locations of the optical axis of each XRT-I module in the focal plane determined from the observations of the Crab nebula in 2005 August–September. This figure implies that the image on each XIS detector becomes brightest when a target star is placed at the position of the corresponding cross. The dotted circles are drawn every $30''$ in radius from the XIS-default position (see text). 50

6.6 The source- and background-integration regions overlaid on the Crab images taken with XIS1 at the XIS-default position (left) and the HXD-default position (right) on 2005 September 15–16. The images are elongated in the frame-transfer direction due to the out-of-time events (see text). In order to cancel these events, the background regions with a size of 126 by 1024 pixels each are taken at the left and right ends of the chip for the XIS-default position, and a single region with a size of 252 by 1024 pixels is taken at the side far from the Crab image for the HXD-default position. The remaining source-integration region has a size of 768 by 1024 pixels, or $13'.3 \times 17'.8$. The background subtraction is carried out after area-size correction. 51

6.7 Power-law fit to the Crab spectra of all four XIS modules taken at the XIS-default position. All the parameters are allowed to vary independently for each XIS module. The fit is carried out in the 1.0–10.0 keV band, excluding the 1.5–2.0 keV interval where large systematic uncertainties associated with the Si K-edge remain. This energy range is retrieved after the fit. 53

6.8 Count rates of the Crab pointings offset in DETX (left) and DETY (right) in the 2–10 keV band. Red and green symbols correspond to the data during 2005 and 2006, respectively. The solid line corresponds to the output of the ray-tracing simulator `xissim`. The bottom panels show the ratios of the data to the simulator output. 55

6.9 The same as Fig.6.8 but in the 3–6 keV band. 56

6.10 The same as Fig.6.8 but in the 8–10 keV band. 57

6.11 Images of the four XRT-I modules in the focal plane: SS Cyg (left) and simulation (right). All the images are binned to 2×2 pixels and then smoothed with a Gaussian with a sigma of 3 pixels, where the pixel size is 24 μm. The Fe55 events were removed from the SS Cyg image. 59

6.12 PSF of the four XRT-I images. The lower panels show the ratio between the observed and simulated data. 60

6.13 EEF of the four XRT-I images. The EEF is normalized to unity at the edge of the CCD chip (a square of $17'.8$ on the side). The lower panels show the ratio between the observed and simulated data. 61

6.14 Focal plane images formed by stray light. The left and middle panels show simulated images of a monochromatic point-like source of 4.51 keV located at $(-20', 0')$ in (DETX, DETY) without and with the pre-collimator, respectively. The radial dark lanes are the shadows of the alignment bars. The right panel is the in-flight stray image of the Crab nebula in the 2.5–5.5 keV energy band located at the same off-axis angle. The unit of the color scale of this panel is counts per 16 pixels over the entire exposure time of 8428.8 s. The count rate from the whole image is 0.78 ± 0.01 counts s^{-1} including background. Note that the intensity of the Crab nebula measured with XIS3 at the XIS-default position is 458 ± 3 counts s^{-1} in the same 2.5–5.5 keV band. All images are binned to 2×2 pixels and then smoothed with a Gaussian with a sigma of 2 pixels, where the pixel size is 24 μm. 62

6.15 Mosaic images of offset observations of the Crab taken in 2005. 64

6.16 Same as figure 6.15, but taken in 2010. 65

6.17 Angular responses of the XRT-I at 1.5 (left) and 4.5 keV (right) up to 2°. The effective area is normalized to 1 at the on-axis position. The integration area is corresponding to the detector size of the XISs ($17.'8 \times 17.'8$). The four solid lines in the plots correspond to different detector IDs. The crosses are the normalized effective area using the Crab pointings. 66

6.18 Stray patterns for a stray source at an azimuth angle of α and an offset angle of R. 68

6.19 Pointing positions targeting the three kinds of stray light free regions: the "Quadrant Boundary" region (top), the "Secondary-reflection component free" region (middle) and the "Backside component free" region (bottom). . 69

7.1 Photo of an XIS sensor 71

7.2 XIS field of view 72

7.3 Schematic view of the data flow in one XIS unit. 73

7.4 Time sequence of the exposure, transfer, and readout 79

7.5 Data pattern for 5×5, 3×3, and 2×2 editing modes 82

7.6 Incident versus observed count rates for a point-like source 85

7.7 Image of out-of-time events 88

7.8 Frame data with SCI 91

7.9 Trend of ^{55}Fe peak height and width 92

7.10 Gain in the hard band for the Normal mode (without options) 95

7.11 Energy resolution in the hard band for the Normal mode (without options) 96

7.12 Gain in the soft band for the Normal mode (without options) 97
7.13 Energy resolution in the soft band for the Normal mode (without options) . 98
7.14 Gain for the window option (XIS0) 99
7.15 Gain for the window option (XIS1) 100
7.16 Gain for the window option (XIS3) 100
7.17 Gain and resolution for the burst option 101
7.18 History of the P-sum gain. 102
7.19 History of the P-sum energy resolution. 103
7.20 Gain for the 2×2 editing mode. 105
7.21 Chemical composition of the contaminant 106
7.22 Time dependence of the thickness of the C contaminant 107
7.23 Time dependence of the thickness of the N contaminant 108
7.24 Time dependence of the thickness of the O contaminant 108
7.25 Time dependence of the thickness of the total contaminant 109
7.26 Spatial dependence of the thickness of the contaminant 110
7.27 Fit results using the 2012 contamination model 111
7.28 XIS non X-ray background (NXB) spectra 112
7.29 Cut-off rigidity dependence of the NXB. 114
7.30 ACTY dependence of the NXB 115
7.31 Soft NXB increase in XIS1 116
7.32 Relative normalization between different XIS sensors. 117
7.33 Definition of grades in the P-Sum/Timing mode. 121

8.1 The Hard X-ray Detector before installation. 123
8.2 Schematic picture of the HXD instrument, which consists of two types of detectors: the PIN diodes located in the front of the GSO scintillator, and the scintillator itself. 124
8.3 Angular response of a single fine-collimator along the satellite X-axis, obtained from offset observations of the Crab nebula. 127
8.4 [Left] Comparison of average non X-ray background spectra of the PIN, obtained in various epochs. The Crab spectrum, scaled down by two orders of magnitude, is shown as well. [Right] Evolution of average GSO-NXB spectra. 127

8.5 Comparison of the in-orbit detector background of the PIN/GSO, normalized by the individual effective areas, with that of the *RXTE*-PCA, *RXTE*-HEXTE, and *BeppoSAX*-PDS. Dotted lines indicate 1 Crab, 100 mCrab, and 10 mCrab intensities. 128

8.6 [Left] Light curve of the non X-ray background of the PIN, folded with the elapsed time after the SAA passage (*top*), and the average cut-off rigidity at the corresponding position (*bottom*). [Right] The same folded light curves for the GSO background, in the 40–90, 260–440, and 440-700 keV energy bands. 129

8.7 Comparison between the data and the NXB model count rate of sky observations with 10 ks integration time in the 15–40 keV band. Observations with no apparent hard X-ray objects in the XIS FOV were selected (see text for details of the data selection). 130

8.8 The same as Figure 8.7, but for observations of E0102-72 (black) and the Cygnus LOOP (red). 131

8.9 Comparison between the measured PIN spectra (black) and the PIN NXB model spectra (red) for observations of objects with no strong hard X-ray contribution. Their fractional residuals are given by purple crosses in the bottom panel of each figure. The blue and green histograms in the top panel indicate the background-subtracted spectrum and the typical CXB spectrum (Boldt 1987), respectively. 134

8.10 Comparison of the GSO spectra between the data (black) and BGD model (red) for observations of objects with no known strong hard X-rays. Their fractional residuals are given by blue crosses. 135

8.11 Calculated detection limits of the HXD, for continuum measurements. The solid lines denote the statistical 3σ limit for a 100 ks exposure, while the dashed lines show the assumed systematic uncertainties of 3% and 1.5% for the PIN- and GSO-NXB modeling, respectively. 136

List of Tables

3.1 Overview of *Suzaku* capabilities. 11

3.2 Error Budgets of Scientific Instrument Calibrations. 15

4.1 *Suzaku* time allocated to each group of observers. The ESA time is in parentheses as it is part of the Japanese allotment. 17

6.1 Telescope dimensions and parameters of XRT-I. 45

6.2 Design parameters for the pre-collimator. 48

6.3 Best-fit parameters of the power law model fits to the Crab spectra taken on 2005 September 15–16. 52

6.4 Best-fit parameters of the contemporaneous power-law fits to the Crab spectra taken in 2005 September 15–16. 54

7.1 Operation history 76

7.2 Clocking modes 78

7.3 Window and burst options (XIS nominal position) 80

7.4 Editing modes and size per event for observation modes 81

7.5 Combination of editing modes and PPU ratio 83

7.6 Event threshold 83

7.7 Total count rate (s^{-1}) to cause the indicated pile-up fraction as a function of PSF radius. 86

7.8 Telemetry allocation for XIS 87

7.9 Incoming rate to cause telemetry saturation (s^{-1}) 87

7.10 Routine calibration observations and their usage. 90

7.11 Strength of emission lines in the NXB spectrum 113

7.12 Relative normalization among different sensors. 117

Chapter 1

Introduction

Suzaku is the fifth in the series of Japanese astronomy satellites devoted to observations of celestial X-ray sources, following the highly successful Hakucho, Tenma, Ginga and *ASCA* satellites. Like *ASCA*, *Suzaku* is a joint Japanese-US mission, developed by the Institute of Space and Astronautical Science (part of the Japan Aerospace Exploration Agency, ISAS/JAXA) in collaboration with the National Aeronautics and Space Administration's Goddard Space Flight Center (NASA/GSFC) and many other institutions. *Suzaku* was launched on a Japanese M-V rocket on July 10, 2005 from the JAXA Uchinoura Space Center (USC). Despite initial success, on August 8, 2005 a thermal short between the helium and neon tanks resulted in the liquid helium coolant venting to space, leaving the X-Ray Spectrometer (XRS) inoperable. However, the X-ray Imaging Spectrometer (XIS) and Hard X-ray Detector (HXD) are all working well. As a result, *Suzaku* retains its excellent X-ray sensitivity, with high throughput over a broad-band energy range of 0.2 to 600 keV. *Suzaku*'s broad bandpass, low background, and good CCD resolution makes it a unique tool capable of addressing a variety of outstanding problems in astrophysics.

Guest observing time on *Suzaku* will be awarded on a competitive basis and proposals will be judged on their scientific merits and their relevance to *Suzaku* observing capabilities. The overall purpose of this document is to aid potential users of *Suzaku* in proposing for time during the Guest Observer (GO) phase of the mission. In particular, upon reading this document, the proposer should be able to determine whether or not *Suzaku* is best suited to conduct the investigation in question. This should be demonstrated in the proposal, preferably using simulations of the proposed observations. All proposals should clearly answer the following four questions:

1. Is *Suzaku* capable of the proposed observation?
2. Is it the best available instrument for the investigation?
3. When can *Suzaku* observe a given source?

4. How much exposure time is required to meet the scientific goals?

Chapter 2 lists the principal changes since the last AO. Chapter 3 summarizes the principal characteristics of the detectors on-board *Suzaku*. Chapter 4 covers how the satellite time will be allocated. This includes the data rights and available time for GOs, as well as policies regarding Targets of Opportunity (TOOs). In addition, observational constraints due to the orbit, sun angle, and the pointing accuracy are described. Finally, the proposal process is reviewed, including how to submit a proposal, how they will be evaluated, and how observations will be scheduled, performed, and the results disseminated. US proposers should note especially the NASA requirements regarding the relevance of the proposed science to NASA's mission.

Chapter 5 explains how to write a strong proposal, including a summary of what constraints must be met, and what must be included in the proposal. In most cases, existing X-ray data can be used to estimate the likely *Suzaku* count rates. Simulation tools, including **XSPEC** and **PIMMS**, will assist in this and are covered in detail with examples.

The last three chapters describe the telescopes and instruments on *Suzaku*. Chapter 6 covers the five X-ray Telescopes (XRTs) on *Suzaku*. Chapter 7 reviews the X-ray Imaging Spectrometers (XISs), four CCDs with moderate spectral resolution and a large field of view. Chapter 8 explains the operation of the Hard X-ray Detector (HXD), which extends the high energy bandpass of *Suzaku* to 600 keV.

Disclaimer:

This document was prepared using the best current knowledge of the *Suzaku* satellite by the *Suzaku* teams at ISAS/JAXA and NASA/GSFC as of October 2012. It is possible that information contained in this document may contain inadvertent errors or omissions. We welcome suggestions for corrections or clarifications. Revisions of this document will be available on the *Suzaku* Web sites listed in Appendix B. Users interested in more details can also access the different instrument papers available at the web-site specified below. Please note that these papers have also been published in the special issue number 1, vol. 59 of the Publications of the Astronomical Society of Japan.

1. Spacecraft paper:
   `ftp://legacy.gsfc.nasa.gov/suzaku/doc/general/suzakumemo-2006-33.pdf`
2. XRT paper:
   `ftp://legacy.gsfc.nasa.gov/suzaku/doc/xrt/suzakumemo-2006-34.pdf`
3. XIS instrument paper:
   `ftp://legacy.gsfc.nasa.gov/suzaku/doc/xis/suzakumemo-2006-35.pdf`
4. XIS simulations paper:
   `ftp://legacy.gsfc.nasa.gov/suzaku/doc/xis/suzakumemo-2006-39.pdf`

5. HXD instrument paper:
   `ftp://legacy.gsfc.nasa.gov/suzaku/doc/hxd/suzakumemo-2006-36.pdf`
6. HXD in-flight performance paper:
   `ftp://legacy.gsfc.nasa.gov/suzaku/doc/hxd/suzakumemo-2006-37.pdf`

Chapter 2

Changes Since AO-7

This page summarizes the main changes to the *Suzaku* Technical Description since the last AO and *re-emphasizes* several important issues to consider for the preparation of proposals. Please note that this **should not prevent the user to carefully read the new version of the Technical Description**.

New:

1. The total time nominally available for observations to the community is again 11902 ks in AO-8 (11902 ks in AO-4 to AO-7, 12038 ks in AO-3, 11722 ks in AO-2). 2 Ms will be used for continuing Key projects, accepted in or before AO-7; any remaing time will be added to the Joint Japan-US time. 5451 ks are assigned to Japanese observations, this includes 909 ks for proposals submitted to ESA as joint Japan-ESA observations, and 3963 ks go to US observations. The remaining 488 ks are foreseen for joint Japan-US investigations.

2. Every possible measure to enable normal observations through the end of the AO-8 period (2014 March 31) will be taken, but still the operation of a subset of the instruments might have to be stopped if the power shortage becomes serious enough. Further degradation of the power supply may even lead to premature termination of AO-8. A simple extrapolation of the power history implies that a partial shutdown of the scientific instruments should be considered around early 2014. However, this estimate depends on the radiation environment on orbit, such as the activity level of the Sun.

3. Given this, all new Cycle 8 proposals should stand on their own merits, in the sense of not requiring future (Cycle 9) *Suzaku* observations.

4. Previously, targets with Sun angles in the range 65 to 110 degrees were accessible for *Suzaku* observations. Considering the power situation, **the Sun angle range will be restricted to 70–110 degrees** for AO-8 observations.

5. It is conceivable that the amount of time available for target-of-opportunity and time critical observations will have to be reduced.

6. The Key Project proposal category was introduced in AO-4 for comprehensive observing programs sampling a number of objects of a particular class or surveying a large region of the sky, in order to take maximal advantage of the unique attributes of *Suzaku* to address important astrophysical problems. **While no new Key Project proposals will be solicited in AO-8** given the power supply degradation, the project team decided to **concentrate on completing Key Projects that have been accepted in previous cycles**.

Reminders:

1. The category of "Long Program" for proposals with a total exposure time >300 ks, available in (only) the US from AO-3 to AO-6 has not been offered since AO-7 anymore.

2. As before all projects with total exposure times equal to or more than 300 ks are open to the public immediately.

3. Regular US proposals may request no more than 1 Ms of observing time for practical reason (ISAS/JAXA proposals may not exceed total exposure times of 400 ks). Note that for TOO proposals this 1 Ms limit applies to the actually requested observing time. It is therefore possible to request 400 ks per target for up to 2 triggers among 5 potential targets, for example.

4. Since AO-5, individual raster scan observations have to have the same minimum exposure time of 10 ks per pointing as other observations.

5. XIS1 suffered a micro-meteorite hit in December 2009. Following diagnostic measurements showed that the scientific impact is minimal. See section 7.3.6 for more information about previous micrometeorite hits and their effects.

6. The use of the HXD nominal aim point is discouraged. To this end the HXD team will no longer provide response matrices for simulation for observations at the HXD nominal aim point. The XIS team will no longer support observations at the HXD nominal aim point that use the P-sum mode, the Window option or the Burst option.

7. Two *Suzaku* memos provide information about the jitter of the pointing direction that can affect observations since the end of 2009 (`ftp://legacy.gsfc.nasa.gov/suzaku/doc/general/suzakumemo-2010-05.pdf` and `ftp://legacy.gsfc.nasa.gov/suzaku/doc/general/suzakumemo-2010-06.pdf`). Note that the first one describes an effect – the observed light curves being modulated due to telescope vignetting – that is mitigated by not using the HXD aim point.

8. Proposals using the P-sum/Timing mode of the XIS are encouraged. There is no longer a limit on the amount of P-sum/Timing mode observations that can be accepted. Proposers should be aware of the properties of the P-sum/Timing mode. Photon pile-up scarcely occurs in this mode, and a time resolution as fast as 7.8 ms can be achieved, but only a 1-dimensional image can be obtained. Note that the P-sum/Timing mode can be adopted only for the XIS3, and neither the Spaced-row Charge Injection nor a CTI correction can be applied. The energy resolution is therefore significantly worse than in the normal imaging mode. The calibration accuracy is not as good as that for the normal imaging mode, either.

9. XIS recipes for P-sum data reduction and pile-up detection have been released which are useful for planning observations requiring high time resolution and pile-up mitigation. Please see `http://www.astro.isas.jaxa.jp/suzaku/analysis/xis/`.

10. For feasibility studies of HXD data analyses proposers should simulate observations with the responses and background files provided for the XIS aim point, then analyze them by varying the background by typically $\pm 3\%$ for the PIN and $\pm 1.5\%$ for the GSO. This procedure mimics the level of systematic uncertainties in the current HXD background models (see sections 5.5.2 and 8.5). The background files were generated based on the Lockman hole observation performed on 2009-06-12. The PIN threshold of Epoch 9 has been applied. Channels below 15 keV should be ignored due to uncertainties in the response and background. As long as this is done, simulations based on these files are suitable for simulating AO-8 observations.

11. Note that the *Suzaku* project has an agreement with the *Fermi* project as well as with the *Chandra* project to make a modest amount of *Suzaku* time available for allocation through their proposal review processes for investigations that take advantage of joint observations. See *Chandra* and *Fermi* calls for proposals for further details.

12. Real-time TOO proposals (outside the AO process, through `http://www.astro.isas.jaxa.jp/suzaku/planning/gtoo/`) for gamma-ray bursts can be submitted by all investigators, including those who are not part of the *Suzaku* science working group.

Chapter 3

Mission Description

This chapter is a brief introduction to the satellite and its instruments and is intended as a simplified guide for the proposer. Reading it thoroughly should provide the reader with the necessary information to understand the capabilities of the instruments at a level sufficient to prepare the feasibility section of a *Suzaku* proposal.

In its first four years of operation, *Suzaku* has accumulated data from calibration, SWG and GO observations. The list of all observations performed is available in the Browse master catalog at the High Energy Astrophysics Science Archive Research Center (HEASARC) at `http://heasarc.gsfc.nasa.gov/cgi-bin/W3Browse/w3browse.pl` and at `http://suzaku.gsfc.nasa.gov/docs/suzaku/aehp_time_miss.html`.

Suzaku is in many ways similar to *ASCA* in terms of orbit, pointing, and tracking capabilities. *Suzaku* uses the same station (USC) as *ASCA* did for up-link and down-link, although down-link at NASA DSN is not possible with *Suzaku* (see footnote in subsection 3.2.1). As a result, the operational constraints for *Suzaku* are also similar to those of *ASCA*. *Suzaku* is placed in a near-circular orbit with an apogee of 568 km, an inclination of 31.9 degrees, and an orbital period of about 96 minutes. The maximum slew rate of the spacecraft is 6 degrees/min, and settling to the final attitude takes $\sim$ 10 minutes, using the star trackers. The normal mode of operations will have the spacecraft pointing in a single direction for at least 1/4 day (10 ks net exposure time). With this constraint, most targets will be occulted by the Earth for about one third of each orbit, but some objects near the orbital poles can be observed nearly continuously. The observing efficiency of the satellite as measured after four years of operation is about 45%.

3.1 Brief Introduction to *Suzaku*

The scientific payload of *Suzaku* (Fig. 3.2) initially consisted of three distinct co-aligned scientific instruments. There are four X-ray sensitive imaging CCD cameras (X-ray Imag-

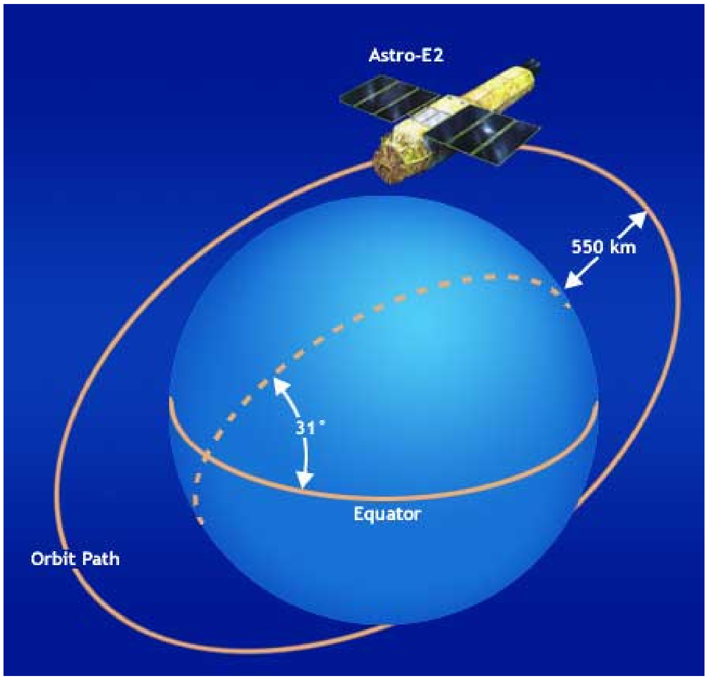

Figure 3.1: The 96 minute *Suzaku* orbit.

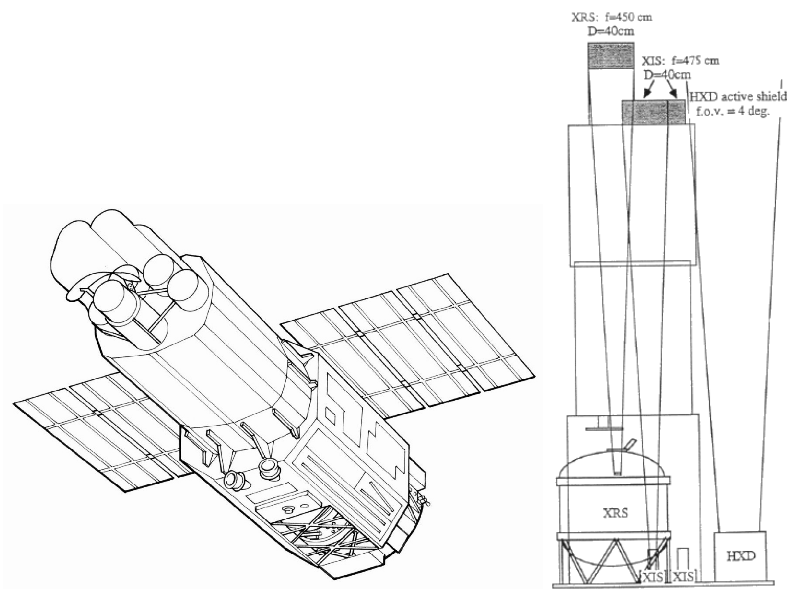

Figure 3.2: [Left] Schematic picture of the bottom of the *Suzaku* satellite. [Right] A side view of the instrument and telescopes on *Suzaku*.

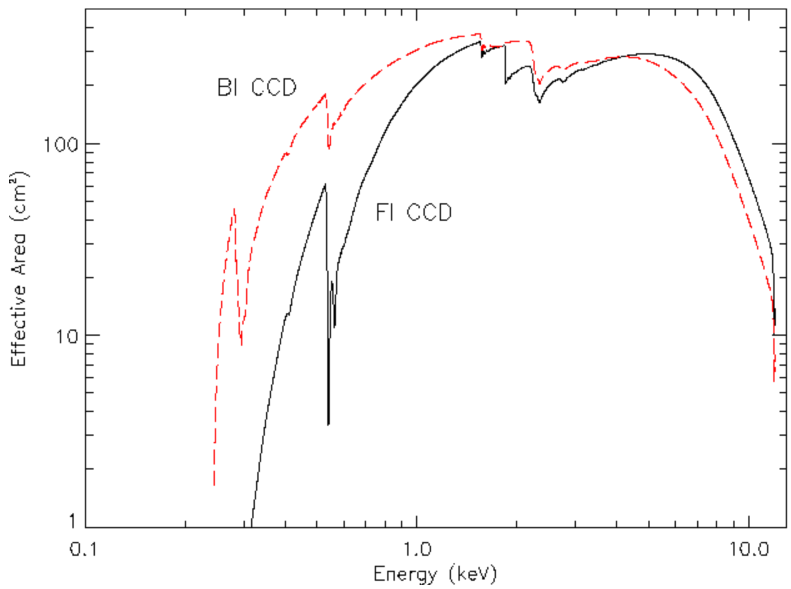

Figure 3.3: XIS effective area of one XRT + XIS system, for both the FI and BI chips.(No contamination included.)

ing Spectrometers, or XISs), three front-illuminated (FI; energy range 0.4–12 keV) and one back-illuminated (BI; energy range 0.2–12 keV), capable of moderate energy resolution. Each XIS is located in the focal plane of a dedicated X–ray telescope. The second instrument is the non-imaging, collimated Hard X-ray Detector (HXD), which extends the bandpass of the observatory to much higher energies with its 10-600 keV pointed bandpass. The X-Ray Spectrometer (XRS) is no longer operational, and will not be discussed further. Interested readers are invited to access the XRS instrument paper at `http://www.astro.isas.jaxa.jp/suzaku/doc/suzakumemo/suzakumemo-2006-38.pdf`.

All of the instruments on *Suzaku* operate simultaneously. Each of the co-aligned XRTs features an X-ray mirror with an angular resolution (expressed as Half-Power Diameter, or HPD) of $\sim 2'$ (Fig. 3.4). Figure 3.3 shows the total effective area of the XIS+XRT, which includes features due to the elemental composition of the XIS and XRT. K-shell absorption edges from oxygen (0.54 keV) and aluminum (1.56 keV) in the blocking filters are present, as well as a number of weak M-shell features between 2–3 keV arising from the gold in the XRT.

The four XISs (Fig. 7.3) are true imagers, with a large field of view ($\sim 18' \times 18'$), and moderate spectral resolution.

The HXD (Fig. 8.1) is a non-imaging instrument with an effective area of $\sim$260 cm^2, featuring a compound-eye configuration and an extremely low background. It dramatically extends the bandpass of the mission with its nominal sensitivity over the 10–600 keV band (Fig. 3.5). The HXD consists of two types of sensors: 2 mm thick silicon PIN diodes sensi-

S/C	Orbit apogee	568 km
	Orbital period	96 minutes
	Observing efficiency	$\sim 45\%$
XRT	Focal length	4.75 m
	Field of view	$17'$ at 1.5 keV
		$13'$ at 8 keV
	Plate scale	0.724 arcmin/mm
	Effective area	440 cm^2 at 1.5 keV
		250 cm^2 at 8 keV
	Angular resolution	$2'$ (HPD)
XIS	Field of view	$17.8' \times 17.8'$
	Bandpass	0.2–12 keV
	Pixel grid	1024×1024
	Pixel size	$24\,\mu m \times 24\,\mu m$
	Energy resolution	~ 130 eV at 6 keV
	Effective area	340 cm^2 (FI), 390 cm^2 (BI) at 1.5 keV
	(incl XRT-I)	150 cm^2 (FI), 100 cm^2 (BI) at 8 keV
	Time resolution	8 s (Normal mode), 7.8 ms (P-Sum mode)
HXD	Field of view	$4.5^\circ \times 4.5^\circ$ ($\gtrsim 100$ keV)
	Field of view	$34' \times 34'$ ($\lesssim 100$ keV)
	Bandpass	10–600 keV
	– PIN	10–70 keV
	– GSO	40–600 keV
	Energy resolution (PIN)	~ 4.0 keV (FWHM)
	Energy resolution (GSO)	$7.6/\sqrt{E_{\rm MeV}}$ % (FWHM)
	Effective area	~ 160 cm^2 at 20 keV, ~ 260 cm^2 at 100 keV
	Time resolution	61 μs
HXD-WAM	Field of view	2π (non-pointing)
	Bandpass	50 keV–5 MeV
	Effective area	800 cm^2 at 100 keV / 400 cm^2 at 1 MeV
	Time resolution	31.25 ms for GRB, 1 s for All-Sky-Monitor

Table 3.1: Overview of *Suzaku* capabilities.

.

tive over 10–70 keV, and GSO crystal scintillators placed behind the PIN diodes covering 40–600 keV. The HXD field of view is actively collimated to $4.5^\circ \times 4.5^\circ$ by the well-shaped BGO scintillators, which, in combination with the GSO scintillators, are arranged in the so-called phoswich configuration. At energies below $\sim$100 keV, an additional passive collimation further reduces the field of view to $34' \times 34'$. The energy resolution is $\sim$4.0 keV (FWHM) for the PIN diodes, and 7.6 / $\sqrt{E}$ % (FWHM) for the scintillators (where E is energy in MeV). The HXD time resolution for both sensors is 61 μs. While the HXD is intended mainly to explore the faintest hard X-ray sources, it can also tolerate very bright sources up to ~10 Crab. The HXD also performs as an all-sky monitor (the Wide-band All-sky Monitor (WAM), which can detect GRBs and other sources. Although observers will receive data from the WAM, it cannot be proposed for directly and has special rules regarding data rights; see Chapter 4.

Because the HXD bore-sight axis, with the highest effective area, is about 3.5 arcmin shifted from that of the XISs, the *Suzaku* operations team supported two aim points, XIS and HXD oriented, in the past. The XIS aim point provides a ~10% larger XIS effective area than the HXD aim point. Conversely for the HXD, the HXD aim point provides a ~ 10% larger HXD effective area than the XIS aim point. A 10% increase in effective area corresponds to a 10% and 20% increase in observing time for source and background dominated observations, respectively. In order to mitigate effects due to the increased attitude jitter of *Suzaku* since the end of 2009 the HXD aim point is not supported anymore in AO-7.

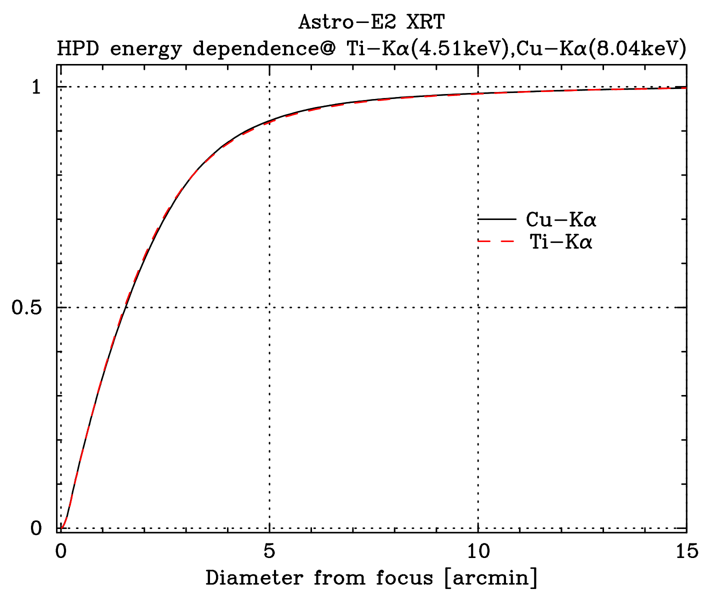

Figure 3.4: The Encircled Energy Function (EEF) showing the fractional energy within a given radius for one quadrant of the XRT-I telescopes on *Suzaku* at 4.5 and 8.0 keV.

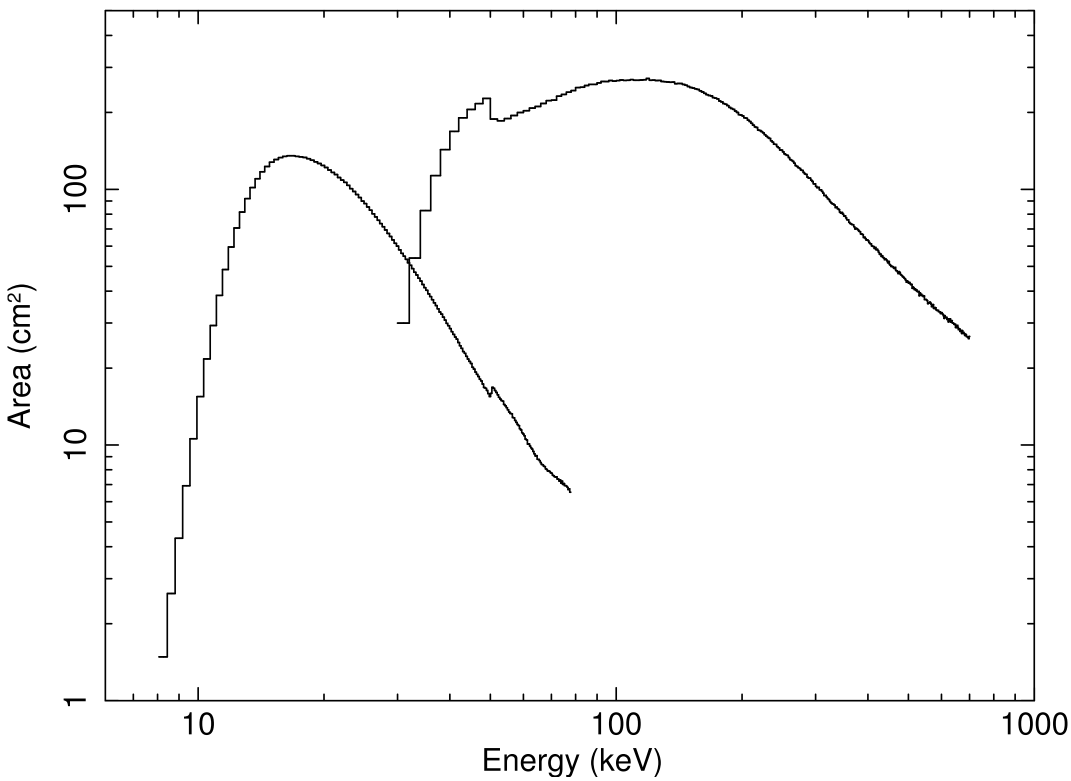

Figure 3.5: Total effective area of the HXD detectors, PIN and GSO, as a function of energy.

3.2 Operational Constraints

3.2.1 Telemetry Rates

Suzaku carries a 6 Gbit data recorder. Data will be down-linked to USC at a rate of 4 Mbps for a total of 2 Gbits per pass, up to 5 times a day. This allows a maximum of 10 Gbits of data to be obtained per day, but fewer passes may be available to *Suzaku* as it will share the use of USC ground station with other ISAS satellites[1]. Data can be recorded at 4 different rates: Super-High (524 kbps), High (262 kbps), Medium (131 kbps), and Low (33 kbps). The recording rate will be changed frequently throughout an observation, according to a sequence that will be determined by the operations team at ISAS. This is to optimize the selection of the data rates and the usage of the data recorder, taking into account the expected count rates supplied by the proposers. Thus an accurate estimation of the count rates is important for the optimization of the mission operation. **We emphasize that proposers cannot arbitrarily choose the data recording rate**.

[1]Unlike *ASCA*, NASA DSN stations will not be used, since a 4 Mbps down-link is not possible at DSN stations.

On-source data will usually be recorded at High (during contact orbits, during which the satellite passes over USC) or Medium (during remote orbits, without USC passes) data rate. The Low rate will primarily be used for times of Earth occultations and SAA passages, as the background rates in the XIS and HXD exceed their telemetry allocation limit at Low data rate. The telemetry limits for the XIS are presented in Chapter 7. The XIS data mode will be chosen for each data recording rate used to prevent telemetry saturation, based on the count rate supplied by the proposer.

3.2.2 Summary

Suzaku excels for observations such as:

- Studies of diffuse soft X-ray sources with low surface brightness: the low background, soft X-ray sensitivity, and near-Gaussian response of the XIS BI CCD makes such targets an excellent use of *Suzaku*.
- Observations requiring sensitivity both above and below 10 keV, especially measuring the Fe K complex simultaneously with the hard (>10 keV) continuum.
- Rapid variability studies on 10 ms time scales. The best time resolution available on the XIS is ~ 7.8 ms, while the HXD time resolution is $\sim 61\,\mu$s (see Table 3.1)

Suzaku is less appropriate for:

- Studies requiring primarily high spatial resolution. *Chandra*'s PSF is $\sim 100\times$ smaller than *Suzaku*'s, while the *XMM-Newton* PSF is $\sim 10\times$ smaller.
- Studies requiring primarily high spectral resolution. The gratings on *Chandra* and *XMM-Newton* have significantly higher resolution than the XIS.

3.3 Calibration

Table 3.2 summarizes the calibration items of all scientific instruments, the current status, and their expected and measured accuracy.

These values are the 90% limits, equivalent to 1.6σ. Note that the values listed are those required from the scientific purpose and ultimate goals which are possible to be realized on the basis of the instrument design.

Table 3.2: Error Budgets of Scientific Instrument Calibrations.

	Calibration Item	Oct 2008	Requirement	Goal
XRT−I/XIS	On-axis effective area [a]	∼2%	5%	5%
	Vignetting[a]	∼10%	5%	2%
	On-axis EEF [b]	∼3%	5%	1%
	Off-axis EEF [c]	∼3%	20%	2%
	Optical axis position in XIS	$\sim 0.5'$	$<0.2'$	$<0.2'$
	Energy scale[d]	max(0.2%, 5 eV)	0.1%	0.1%
	Energy resolution (FWHM) at 5.9 keV	5%[e]	1%	1%
	Contamination thickness[f]	$10^{18}\,\mathrm{cm}^{-2}$	N/A	N/A
	OBF integrity	unbroken	broken/unbroken	broken/unbroken
HXD	Absolute effective area	20%	20%	5%
	Relative effective area	10%	10%	5%
	Vignetting	5%	10%	5%
	Background modeling (PIN)[g]	3 ∼ 5%	10%	1%
	Background modeling (GSO)[g]	1.5 ∼ 2%	10%	3%
	Absolute timing[h]	300 μs	300 μs	100 μs
	Relative timing[h]	1.9×10^{-9}	10^{-8}	10^{-10}
	GRB absolute timing	∼2 ms	10 ms	1 ms

a: Valid in the 2-10 keV band. Calibration uncertainty may become larger outside this energy range, especially below 0.3 keV (BI chip) and above 10 keV. We calibrated the effective area using spectral parameters of the Crab emission as those given by Toor & Seward (1974, AJ, 79, 995).
b: For all integration radii from $1'$-$6'$. No error on attitude control is included.
c: As on-axis but for all XIS f.o.v. No calibration is currently scheduled.
d: For the normal mode data. Uncertainties of the energy scale increase when the Burst and/or Window options are applied.
e: When xisrmfgen is used. Note that an error of 5% in the energy resolution could produce an artificial line width of as large as ∼25 eV in sigma at the iron band. Energy resolution with the spaced-row charge injection is under investigation.
f: Uncertainty represented as the carbon-equivalent column density. Valid only at the center of the field of view.
g: Modeling accuracy depends on energy-band and exposure. See Chapter 8.5 for typical examples.
h: The Crab and PSR B1509-58 pulses are clearly detected in the quick look analysis of calibration data.

Chapter 4

Observation Policies

In AO-8, 100% of the observing time available is used for GO observations. The current schedule for the time allocation between Japanese and US PIs is given in Table 4.1. The AO will run for a year starting in April 2013. However, given the secular degradation of its power system, the possibility that the observations cannot continue throughout the 1-year AO period should be kept in mind.

In 2009, the new category of Key Project proposals was introduced. Key Projects were defined as comprehensive observing programs sampling a number of objects of a particular class, or surveying a large region of the sky, in order to take maximal advantage of the unique attributes of *Suzaku* to address important astrophysical problems. Given the above situation, no new Key Project proposals are being solicited in AO-8, while the completion of on-going Key Projects will be a high priority of the mission.

After seven years of operation, we know that the actual observing efficiency is about 38 ks per day and we assume 360 days of operations per year. From the total of 13680 ks, we subtract 3% of the available time as observatory time used for satellite maintenance and similar purposes, and 5% for ongoing calibration observations. Finally, 5% are earmarked as Director's Discretionary Time (DDT) for unproposed Target of Opportunity (TOO) proposals (including observations of gamma-ray bursts) and other important observations, granted at the mission director's discretion. Therefore $13680 \times 0.87 = 11902$ ks are nominally available to the community via the proposal selection process.

The project will over-subscribe this total by 40% including category C targets for which the observation is not guaranteed (see Section 4.4 below). If the actual sum of the observatory, calibration, and director's times is less than 12%, additional C targets will be observed.

In this AO, up to 2 Ms will be set aside for continuing Key Projects. 5,451 ks are assigned to Japanese observations and 3,963 ks go to US observations. The remaining 488 ks, plus any time remaining in the Key Project allocation, are set aside for joint Japan-

Phase	Months Post-Launch	SWG	Japan (ESA)	US	Japan/US	Key Project
AO-8	93-104	0	5451 (909)	3963	>488	<2000

Table 4.1: *Suzaku* time allocated to each group of observers. The ESA time is in parentheses as it is part of the Japanese allotment.

US investigations. When the respective national reviews have selected the same target, the two proposals will be merged if both teams indicated their willingness to collaborate on the RPS form, and the observation will be counted against the Japan-US time. If such mergers do not take up 488 ks, the remainder will be divided between separate Japanese and US investigations. Additionally, within the "Japanese" allocation, 909 ks are reserved for proposals submitted to ESA as joint Japan-ESA observations. Proposals from non-US, non-ESA countries will be accepted within the Japanese time up to the ESA portion.

The nationality of the PI's institution determines which agency should receive the proposal. That is, researchers at US institutions must submit their proposals to NASA and those at institutions in ESA member countries must submit theirs to ESA (regardless of their actual nationality). While the ISAS/JAXA proposal process is primarily aimed at researchers resident in Japan, proposals from researchers in other (non-US, non-ESA) countries will also be considered. A PI with dual affiliations generally must choose a single agency for all his/her AO-8 proposals, even if they are for independent projects. Only in rare cases, a single PI may be considered eligible to submit Suzaku proposals through multiple agencies. Co-Is from any country may be part of any proposal, though.

The category of "Long Program" for proposals with a total exposure time >300 ks, available in (only) the US from AO-3 to AO-6 is **not** offered in AO-8.

Regular US proposals may request no more than 1 Ms of observing time for practical reasons (regular ISAS/JAXA proposals may not exceed total exposure times of 400 ks). Note that for TOO proposals this 1 Ms limit applies to the actually requested observing time. It is therefore possible to request 400 ks per target for up to 2 triggers among 5 potential targets, for example.

4.1 Data Rights

The data rights policy for *Suzaku* is similar to previous missions. The normal exclusive period for GO data is one year, **except for proposals with a total accepted exposure time > 300 ks (including priority C targets), and DDT data** which are made public immediately.

Accepted targets will be classified into three categories. Priority A targets will be preferentially observed during the AO-8 period (April 2013 to March 2014). Priority B targets will be scheduled in this period as much as possible, but may be carried over to the next cycle. Priority C targets will be used as fillers when there are gaps in the schedule. For the total available time T, we currently plan to accept 0.6 T, 0.3 T, and 0.5 T as As, Bs, and Cs (for a total over-subscription by 40%).

During AO-8, category A and B targets will be considered complete if 90% (for A targets) or 70% (for B targets) of the proposed time is obtained on the source. In general, supplementary observations will be performed for A or B targets that do not meet the completion criteria, although it may not always be possible in case of time critical observations.

During the GO phase, data from calibration and TOOs requested outside the proposal process (see below) will not be considered proprietary.

4.2 Target of Opportunity Proposals

TOO proposals are allowed for *Suzaku* through the normal proposal process, although they must be highly ranked (see below) to be accepted. Proposals with TOOs should not be mixed with non-TOO targets. TOO proposals are allowed for short-lived events in known objects the timing of which is uncertain. These should only include unpredictable phenomena in a specific target (e.g., SS Cyg in outburst), not a generic target (e.g., the next Galactic supernova). The trigger criteria **must** be explicit and quantifiable, and stated in detail in the proposal text; a brief summary should appear in the "Remarks" section of the target form. In addition, TOO proposals **must provide an estimated probability of a successful trigger** during the AO period. It is **the PI's responsibility** to notify the *Suzaku* project when the criteria are met. **Generic TOOs without a specific target (such as "a nearby supernova") will not be accepted. In the same spirit, the number of targets in TOO proposals should not exceed 5.** Gamma-ray bursts or any genuinely unpredictable events may be observed outside the proposal process, as part of the 5% DDT. Data from such observations will not have a proprietary period.
To request such unproposed TOO observations, please send an e-mail to: `suzaku_managers` <at> `astro.isas.jaxa.jp` using the format specified in `http://www.astro.isas.jaxa.jp/suzaku/planning/gtoo/`.

4.3 Pointing Constraints

The Solar panels on the *Suzaku* satellite are fixed. This places a restriction on the pointing direction with respect to the satellite-Sun line: the Sun angle constraint during AO-8 is 70–110 degrees. This means that at any given time of the year, only a swath of the sky 40 degrees wide is accessible for astronomical observations, and thus most celestial sources are available for observations for about 40 days every 6 months. If a specific observing date or a coordinated observation with other missions is required, the proposer must first determine if the observation is possible. This can be done using the "Viewing" tool on the *Suzaku* proposal web-site (see Appendix B).

Long (>1 day) observations are the norm for *Suzaku*. A large number of short observations is an inefficient use of the satellite because of the unusable time during slews and attitude settling. The pointing is expected to be accurate to 0.3 arcmin and can be reconstructed to better than 0.2 arcmin, except during the initial settling period of up to 10 minutes. Moreover, there is a limit on the number of slews that can be uploaded to *Suzaku*. For these reasons, a minimum exposure time of 10 ks has been set for all proposed observations.

Contiguous observations, i.e., observations not disrupted by the observation of another target, are generally guaranteed up to exposures of not more than 100 ks. This limitation is due to moon light constraints for the star trackers' field of view, conflicts with other time critical observations, and other operational/planning difficulties. While the operation team does accept requests for uninterrupted observations longer than the 100 ks, these are conducted on a best-effort basis.

Even during shorter pointed observations, there will typically be interruptions due to the location of *Suzaku* in a low Earth orbit: Normally, a target will be occulted by the Earth for ∼30 minutes every satellite orbit. In addition, *Suzaku* will pass through the South Atlantic Anomaly (SAA) during parts of 5 or 6 orbits every day. Due to the harsh radiation environment of the SAA, scientific observation is not possible during SAA passages. There are other variations in the particle background, depending primarily on the Cut-Off Rigidity (COR)[1]. The optimal criteria to reduce times of high background while maximizing the science return are still being determined from SWG observations, please check the *Suzaku* web-sites (see Appendix B) for the most up-to-date suggestions.

There are also orbital constraints on the orientation of the projection of the XIS CCDs on the sky. Since the *Suzaku* XIS arrays are square, with calibration sources in different corners, selecting a specific roll angle is rarely significant. However, if a specific roll angle is scientifically advantageous, the proposer must first determine if it is allowed. This can be done using the MAKI tool described in Section 5.7. Then the required roll range can be entered on the RPS proposal form. For objects close to the ecliptic poles it is possible to arrange for any XIS orientation by scheduling observations at a specific time, but for those located close to the ecliptic, the XIS will project on the sky in a nearly fixed orientation. **Note that any roll constraint will make a proposal time critical.**

It is possible to specify the time of observations (time critical, or TC, observations) in order to observe during specific phases or for simultaneous observations. Monitoring observations (repeated observations with a specified interval) or roll-angle constrained ob-

[1] *Suzaku* is protected from solar and cosmic-ray particles by the geomagnetic field. The COR is an indicator of the minimum momentum required for a particle to reach a specific location, given the average geomagnetic field configuration.

servations are also considered time critical, and must be so flagged on the proposal form. The total accepted time of the TC and TOO proposals is less than 15% of the total observation, and proposers should justify their requirements carefully.

Overall the proposers are strongly urged to provide accurate information. All information that is indispensable for operation planning should be provided on the electronic forms. The PIs are advised to utilize the "Remarks" area if they have detailed requests which cannot be expressed with the check boxes/pull-down menus.

4.4 Events After Submission

After the *Suzaku* proposal deadline, there will be three independent proposal reviews for the US, Japan, and ESA proposals. Each review will create a target list from the proposed observations, ranking the accepted targets as category A, B, or C. Only category A and B targets are guaranteed to be observed. As stated above, TOOs and time critical observations are only accepted within 15% of the total time – however, the project will review this limit given the narrower range of sun angles allowed and other power-related considerations at the time of the international merging meeting in February 2013. Category C targets will be observed as time permits, and will not be carried over into the next AO if not observed in this AO. An international merging committee will collate the three target lists and produce a single, unified list. Overlaps between US and Japanese targets will be resolved, either by merging the investigations (if both parties are willing) or by choosing one. In the latter process, the priority given by the national reviews, as well as the lengths of the accepted observations, will be considered. The final target list will be $\sim$ 40% oversubscribed. Category A and Key Project targets will have 60% of the available time, category B 30%, and category C 50%.

Even though observations are scheduled to acquire roughly the approved exposure time and although this is usually achieved with *Suzaku*, occasional losses of usable observation time are inevitable. As mentioned above, Category A observations will be deemed complete when they have received at least 90% of the approved time. Note that this will be judged based on the good time intervals of the cleaned XIS event files after the standard screening. Dead times (including those due to the use of the burst option) are not taken into account. Also, the standard screening for the HXD is more strict, so the effective exposure for the HXD is often smaller than that of the XIS by 20% or more. Additional observations will be scheduled automatically for those non-time-critical targets the observations of which are considered incomplete by the project scientist at ISAS. In the case of time-critical observations which are incomplete or unusable, it will be the PI's responsibility to determine the best course of action.

Each PI will be assigned a contact scientist, either at ISAS or the NASA *Suzaku* GOF, who will work with the PI to assure the maximum science return. This will include double-checking coordinates, count rates and finalizing configurations (nominal pointing, XIS modes, . . .). It is important to note that once an observation has been scheduled, any delay in responding to questions from the contact scientist may result in targets being removed from the schedule. We do not have a mechanism to approve coordinated observations with *Suzaku* and another observatory through a single proposal except for the joint *Fermi-Suzaku* and *Chandra-Suzaku* programs noted earlier. It is the PI's responsibility to secure observing time with other observatories, when simultaneous observations are desirable. **Please note that the *Suzaku* component of such a proposal may be approved contingent on the success of other proposals.** Special scheduling requests and TOOs will be accommodated on a best effort basis. For simultaneous observations, the mission scheduler at ISAS, in consultation with the contact scientist, will contact the PI in advance for detailed scheduling information, and will often work directly with schedulers of other missions. During the AO-1–AO-7 observing periods, the *Suzaku* scheduling team made every effort to accommodate requests of coordinated/simultaneous observations with other facilities and we expect that it will continue to do so during AO-8.

Once the observation has been completed, the data will be promptly run through the processing pipeline and put into both the US and Japanese archives, initially in encrypted form, unless the proposal has a total accepted exposure time > 300 ks as noted above. The PI will be sent the decryption key, if applicable, along with instructions on how to download and decrypt the data. Another exception to the one year exclusive period for GO data concerns the HXD Wide-band All-sky Monitor (WAM) data (see Chapter 8). The WAM is primarily used for anticoincidence shielding in the HXD, but it can also be used as an all-sky monitor, detecting solar flares, gamma-ray bursts, and other bright X-ray sources (e.g., Cyg X-1). All data from the WAM will be monitored by the HXD team, which will alert the GRB community to any detected bursts. In addition, the HXD team will make analysis results from WAM, such as light curves and fluences, available to the public as soon as possible. These may be used to put limits on GRBs or other events triggered by other satellites or observatories. However, the PI will receive the complete WAM data from their observation and will share data rights with the *Suzaku* team for the normal 1 year proprietary period. This unusual arrangement is due to the time-critical and non-source-specific nature of the WAM data.

With the exception of the code that converts raw binary telemetry into FITS format files, all *Suzaku* software is written as FTOOLS and distributed through the *Suzaku* team at ISAS/JAXA and the NASA/GSFC HEASARC. This includes the tools used in the processing. All calibration files are distributed through the HEASARC `caldb` (calibration database) system. This enables users to apply any calibration updates themselves. The *Suzaku* team at ISAS and the NASA *Suzaku* GOF provide additional FTOOLS that may be necessary or desirable for analyzing *Suzaku* data. The use of other software packages will only be supported at a lower priority level.

Chapter 5

Writing A Successful *Suzaku* Proposal

Each *Suzaku* proposal must include at a minimum the source coordinates, exposure time, instrument configuration and expected count rates, and any observing constraints within the four page limit. The review panels will base their decision primarily upon the justification of the proposed science to be done with the data. This chapter describes how to prepare a strong proposal, including the various software tools available to assist the proposer.

5.1 First Checks

5.1.1 `Viewing`

One of the first tasks in preparing a proposal is determining when and for how long a target can be observed as there is very little use to simulate a source that cannot be observed. This can be easily done with `Viewing`, a simple web-based interactive tool (see Appendix B) that can determine visibility for many different satellites. To use `Viewing`, simply enter the target name or coordinates, and select the satellite. `Viewing` will return all the available dates when that target is observable.

5.1.2 Previous Observations

Another initial check to be performed before starting sophisticated simulations is to ensure that the target has not yet been extensively observed by *Suzaku*, e.g., using `Browse`. Users should also check the observations log located at
`http://suzaku.gsfc.nasa.gov/docs/suzaku/aehp_time_miss.html` as some of the tar-

gets (category C) may have been accepted but not observed.

5.2 Proposal Ingredients

While it is conceivable that one would wish to study a previously unknown X-ray source with *Suzaku*, a more likely scenario would involve a spectroscopic study of an object with known X-ray flux. A viable proposal should state the scientific objective of the observation and show that *Suzaku* can achieve this objective. Observations that require one or more of *Suzaku*'s unique capabilities would be especially strong candidates.

Every *Suzaku* proposal must have an estimate of the expected source count rates from the proposed target for all detectors. This rate is used both by the reviewers to evaluate the viability of the proposal and the operations team to evaluate any safety concerns. The simplest tool to use in estimating the expected XIS or HXD count rate is `PIMMS`. This tool is freely available as a stand-alone tool or on the web as `WebPIMMS` (see Appendix B). The next level of detail is provided via simulations using `XSPEC`, and such simulations should provide significant insight into the expected spectrum obtained from a proposed observation. A brief guide to `XSPEC` simulations is given in section 5.4. In many cases, this should be sufficient for a point source. There are also tools available to simulate imaging data, which may be useful for an extended source or a particularly bright source. In particular, the most powerful tool is `xissim`, which can use a FITS format image with an assumed spectral shape of the source to estimate the distribution of events in all elements of the XIS detectors.

5.3 `PIMMS` & `WebPIMMS`

`PIMMS` is an interactive, menu-driven program, which has an extensive HELP facility. It is also available as the web-based tool `WebPIMMS`. In either case, users specify the flux and spectral model with its parameters, and `PIMMS/WebPIMMS` returns the predicted count rate. `PIMMS/WebPIMMS` can be used for a variety of other instruments, so if, for instance, the count rate and spectrum of a given source observed with the *ROSAT* PSPC is known, `PIMMS/WebPIMMS` can estimate the expected count rates for *Suzaku*'s instruments. The limitations of the input source must be considered carefully. For example, *ROSAT* had no significant response to X-rays above $\sim 2.4\,\mathrm{keV}$, and so is not useful when estimating the HXD GSO count rate.

5.4 XSPEC Simulations

Perhaps the easiest tool for simulating X-ray spectra is the XSPEC program (a part of the XANADU software package), which is designed to run on a variety of computer platforms and operating systems and is freely distributed on the NASA GSFC HEASARC web-site (see Appendix B). The simulation of an XIS observation requires the current instrument redistribution matrix (the so-called RMF file) and the energy-dependent effective area of the instrument (the so-called ARF file), while the simulation of an HXD observation requires the current instrument response (the so-called RSP file). These files are available on the Web or via anonymous FTP (see Appendix B).

The procedure for simulations is relatively simple: if the XSPEC program is installed, one should start XSPEC, making sure that the proper RMF, ARF, and RSP files are accessible. Within XSPEC, one should specify the spectral model, such as hot thermal plasma or the like (via the *model* command). Specifying the model will drive XSPEC to query for the model parameters (such as the temperature and abundances for an APEC collisional plasma model), as well as its normalization. The key command to create a simulated spectrum is the *fakeit* command, which will query for the RMF and ARF files, when simulating XIS, or for an RSP file, in the HXD case. The *fakeit* command will also request the data filename and the length of the observation to be simulated. One can then use the resulting spectrum within XSPEC to determine the sensitivity of the simulated data file to changes in the model parameters. Users should adjust the normalization of their input models to reflect the actual count rate or flux (absorbed or unabsorbed) of their source.

5.4.1 WebSPEC Simulations

Some of the features of XSPEC are also available as a web-based tool on the HEASARC web-site (see Appendix B). WebSPEC calls XSPEC behind the scenes, so the description above applies here as well.

After selecting the instrument, WebSPEC allows the user to choose the spectral model, such as an absorbed collisional plasma or a power-law spectrum with an absorption component. The next page will then query for the model parameters (such as the temperature and abundances for an APEC collisional plasma model), as well as its normalization. In addition, it queries for the simulation parameters, i.e., the exposure, upper and lower energies, and the number of bins to use in the spectral plot. WebSPEC will then create a simulated spectrum after clicking the "Show me the Spectrum" button, using the *fakeit* command. This folds the specified model through the instrument response and effective area, calculating the observed count rate and fluxes as well. WebSPEC will then allow one to download the postscript file of the spectrum, change the model parameters, or re-plot the data.

5.5 Examples

In order to show how to estimate the proper exposure, we include some simple examples of XIS and HXD observations that illustrate the process.

5.5.1 Faint Oxygen Emission from the Local Hot Bubble

The Local Hot Bubble is the proposed origin for at least some of the 1/4 keV emission seen in the *ROSAT* All-Sky Survey at all latitudes. Although *Suzaku* has some sensitivity at 1/4 keV, a more profitable approach to finding this emission is to detect the O VII emission that should accompany it. In this case we need to calculate the expected count rate from the O VII and compare it to the expected background.

We first need the expected flux, based on published papers or the PI's model. In this case, we expect the surface brightness to be 0.34 ph/cm^2/s/sr, based on a number of papers. Since the XIS field of view is $18' \times 18'$, this value corresponds to a total surface brightness in one XIS of 9.3×10^{-6} ph/cm^2/s. The next question is the effective area of the XIS instruments at the line energy. O VII is in fact a complex of lines, centered around 0.57 keV. Examining the effective area plots for the XIS in Chapter 3, we see that the effective area at 0.57 keV in the BI CCD is ~ 140 cm^2; for the FI CCDs it is ~ 90 cm^2. The curves shown on Fig. 3.3 do not include the contamination effect. The computation below is only given as an example. Please note that the more current effective area curves for the FI and BI CCDs can also be found by loading their responses into `XSPEC` and using the `plot efficiency` command. *Warning:* The XIS RMF response matrices are **not** normalized, and thus must be combined with the ARF files to determine the total effective area. With the expected flux and the effective area, we can now determine the expected count rate in the BI and FI CCDs to be 1.3 and 0.87 counts/ks. This is obviously a extremely low count rate and so the expected background is very important. The resolution of the XIS is quite good, as shown in Chapter 7, at 0.57 keV a bin of width 60 eV will contain most of the emission. The XIS background rate (see section 7.3.4 at this energy is only 0.05 counts/s/keV in both the FI and BI detectors, so we can expect a background of 3 counts/ks. In both the FI and BI detectors the line will be below the background, but this does not intrinsically hinder detection. As will be seen below, in the HXD this is the norm rather than the exception. One aid for this observation is that the O VII line is relatively isolated in this energy range, with the exception of the nearby O VIII line. Assume we wish to detect the O VII feature with 3σ significance. The total count rate in the XIS-S1 (the BI CCD) in our energy band will be 4.3 counts/ks, with 3 counts/ks of background. In an N ks observation, we will measure the signal to be $1.3 \times N \pm \sqrt{4.3 \times N}$. To achieve a 3σ result, then, we need $1.3 \times N/\sqrt{4.3 \times N} > 3$, or $N > 23$ ks.

5.5.2 Hard Tails of XRBs

Another common observation will be to search for faint hard X-ray tails from sources such as X-ray binaries. We describe here how to simulate such an observation, including the all-important HXD background systematics, which will dominate all such observations.

The first step is to download the latest versions of the background template files and the response files from the web-site listed in Appendix B. The HXD web-site will also describe the current best value for the systematic error in background estimation. For this AO, proposers should carefully read Chapter 8 and evaluate the systematic errors for the PIN and the GSO backgrounds in the energy band of interest, and at the exposure level chosen. For example, for a 100 ks exposure, the value for the PIN in the 15–40 keV band and the GSO in the 50–100 keV band can be estimated to be ∼3% and ∼1.5%, respectively. Since the energy bands are important in this case, the associated errors should first be estimated and then used in the procedure described below. In addition, the proposer should also check if contaminating sources exist in the FOV of the HXD, using existing hard X-ray source catalogs from satellites such as *RXTE*-ASM, *INTEGRAL*, and *Swift*, before beginning this process.

We set up `XSPEC` for simulating by reading the background template files as both data and background along with the response files:

```
XSPEC12>data ae_hxd_pinbkg_20101012.pha ae_hxd_gsobkg_20101012.pha

2 spectra  in use

Spectral Data File: ae_hxd_pinbkg_20101012.pha  Spectrum 1
Net count rate (cts/s) for Spectrum:1  4.735e-01 +/- 3.973e-04
 Assigned to Data Group 1 and Plot Group 1
  Noticed Channels:  1-256
  Telescope: SUZAKU Instrument: HXD  Channel Type: PI_PIN
  Exposure Time: 3e+06 sec
 Using fit statistic: chi
 No response loaded.

Spectral Data File: ae_hxd_gsobkg_20101012.pha  Spectrum 2
Net count rate (cts/s) for Spectrum:2  4.397e+01 +/- 3.829e-03
 Assigned to Data Group 1 and Plot Group 2
  Noticed Channels:  1-512
  Telescope: SUZAKU Instrument: HXD  Channel Type: PI_SLOW
  Exposure Time: 3e+06 sec
 Using fit statistic: chi
 No response loaded.
```

```
***Warning!  One or more spectra are missing responses,
               and are not suitable for fit.
XSPEC12>back ae_hxd_pinbkg_20101012.pha ae_hxd_gsobkg_20101012.pha
Net count rate (cts/s) for Spectrum:1  0.000e+00 +/- 5.619e-04 (0.0 % total)
Net count rate (cts/s) for Spectrum:2  0.000e+00 +/- 5.414e-03 (0.0 % total)
***Warning!  One or more spectra are missing responses,
               and are not suitable for fit.
XSPEC12>resp ae_hxd_pinxinome9_20100731.rsp ae_hxd_gsoxinom_20100524.rsp
Response successfully loaded.
Response successfully loaded.
```

We first create background spectra with the correct statistics, by simulating an observation with no source flux using the `fakeit` command. In the case of the PIN the simulated background exposure is a factor 10 higher than the exposure of the source observation to be simulated (here 10^6 s), following the prescription for PIN data analysis. In the case of the GSO the simulated background exposure is equal to the exposure of the source observation (here 10^5 s).

```
XSPEC12>model powerlaw

Input parameter value, delta, min, bot, top, and max values for ...
              1       0.01(      0.01)         -3         -2          9         10
1:powerlaw:PhoIndex>1
              1       0.01(      0.01)          0          0      1e+24      1e+24
2:powerlaw:norm>0

========================================================================
Model powerlaw<1> Source No.: 1   Active/On
Model Model Component  Parameter  Unit     Value
 par  comp
   1    1   powerlaw   PhoIndex            1.00000      +/-  0.0
   2    1   powerlaw   norm                0.0          +/-  0.0
________________________________________________________________________


 Chi-Squared =            0.0 using 768 PHA bins.
 Reduced chi-squared =            0.0 for    766 degrees of freedom
 Null hypothesis probability =   1.000000e+00

***Warning: Chi-square may not be valid due to bins with zero variance
            in spectrum number(s): 1 2
```

```
 Current data and model not fit yet.
XSPEC12>fakeit
 Use counting statistics in creating fake data? (y):
 Input optional fake file prefix:
 Fake data file name (ae_hxd_pinbkg_20101012.fak): pin_10mCrab_1Ms.bkg
 Exposure time, correction norm, bkg exposure time (3.00000e+06, 1.00000, 3.00000e+06):
                                                                          1000000
 Fake data file name (ae_hxd_gsobkg_20101012.fak): gso_10mCrab_100ks.bkg
 Exposure time, correction norm, bkg exposure time (3.00000e+06, 1.00000, 3.00000e+06):
                                                                          100000

No ARF will be applied to fake spectrum #1 source #1

No ARF will be applied to fake spectrum #2 source #1

2 spectra  in use


 Chi-Squared =         637.77 using 768 PHA bins.
 Reduced chi-squared =        0.83260 for    766 degrees of freedom
 Null hypothesis probability =   9.997317e-01

***Warning: Chi-square may not be valid due to bins with zero variance
            in spectrum number(s): 1 2

 Current data and model not fit yet.
```

Now we assume a spectrum for our source; here, we use a Crab-like spectrum (Toor & Seward 1974 AJ, 79, 995) with a photon index of 2.1, a hydrogen column density N_H of $3{\times}10^{21}\,cm^{-2}$, and 10m Crab flux. This can be set up in XSPEC via the following commands (note that while the response files are still present from the previous step, the simulated background files from the previous step should be loaded as background files, and the data files do not matter):

```
XSPEC12>back pin_10mCrab_1Ms.bkg  gso_10mCrab_100ks.bkg
Net count rate (cts/s) for Spectrum:1  2.101e-17 +/- 9.723e-04 (0.0 % total)
Net count rate (cts/s) for Spectrum:2  -3.640e-15 +/- 2.965e-02 (-0.0 % total)

 Chi-Squared =          3e-26 using 768 PHA bins.
 Reduced chi-squared =          4e-29 for    766 degrees of freedom
 Null hypothesis probability =   1.000000e+00
```

```
***Warning: Chi-square may not be valid due to bins with zero variance
            in spectrum number(s): 1 2

 Current data and model not fit yet.
XSPEC12>model phabs*powerlaw

Input parameter value, delta, min, bot, top, and max values for ...
              1      0.001(      0.01)          0          0     100000      1e+06
1:phabs:nH>0.3
              1       0.01(      0.01)         -3         -2          9         10
2:powerlaw:PhoIndex>2.1
              1       0.01(      0.01)          0          0      1e+24      1e+24
3:powerlaw:norm>0.097

========================================================================
Model phabs<1>*powerlaw<2> Source No.: 1   Active/On
Model Model Component  Parameter  Unit     Value
 par  comp
   1    1   phabs      nH         10^22    0.300000     +/-  0.0
   2    2   powerlaw   PhoIndex            2.10000      +/-  0.0
   3    2   powerlaw   norm                9.70000E-02  +/-  0.0
________________________________________________________________________


 Chi-Squared =       184046.2 using 768 PHA bins.
 Reduced chi-squared =       240.5832 for    765 degrees of freedom
 Null hypothesis probability =   0.000000e+00

***Warning: Chi-square may not be valid due to bins with zero variance
            in spectrum number(s): 1 2

 Current data and model not fit yet.
```

Now we can create fake PIN and GSO data for the planned observation using the `fakeit` command. The result will be simulated spectral files which include the instrumental background, effective area, and resolution:

```
XSPEC12>fakeit
 Use counting statistics in creating fake data? (y):
 Input optional fake file prefix:
 Fake data file name (pin_10mCrab_1Ms.fak): pin_10mCrab_100ks.fak
```

```
 Exposure time, correction norm, bkg exposure time (1.00000e+06, 1.00000, 1.00000e+06):
                                                                                 100000
 Fake data file name (gso_10mCrab_100ks.fak): gso_10mCrab_100ks.fak
 Exposure time, correction norm, bkg exposure time (100000., 1.00000, 100000.): 100000

No ARF will be applied to fake spectrum #1 source #1

No ARF will be applied to fake spectrum #2 source #1

2 spectra  in use


 Chi-Squared =          660.11 using 768 PHA bins.
 Reduced chi-squared =        0.86289 for    765 degrees of freedom
 Null hypothesis probability =   9.974261e-01

***Warning: Chi-square may not be valid due to bins with zero variance
            in spectrum number(s): 1 2

 Current data and model not fit yet.
```

At this point we have created simulated spectral files for an observation of a 10 mCrab XRB, `pin_10mCrab_100ks.fak` and `gso_10mCrab_100ks.fak`. In order to achieve the statistics of an actual observations, these files have to be rebinned to the spectral binning of the regularly created GSO background files. A grouping file which can be used with the `FTOOL grppha` is available from
`http://heasarc.gsfc.nasa.gov/docs/suzaku/analysis/gsobgd64bins.dat`:

```
grppha gso_10mCrab_100ks.fak gso_10mCrab_100ks_bin.fak

  -------------------------
  MANDATORY KEYWORDS/VALUES
  -------------------------
  --------------------------------------------------------------------
  --------------------------------------------------------------------
  EXTNAME   - SPECTRUM        Name of this BINTABLE
  TELESCOP  - SUZAKU          Mission/Satellite name
  INSTRUME  - HXD             Instrument/Detector
  FILTER    -                 Instrument filter in use
  EXPOSURE  - 1.00000E+05     Integration time (in secs) of PHA data
  AREASCAL  - 1.0000          Area scaling factor
  BACKSCAL  - 1.0000          Background scaling factor
```

```
  BACKFILE  - gso_10mCrab_100ks_bkg.fak
  CORRSCAL  - -1.0000         Correlation scaling factor
  CORRFILE  - NONE            Associated correlation file
  RESPFILE  - ae_hxd_gsoxinom_20100524.rsp
  ANCRFILE  - NONE            Associated ancillary response file
  POISSERR  - TRUE            Whether Poissonian errors apply
  CHANTYPE  - PI_SLOW         Whether channels have been corrected
  TLMIN1    - 0               First legal Detector channel
  DETCHANS  - 512             No. of legal detector channels
  NCHAN     - 512             No. of detector channels in dataset
  PHAVERSN  - 1.1.0           OGIP FITS version number
  STAT_ERR  - FALSE           Statistical Error
  SYS_ERR   - FALSE           Fractional Systematic Error
  QUALITY   - TRUE            Quality Flag
  GROUPING  - TRUE            Grouping Flag
  ---------------------------------------------------------------------
  ---------------------------------------------------------------------
GRPPHA[] group gsobgd64bins.dat
GRPPHA[] exit
 ... written the PHA data Extension
 ...... exiting, changes written to file : gso_10mCrab_100ks_bin.fak
 ** grppha 3.0.1 completed successfully
```

The same grouping has to be applied to the GSO background spectrum:

```
grppha gso_10mCrab_100ks.bkg gso_10mCrab_100ks_bin.bkg

  -------------------------
  MANDATORY KEYWORDS/VALUES
  -------------------------
  ---------------------------------------------------------------------
  ---------------------------------------------------------------------
  EXTNAME   - SPECTRUM        Name of this BINTABLE
  TELESCOP  - SUZAKU          Mission/Satellite name
  INSTRUME  - HXD             Instrument/Detector
  FILTER    -                 Instrument filter in use
  EXPOSURE  - 1.00000E+05     Integration time (in secs) of PHA data
  AREASCAL  - 1.0000          Area scaling factor
  BACKSCAL  - 1.0000          Background scaling factor
  BACKFILE  - gso_10mCrab_100ks_bkg.bkg
  CORRSCAL  - -1.0000         Correlation scaling factor
  CORRFILE  - NONE            Associated correlation file
```

```
  RESPFILE  - ae_hxd_gsoxinom_20100524.rsp
  ANCRFILE  - NONE            Associated ancillary response file
  POISSERR  - TRUE            Whether Poissonian errors apply
  CHANTYPE  - PI_SLOW         Whether channels have been corrected
  TLMIN1    - 0               First legal Detector channel
  DETCHANS  - 512             No. of legal detector channels
  NCHAN     - 512             No. of detector channels in dataset
  PHAVERSN  - 1.1.0           OGIP FITS version number
  STAT_ERR  - FALSE           Statistical Error
  SYS_ERR   - FALSE           Fractional Systematic Error
  QUALITY   - TRUE            Quality Flag
  GROUPING  - TRUE            Grouping Flag
  --------------------------------------------------------------------
  --------------------------------------------------------------------
GRPPHA[group gsobgd64bins.dat] group gsobgd64bins.dat
GRPPHA[exit] exit
 ... written the PHA data Extension
 ...... exiting, changes written to file : gso_10mCrab_100ks_bin.bkg
 ** grppha 3.0.1 completed successfully
```

In the next step we fit these datasets with the Crab-like model defined above. We will use three different background assumptions – low, medium, and high – which vary by as much as 3% and 1.5% for the PIN and the GSO, respectively. This takes into account the fact that the "true" background will likely vary within these limits. We load the simulated source files (rebinned for the GSO). The simulated background files from the first `fakeit` step (rebinned for the GSO) – `pin_10mCrab_1Ms.bkg` and `gso_10mCrab_100ks_bin.bkg` –, are loaded as background files as well as as correction files ("corfiles"), the latter allowing for an easy way to vary the total background within `XSPEC`.

```
XSPEC12>data pin_10mCrab_100ks.fak gso_10mCrab_100ks_bin.fak

Spectrum #: 1 replaced

Spectrum #: 2 replaced

2 spectra  in use

Spectral Data File: pin_10mCrab_100ks.fak  Spectrum 1
Net count rate (cts/s) for Spectrum:1  3.803e-01 +/- 3.000e-03 (44.6 % total)
 Assigned to Data Group 1 and Plot Group 1
  Noticed Channels:  1-256
  Telescope: SUZAKU Instrument: HXD  Channel Type: PI_PIN
```

```
  Exposure Time: 1e+05 sec
 Using fit statistic: chi
 Using Background File                pin_10mCrab_100ks_bkg.fak
  Background Exposure Time: 1e+06 sec
 Using Response (RMF) File            ae_hxd_pinxinome9_20100731.rsp for Source 1

Spectral Data File: gso_10mCrab_100ks_bin.fak  Spectrum 2
Net count rate (cts/s) for Spectrum:2  3.287e-01 +/- 2.970e-02 (0.7 % total)
 Assigned to Data Group 1 and Plot Group 2
  Noticed Channels:  1-64
  Telescope: SUZAKU Instrument: HXD  Channel Type: PI_SLOW
  Exposure Time: 1e+05 sec
 Using fit statistic: chi
 Using Background File                gso_10mCrab_100ks_bkg.fak
  Background Exposure Time: 1e+05 sec
 Using Response (RMF) File            ae_hxd_gsoxinom_20100524.rsp for Source 1


 Chi-Squared =         318.41 using 320 PHA bins.
 Reduced chi-squared =        1.0044 for    317 degrees of freedom
 Null hypothesis probability =   4.672303e-01

***Warning: Chi-square may not be valid due to bins with zero variance
            in spectrum number(s): 1 2

 Current data and model not fit yet.
XSPEC12>back pin_10mCrab_1Ms.bkg gso_10mCrab_100ks_bin.bkg
Net count rate (cts/s) for Spectrum:1  3.802e-01 +/- 3.000e-03 (44.6 % total)
Net count rate (cts/s) for Spectrum:2  3.261e-01 +/- 2.970e-02 (0.7 % total)

 Chi-Squared =         305.87 using 320 PHA bins.
 Reduced chi-squared =       0.96490 for    317 degrees of freedom
 Null hypothesis probability =   6.629651e-01

***Warning: Chi-square may not be valid due to bins with zero variance
            in spectrum number(s): 1 2

 Current data and model not fit yet.
XSPEC12>corfile pin_10mCrab_1Ms.bkg gso_10mCrab_100ks_bin.bkg
Net count rate (cts/s) for Spectrum:1  8.529e-01 +/- 3.000e-03 (64.3 % total)
 After correction of -4.727e-01 (using cornorm -1.000)
Net correction flux: 0.472657
```

```
Net count rate (cts/s) for Spectrum:2  4.427e+01 +/- 2.970e-02 (50.2 % total)
 After correction of -4.395e+01 (using cornorm -1.000)
Net correction flux: 43.9467


 Chi-Squared =   2.212409e+06 using 320 PHA bins.
 Reduced chi-squared =       6979.207 for    317 degrees of freedom
 Null hypothesis probability =   0.000000e+00

***Warning: Chi-square may not be valid due to bins with zero variance
            in spectrum number(s): 1 2

 Current data and model not fit yet.
XSPEC12>model phabs*powerlaw

Input parameter value, delta, min, bot, top, and max values for ...
              1      0.001(      0.01)          0          0     100000      1e+06
1:phabs:nH>0.3
              1       0.01(      0.01)         -3         -2          9         10
2:powerlaw:PhoIndex>2.1
              1       0.01(      0.01)          0          0      1e+24      1e+24
3:powerlaw:norm>0.097

========================================================================
Model phabs<1>*powerlaw<2> Source No.: 1   Active/On
Model Model Component  Parameter  Unit     Value
 par  comp
   1    1   phabs      nH         10^22    0.300000     +/-  0.0
   2    2   powerlaw   PhoIndex            2.10000      +/-  0.0
   3    2   powerlaw   norm                9.70000E-02  +/-  0.0
________________________________________________________________________


 Chi-Squared =   2.212409e+06 using 320 PHA bins.
 Reduced chi-squared =       6979.207 for    317 degrees of freedom
 Null hypothesis probability =   0.000000e+00

***Warning: Chi-square may not be valid due to bins with zero variance
            in spectrum number(s): 1 2

 Current data and model not fit yet.
```

We now experiment with different background levels, set by the value of "cornorm". A value of 0 gives the "normal" background, for example, 0.03 increases it by 3%, and -0.015 decreases it by 1.5%.

```
XSPEC12>cornorm 1-2 0.0
 Spectrum 1 correction norm set to 0
 Spectrum 2 correction norm set to 0

 Chi-Squared =         305.87 using 320 PHA bins.
 Reduced chi-squared =        0.96490 for    317 degrees of freedom
 Null hypothesis probability =   6.629651e-01

***Warning: Chi-square may not be valid due to bins with zero variance
            in spectrum number(s): 1 2

 Current data and model not fit yet.
XSPEC12>ignore 1:**-15. 70.-** 2:**-50. 600.-**
    40 channels (1-40) ignored in spectrum #     1
    70 channels (187-256) ignored in spectrum #     1
     1 channels (1) ignored in spectrum #     2
    12 channels (53-64) ignored in spectrum #     2

 Chi-Squared =         152.83 using 197 PHA bins.
 Reduced chi-squared =        0.78780 for    194 degrees of freedom
 Null hypothesis probability =   9.869519e-01
 Current data and model not fit yet.

XSPEC12>fit
                    Parameters
Chi-Squared  Lvl          1:nH    2:PhoIndex        3:norm
152.172       -3      0.986583       2.11789      0.101826
152.107       -4       5.56204       2.13807      0.109058
152.035       -5       6.34881       2.14176      0.110693
152.035       -6       6.39060       2.14198      0.110787
========================================
 Variances and Principal Axes
                 1        2        3
 8.9577E-07| -0.0002  -0.3165   0.9486
 3.3044E+02| -1.0000  -0.0035  -0.0014
 1.3350E-03| -0.0037   0.9486   0.3165
----------------------------------------
```

```
====================================
  Covariance Matrix
        1           2           3
   3.304e+02   1.145e+00   4.517e-01
   1.145e+00   5.168e-03   1.966e-03
   4.517e-01   1.966e-03   7.519e-04
------------------------------------

========================================================================
Model phabs<1>*powerlaw<2> Source No.: 1   Active/On
Model Model Component  Parameter  Unit     Value
 par  comp
   1    1   phabs      nH         10^22    6.39060      +/-  18.1780
   2    2   powerlaw   PhoIndex            2.14198      +/-  7.18907E-02
   3    2   powerlaw   norm                0.110787     +/-  2.74216E-02
________________________________________________________________________


 Chi-Squared =          152.04 using 197 PHA bins.
 Reduced chi-squared =        0.78369 for    194 degrees of freedom
 Null hypothesis probability =   9.884693e-01
XSPEC12>cpd /xs
XSPEC12>setplot energy
XSPEC12>plot ldata res
```

This result is shown in Fig. 5.1.

Now we check whether the same source signal would be detectable with a high background, i.e., a 3% and 1.5% higher background for the PIN and the GSO, respectively.

```
XSPEC12>cornorm 1 0.03 2 0.015
 Spectrum 1 correction norm set to 0.03
 Spectrum 2 correction norm set to 0.015

 Chi-Squared =          581.25 using 197 PHA bins.
 Reduced chi-squared =         2.9961 for    194 degrees of freedom
 Null hypothesis probability =   2.754551e-40
 Current data and model not fit yet.
XSPEC12>fit
                    Parameters
Chi-Squared  Lvl          1:nH    2:PhoIndex        3:norm
543.041       -2       2.65270       2.21924      0.127136
```

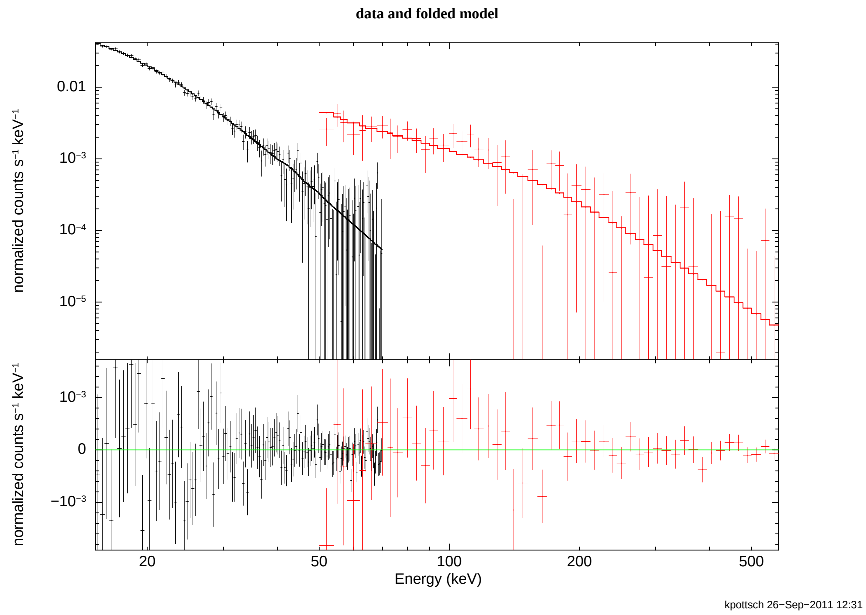

Figure 5.1: Simulation of an HXD observation of a 10 mCrab source with a Crab-like spectrum. Here, the cornorm of the two background files has been set to 0.

```
514.453       -2       4.29908       2.27391      0.153596
502.112       -2       15.5709       2.31955      0.180934
<more trials here>
440.297       -3       154.374       2.94577       1.56829
440.269       -3       155.874       2.95280       1.60683
440.268       -4       159.101       2.96827       1.69155
========================================
 Variances and Principal Axes
                 1        2        3
 9.4350E-06| -0.0006  -0.9792   0.2030
 7.0331E+02| -0.9997  -0.0042  -0.0232
 5.0198E-02| -0.0236   0.2030   0.9789
----------------------------------------

====================================
  Covariance Matrix
        1           2           3
   7.029e+02   2.946e+00   1.632e+01
   2.946e+00   1.443e-02   7.840e-02
```

```
   1.632e+01   7.840e-02   4.273e-01
------------------------------------

========================================================================
Model phabs<1>*powerlaw<2> Source No.: 1   Active/On
Model Model Component  Parameter  Unit     Value
 par  comp
   1    1   phabs      nH         10^22    159.101      +/-  26.5125
   2    2   powerlaw   PhoIndex            2.96827      +/-  0.120104
   3    2   powerlaw   norm                1.69155      +/-  0.653656
________________________________________________________________________


 Chi-Squared =         440.27 using 197 PHA bins.
 Reduced chi-squared =         2.2694 for    194 degrees of freedom
 Null hypothesis probability =   3.505307e-21
XSPEC12>plot ldata res
```

This result is shown in Fig.5.2, and it clear from the figure that in this case the signal is undetectable in the GSO band.

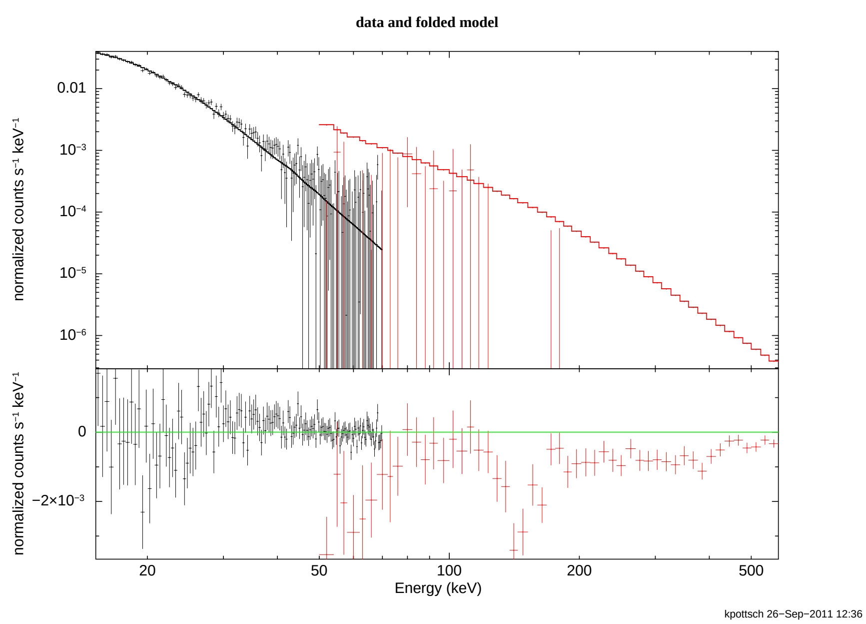

Figure 5.2: Simulation with the highest estimated background, for both the PIN and the GSO.

Finally, we check the source signal using low backgrounds.

```
XSPEC12>cornorm 1 -0.03 2 -0.015
 Spectrum 1 correction norm set to -0.03
 Spectrum 2 correction norm set to -0.015

 Chi-Squared =         911.15 using 197 PHA bins.
 Reduced chi-squared =        4.6967 for    194 degrees of freedom
 Null hypothesis probability =   2.974284e-93
 Current data and model not fit yet.
XSPEC12>fit
                    Parameters
Chi-Squared  Lvl          1:nH    2:PhoIndex        3:norm
808.384       -2       181.269       2.90266       1.54819
791.667       -2       174.773       2.84250       1.27043
772.645       -2       163.596       2.78155       1.03599
<more trials here>
434.587        0    0.00136529       1.83006     0.0445789
434.575        0   0.000110466       1.83001     0.0445767
434.575        6   0.000111649       1.83001     0.0445767
========================================
 Variances and Principal Axes
                 1        2        3
 1.4396E-07| -0.0000  -0.1354   0.9908
 1.4928E+02| -1.0000  -0.0006  -0.0001
 7.6104E-04| -0.0006   0.9908   0.1354
----------------------------------------

====================================
  Covariance Matrix
        1           2           3
   1.493e+02   8.576e-02   1.659e-02
   8.576e-02   7.964e-04   1.116e-04
   1.659e-02   1.116e-04   1.593e-05
------------------------------------

========================================================================
Model phabs<1>*powerlaw<2> Source No.: 1   Active/On
Model Model Component  Parameter  Unit     Value
 par  comp
   1    1   phabs      nH         10^22    1.11649E-04  +/-  12.2180
   2    2   powerlaw   PhoIndex            1.83001      +/-  2.82200E-02
```

```
   3    2   powerlaw   norm                4.45767E-02  +/-  3.99093E-03
________________________________________________________________________


 Chi-Squared =         434.58 using 197 PHA bins.
 Reduced chi-squared =         2.2401 for    194 degrees of freedom
 Null hypothesis probability =   1.748499e-20
XSPEC12>plot ldata res
```

The result is shown in 5.3 where now the GSO spectrum is largely above to model.

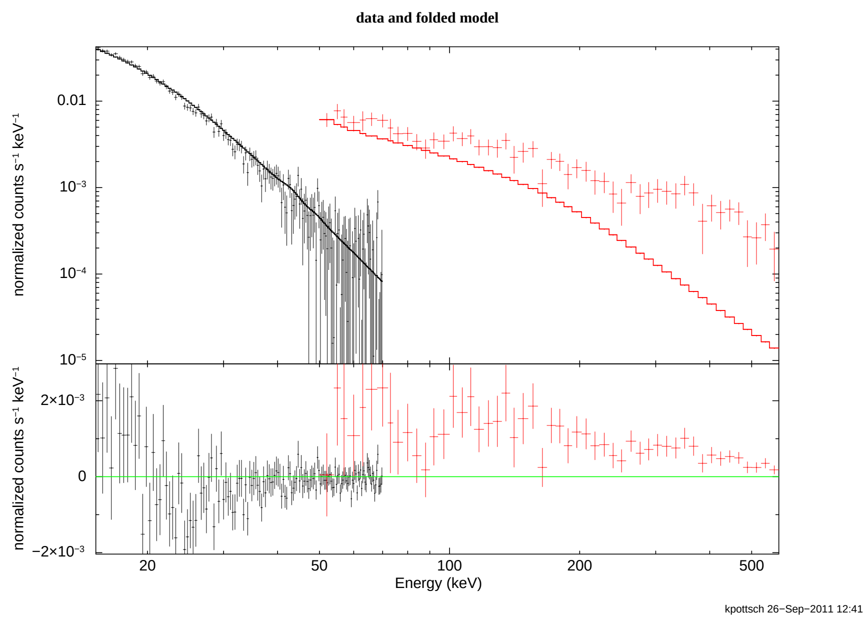

Figure 5.3: Simulation with the lowest estimated background, for both the PIN and the GSO.

By comparing the different fit results from these different runs, the overall uncertainties expected for the slope and normalization can be estimated.

5.6 XISSIM

`xissim` is a *Suzaku* XIS event simulator, based on the tool `xrssim`. It reads a FITS format photon list file, traces photon paths in the telescope (via ray-tracing), and outputs a simulated XIS event file. The XRT thermal shield transmission and the XIS detection efficiency are taken into account if requested. Each record of the photon list file describes the celestial positions, arrival time, and energy of the input photon. The `mkphlist` `FTOOL` can create such photon list files from FITS images (e.g., *ROSAT* HRI or *Chandra* images) and spectral models (which may be created in `XSPEC`). The `xissim` output event file may be analyzed just like observational data, using standard analysis tools such as `xselect`. `xissim` is part of the latest version of the `FTOOLS`.

5.7 MAKI

MAKI is another web-based interactive tool (see Appendix B) that can determine the orientation of the XIS CCDs on the sky as a function of the observation epoch within the visibility window of the target. For *Suzaku*, the orientation of the solar panels with respect to the spacecraft is fixed, and at the same time, the range of the angles between the vector normal to the solar panels and the vector pointing to the Sun is restricted, which in turn restricts the roll angle of the spacecraft.

When using the tool, general instructions are available via the "Help" button. In order to check the visibility and available roll angles for a target, first load an image. This can be done with either an existing FITS image, or by entering the RA and DEC of the source and clicking the "New Graph" button. This creates an image on which the *Suzaku* XIS field of view (FOV) will be shown.

The "Mission and Roll Selector" (in the upper right of the display) allows different instruments from different missions to be selected. Then the FOV will appear on your image. This can be rotated using the "Roll angle" slider bar.

5.8 RPS

The Remote Proposal Submission (RPS) tool must be used to enter the basic proposal data into the ISAS/JAXA, HEASARC, or ESA database. Proposers should make sure they use the appropriate RPS, since there are multiple reviews. See Appendix B for the list of RPS web-sites and addresses. Two versions of RPS are available: a character-oriented version, where the user submits all the required information via e-mail, or a web-oriented version.

One aspect of RPS that is not immediately obvious is how to specify time-constrained observations. For instance, a need for such an observation may arise for a study of a spectrum of a binary system at a particular orbital phase. If some particular aspect of the observation cannot be clearly specified in the RPS form, the user should detail it in the "comments" field of the RPS form and/or contact either the *Suzaku* team at ISAS/JAXA or the NASA *Suzaku* GOF before submitting.

5.9 Checklist

A successful *Suzaku* proposal, from a technical point of view, must include the following elements:

Coordinates: The PI is responsible for supplying the correct J2000 coordinates. For extended sources, specify single FOVs (coordinates for the center of XIS or the HXD) or rastering parameters (a schematic drawing overlaid on images would be the least ambiguous; equivalent textual descriptions are acceptable).

XIS count rate and exposure time: Explain how they were calculated (for a highly variable source, an added explanation — such as "excluding any bursts" — would be helpful).

HXD count rate and exposure time: If the source is not expected to be a hard X-ray source, this can be set to 0.0 since only the source counts are to be included.

Observing constraints, if any: These include monitoring, coordinated, phase-dependent, and roll-dependent observations; TOOs are allowed, but the triggering criteria and the probability of triggering must be spelled out in text, and summarized in target remarks.

While two default aim points were offered from AO-1 to AO-6 — the XIS nominal and the HXD nominal positions (the HXD aim point is at (DETX,DETY)=(-3.′5, 0) on the XIS image); the reduction in effective area for the non-selected instrument is $\sim 10\%$) — support for the HXD nominal position will be dropped in AO-7. This is done to mitigate effects due to the increased attitude jitter of *Suzaku* since the end of 2009. No observations with non-standard readout clocks (P-sum/Timing mode and Window/Burst options) will be carried out at the HXD nominal position. While the operation team does not prohibit observations at the HXD nominal point with a standard XIS mode response matrices will not be provided for such observations.

Note that Guest Observers are welcome to propose for targets already approved for in previous AOs (see the Announcement of Opportunity). However, in the interest of maximizing the scientific return from *Suzaku*, the proposal must explain why the already-approved observation(s) does/do not meet their scientific objectives. Valid reasons include a much longer exposure time, incompatible time constraints, or different positions within an extended source.

We also note that the XISs are subject to count rate limitations, because of possible multiple events in an XIS pixel within one frame. This is much less of a problem than with the ACIS aboard *Chandra*, as *Chandra*'s mirror focuses the X-ray flux onto a CCD area that is orders of magnitude smaller. The rule of thumb is that the XIS can tolerate a point source with a count rate up to ~ 40 cps per CCD with essentially no loss of counts or resolution. For brighter sources, these limitations can be reduced via a variety of XIS modes, such as the use of a sub-array of the XIS, as discussed in section 7.2.2.1.

Finally, it is important to remember that because the HXD is a non-imaging detector, contaminating sources in the field of view can significantly affect your results. The HXD field of view is defined by a collimator with a square opening. The FWHM of the field of view is $34'.4 \times 34'.4$ below ~ 100 keV and $4^\circ.6 \times 4^\circ.6$ above ~ 100 keV. Considering that twice the FWHM value is required to completely eliminate the contamination in a collimator-type detector, and the source may happen to be located at the diagonal of the square, nearby bright sources within a radius of $50'$ and $6^\circ.5$ from the aim point can contaminate the data in the energy band below and above ~ 100 keV, respectively. If you specify the roll-angle to avoid the source, the limit will be reduced to $\sim 35'$ and $\sim 4^\circ.6$, respectively. It is the proposer's responsibility to show that any source with a flux level comparable to or brighter than that of the target of interest does not exist within these ranges. The proposer can, e.g., check this by using the hard X-ray source catalogs from such satellites as *RXTE*-ASM, *INTEGRAL*, and *Swift*, among others.

5.10 Additional Requirements for US Proposers

There are two additional NASA-specific proposal rules that must be followed by US-based proposers:

1. Proposals to NASA must be submitted through `ARK/RPS`. The user interface of `ARK/RPS` is similar to that of the "classic" `RPS` except that the PI must first create an `ARK` account and/or join the *Suzaku*`RPS group`. Having done so, the *Suzaku*`RPS` form can be accessed via `ARK/RPS`.

2. The estimated level of effort (in FTEs) of any NASA civil servants among the team (PI or Co-Is) must be entered into the `ARK/RPS` form. Enter 0 if no NASA civil servant is part of the team.

Chapter 6

X-Ray Telescopes (XRT)

Suzaku has five light-weight thin-foil X-Ray Telescopes (XRTs). The XRTs have been developed jointly by NASA/GSFC, Nagoya University, Tokyo Metropolitan University, and ISAS/JAXA. These are grazing-incidence reflective optics consisting of compactly nested, thin conical elements. Because of the reflectors' small thickness, they permit high density nesting and thus provide large collecting efficiency with a moderate imaging capability in the energy range of 0.2–12 keV, all accomplished in telescope units under 20 kg each.

Four XRTs on-board *Suzaku* are used for the XIS (XRT-I), and the remaining XRT is for the XRS (XRT-S). XRT-S is no longer functional. The XRTs are arranged on the Extensible Optical Bench (EOB) on the spacecraft in the manner shown in Fig. 6.1. The external dimensions of the 4 XRT-Is are the same (see Table 6.1, which also includes a comparison with the ASCA telescopes).

The angular resolutions of the XRTs range from $1'.8$ to $2'.3$, expressed in terms of half-power diameter, which is the diameter within which half of the focused X-rays are enclosed. The angular resolution does not significantly depend on the energy of the incident X-rays in the energy range of *Suzaku*, 0.2–12 keV. The effective areas are typically 440 cm^2 at 1.5 keV and 250 cm^2 at 8 keV. The focal length of the XRT-I is 4.75 m. Actual focal lengths of the individual XRT quadrants deviate from the design values by a few cm. The optical axes of the quadrants of each XRT are aligned to within $2'$ from the mechanical axis. The field of view for the XRT-Is is about $17'$ at 1.5 keV and $13'$ at 8 keV (see also Table 3.1).

6.1 Basic XRT Components

The *Suzaku* X-Ray Telescopes (XRTs) consist of closely nested thin-foil reflectors, reflecting X-ray at small grazing angles. An XRT is a cylindrical structure, having the following layered components: 1. a thermal shield at the entrance aperture to help maintain a uniform temperature, 2. a pre-collimator mounted on metal rings for stray light elimination,

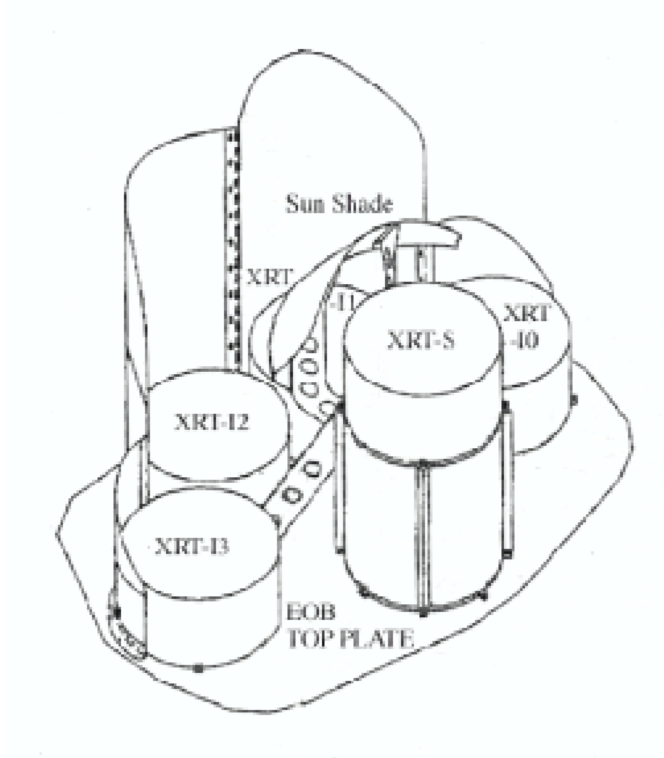

Figure 6.1: Layout of the XRTs on the *Suzaku* spacecraft.

	Suzaku XRT-I	ASCA
Number of telescopes	4	4
Focal length	4.75 m	3.5 m
Inner diameter	118 mm	120 mm
Outer diameter	399 mm	345 mm
Height	279 mm	220 mm
Mass per telescope	19.5 kg	9.8 kg
Number of nested shells	175	120
Reflectors per telescope	1400	960
Geometric area per telescope	873 cm^2	558 cm^2
Reflecting surface	gold	gold
Substrate material	aluminum	aluminum
Substrate thickness	155 μm	127 μm
Reflector slant height	101.6 mm	101.6 mm

Table 6.1: Telescope dimensions and parameters of XRT-I.

Figure 6.2: A *Suzaku* X-ray telescope.

3. a primary stage for the first X-ray reflection, 4. a secondary stage for the second X-ray reflection, 5. a base ring for structural integrity and interfacing with the EOB of the spacecraft. All these components, except the base rings, are constructed in 90° segments. Four of these quadrants are coupled together by interconnect-couplers and also by the top and base rings (Fig. 6.2). The telescope housings are made of aluminum for an optimal strength to mass ratio. Each reflector consists of a substrate also made of aluminum and an epoxy layer that couples the reflecting gold surface to the substrate.

Including the alignment bars, collimating pieces, screws and washers, couplers, retaining plates, housing panels and rings, each XRT-I consists of over 4112 mechanically separated parts. In total, nearly 7000 qualified reflectors were used and over 1 million cm^2 of gold surface was coated.

6.1.1 Reflectors

In shape, each reflector is a 90° segment of a section of a cone. The cone angle is designed to be the angle of on-axis incidence for the primary stage and 3 times that for the secondary stage. They are 101.6 mm in slant length, with radii extending approximately from 60 mm at the inner part to 200 mm at the outer part. The reflectors are nominally 178 μm in thickness. All reflectors are positioned with grooved alignment bars, which hold the foils at their circular edges. There are 13 alignment bars at the face of each quadrant, separated by $\sim$6.4°.

To properly reflect and focus X-ray at grazing incidence, the precision of the reflector figure and the smoothness of the reflector surface are important aspects. Since polishing of thin reflectors is both impractical and expensive, reflectors in *Suzaku* XRTs acquire their surface smoothness by a replication technique and their shape by thermo-forming of aluminum. In the replication method, metallic gold is deposited on an extrusion glass mandrel ("replication mandrel"), the surface of which has sub-nanometer smoothness over a wide spatial frequency, and the substrate is subsequently bonded with the metallic film with a layer of epoxy. After the epoxy is hardened, the substrate-epoxy-gold film composite can be removed from the glass mandrel and the replica acquires the smoothness of the glass. The replica typically has $\sim$0.5 nm rms roughness at mm or smaller spatial scales, which is sufficient for excellent reflectivity at incident angles less than the critical angle. The *Suzaku* XRTs are designed with on-axis reflection at less than the critical angle, which is approximately inversely proportional to X-ray energy.

In the thermo-forming of the substrate, pre-cut, mechanically rolled aluminum foils are pressed onto a precisely shaped "forming mandrel", which is not the same as the replication mandrel. The combination is then heated until the aluminum softens. The aluminum foils acquire the shape of the properly shaped mandrel after cooling and release of pressure. In the *Suzaku* XRTs, the conical approximation of the Wolter-I type geometry is used. This approximation fundamentally limits the angular resolution achievable. More significantly, the combination of the shape error in the replication mandrels and the imperfection in the thermo-forming process (to about 4 μm in the low frequency components of the shape error in the axial direction) limits the angular resolution to about $1'$.

6.1.2 Pre-Collimator

The pre-collimator, which blocks stray light that otherwise would enter the detector at a larger angle than intended, consists of concentrically nested aluminum foils, similar to those of the reflector substrates. They are shorter, 22 mm in length, and thinner, 120 μm in thickness. They are positioned in a fashion similar to that of the reflectors, by 13 grooved aluminum plates at each circular edge of the pieces. They are installed on top of their respective primary reflectors along the axial direction. Due to their smaller thickness, they do not significantly reduce the entrance aperture in that direction more than the reflectors already do. Pre-collimator foils do not have reflective surfaces (neither front nor back). The relevant dimensions are listed in Table 6.2.

	XRT-I
Number of collimators	4
Height	32 mm
Blade substrate	aluminum
Blade thickness	120 μm
Blade height	22 mm
Height from blade top to reflector top	30 mm
Number of nested shells	175
Blades per telescope	700
Mass per collimator	2.7 kg

Table 6.2: Design parameters for the pre-collimator.

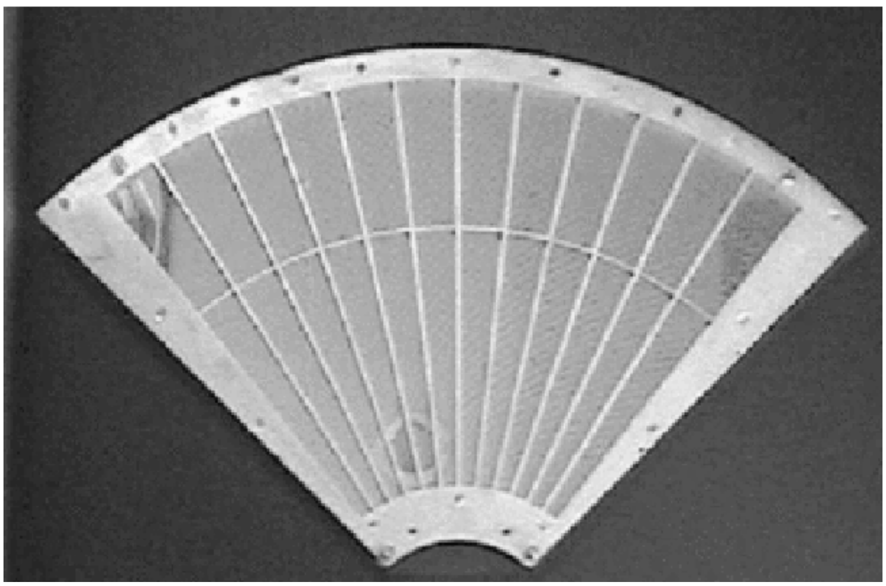

Figure 6.3: A thermal shield.

6.1.3 Thermal Shields

The *Suzaku* XRTs are designed to function in a thermal environment of 20±7.5°C. The reflectors, due to their composite nature and thus their mismatch in coefficients of thermal expansion, suffer from thermal distortion that degrades the angular resolution of the telescopes for temperatures outside this range. Thermal gradients also distort the telescope on a larger scale. Even though sun shields and other heating elements on the spacecraft help in maintaining a reasonable thermal environment, thermal shields are integrated on top of the pre-collimator stage to provide the needed thermal control.

6.2 In-Flight Performance

In this section we describe the in-flight performance and calibration of the *Suzaku* XRTs. There are no data to verify the in-flight performance of the XRT-S, therefore we hereafter concentrate on the four XRT-I modules (XRT-I0 through I3) which focus incident X-rays on the XIS detectors. Several updates of the XRT-related calibration were made in July 2008.

6.2.1 Focal Positions

A point-like source, MCG−6-30-15, was observed at the XIS aim point during 2005 August 17-18. Fig. 6.4 shows the focal position of the XRT-Is, that the source is found at on the XISs, when the satellite points at it using the XIS aim point. The focal positions are located close to the detector center with a deviation of 0.3 mm from each other. This implies that the fields of view of the XISs coincide to within $\sim 0\overset{\prime}{.}3$.

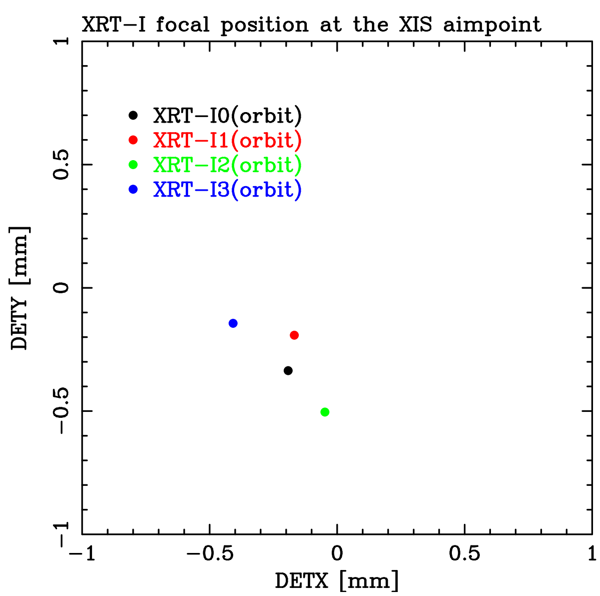

Figure 6.4: Focal positions on the XISs when the satellite points at MCG−6-30-15 using the XIS aim point.

6.2.2 Optical Axis

The maximum transmission of each telescope module is achieved when a target star is observed along the optical axis. The optical axes of the four XRT-I modules are, however, expected to scatter in an angular range of $\sim 1'$. Accordingly, we have to define the axis to be used for real observations that provides a reasonable compromise among the four optical axes. We hereafter refer to this axis as the observation axis.

In order to determine the observation axis, we have first searched for the optical axis of each XRT-I module by observing the Crab nebula at various off-axis angles. The observations of the Crab nebula were carried out in 2005 and 2006. Hereafter all the off-axis angles are expressed in the detector coordinate system DETX/DETY (see `ftp://legacy.gsfc.nasa.gov/suzaku/doc/xis/suzakumemo-2006-39.pdf`.

By fitting a model comprising of a Gaussian plus a constant to the count rate data as a function of the off-axis angle, we have determined the optical axis of each XRT-I module. The result is shown in Fig. 6.5.

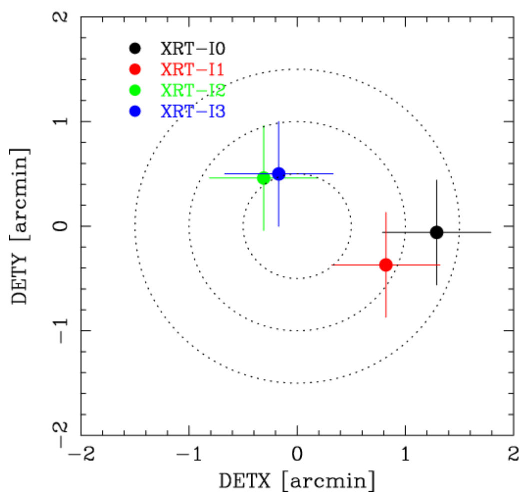

Figure 6.5: Locations of the optical axis of each XRT-I module in the focal plane determined from the observations of the Crab nebula in 2005 August–September. This figure implies that the image on each XIS detector becomes brightest when a target star is placed at the position of the corresponding cross. The dotted circles are drawn every 30″ in radius from the XIS-default position (see text).

Since the optical axes moderately scatter around the origin, we have decided to adopt it as the default observation axis for XIS-oriented observations. Hereafter we refer to this axis as the XIS-default orientation, or equivalently, the XIS-default position. The optical axis of the XRT-I0 shows the largest deviation of $\sim 1.'3$ from the XIS-default position. Nevertheless, the efficiency of the XRT-I0 at the XIS-default position is more than 97%, even at 8–10 keV, the highest energy band (see Fig. 6.10). The optical axis of the HXD PIN detector, on the other hand, deviates from this default by $\sim 5'$ in the negative DETX direction (see for example, the instrument paper at `ftp://legacy.gsfc.nasa.gov/suzaku/doc/hxd/suzakumemo-2006-37.pdf`). Because of this, the observation efficiency of the HXD PIN at the XIS-default orientation is reduced to ∼93% of the on-axis value. We thus provide another default pointing position, the

HXD-default position, for HXD-oriented observations, at $(-3'.5, 0')$ in DETX/DETY coordinates. At the HXD-default position, the efficiency of the HXD PIN is nearly 100%, whereas that of the XIS is ~88% on average.

6.2.3 Effective Area

In-flight calibration of the effective area has been carried out with version 2.1 processed data of the Crab nebula both at the XIS- and HXD-default positions. The observations were carried out in 2005 September 15–16. The data were taken in the normal mode with the 0.1 s burst option in which the CCD is exposed during 0.1 s out of the full-frame read-out time of 8 s, in order to avoid the event pile-up and the telemetry saturation. The exposure time of 0.1 s is, however, comparable to the frame transfer time of 0.025 s. As a matter of fact, the Crab image is elongated in the frame-transfer direction due to so-called the out-of-time events, as shown in Fig. 6.6.

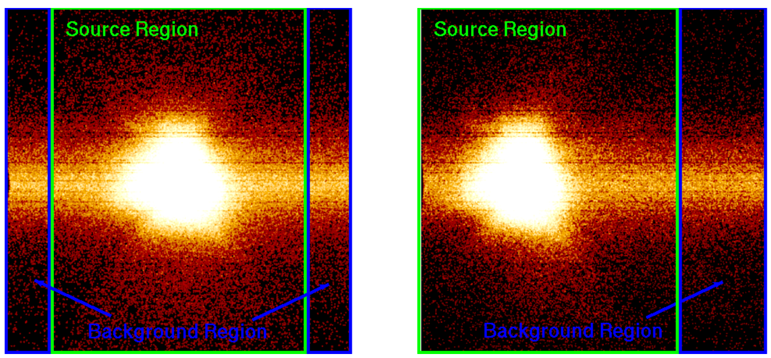

Figure 6.6: The source- and background-integration regions overlaid on the Crab images taken with XIS1 at the XIS-default position (left) and the HXD-default position (right) on 2005 September 15–16. The images are elongated in the frame-transfer direction due to the out-of-time events (see text). In order to cancel these events, the background regions with a size of 126 by 1024 pixels each are taken at the left and right ends of the chip for the XIS-default position, and a single region with a size of 252 by 1024 pixels is taken at the side far from the Crab image for the HXD-default position. The remaining source-integration region has a size of 768 by 1024 pixels, or $13'.3 \times 17'.8$. The background subtraction is carried out after area-size correction.

Accordingly, the background-integration regions with a size of 126 by 1024 pixels are taken at the left and right ends of the chip for the XIS-default position, perpendicularly to the frame-transfer direction, as shown in the left panel of Fig. 6.6. For the observation at the HXD-default position, the image center is shifted from the XIS-default position in the direction perpendicular to the frame-transfer direction for XIS0 and XIS3. Hence we can adopt the same background-integration regions as those of the XIS-default position for these two XIS modules. For XIS1 and XIS2, on the other hand, the image shift occurs in the frame-transfer direction, as shown in the right panel of Fig. 6.6. We thus take a single background-integration region with a size of 252 by 1024 pixels at the far side from the Crab image for the HXD-default position of these two detectors. As a result, the remaining source-integration region has a size of 768 by 1024 pixels, or $13'.3 \times 17'.8$ for all the cases, which is wide enough to collect all the photons from the Crab nebula.

After subtracting the background, taking into account the sizes of the regions, we have fitted the spectra taken with the four XIS modules with a model composed of a power law undergoing photoelectric absorption using `xspec` Version 11.2. For the photoelectric absorption, we have adopted the model `phabs` with the cosmic metal abundances of Anders & Grevesse (1989, Geochim. Cosmochim. Acta, 53, 197). First, we let all parameters vary independently for all the XIS modules. The results are summarized for the XIS/HXD nominal positions separately in Table 6.3 and are shown in Fig. 6.7.

Table 6.3: Best-fit parameters of the power law model fits to the Crab spectra taken on 2005 September 15–16.

Sensor ID	N_H	Photon Index	Normalization	Flux	χ^2_ν (d.o.f.)
		XIS-default position			
XIS0	0.311±0.015	2.077±0.017	$9.38^{+0.24}_{-0.23}$	2.086	1.02 (89)
XIS1	0.294±0.014	2.085±0.017	$9.73^{+0.23}_{-0.22}$	2.141	1.59 (89)
XIS2	0.282±0.015	2.065±0.017	$9.29^{+0.23}_{-0.22}$	2.134	1.34 (89)
XIS3	0.304±0.015	2.082±0.017	$9.33^{+0.24}_{-0.23}$	2.062	1.34 (89)
PIN	0.3 (fix)	2.101±0.008	11.41±0.26	2.464	0.74 (72)
		HXD-default position			
XIS0	0.304±0.018	2.079±0.021	$9.13^{+0.27}_{-0.26}$	2.025	1.28 (89)
XIS1	0.295±0.016	2.111±0.021	$9.59^{+0.27}_{-0.26}$	2.030	0.86 (89)
XIS2	0.282±0.016	2.070±0.019	$9.54^{+0.26}_{-0.25}$	2.151	1.22 (89)
XIS3	$0.301^{+0.017}_{-0.016}$	2.085±0.019	9.29±0.25	2.043	1.19 (89)
PIN	0.3 (fix)	2.090±0.009	10.93±0.27	2.400	0.82 (72)

N_H: Hydrogen column density in $10^{22}\,cm^{-2}$.
Normalization: Power-law normalization in photons $cm^{-2}s^{-1}keV^{-1}$ at 1 keV.
Flux: Energy flux in $10^{-8}\,cm^{-2}s^{-1}$ in the 2–10 keV band.

For the fit, we have adopted the ARFs and RMFs generated using CALDB 2008-07-09. These ARFs are made for a point source, whereas the Crab nebula is slightly extended ($\sim 2'$). We thus have created ARFs by utilizing the ray-tracing simulator (Misaki et al. 2005, Appl. Opt., 44, 916) with a *Chandra* image as input, and have confirmed that the difference of the effective area between these two sets of ARFs is less than 1%. We have neglected the energy channels below 1 keV, above 10 keV, and in the 1.5–2.0 keV band because of insufficient calibration related to uncertainties of the nature and amount of the contaminant on the OBF and to the Si edge structure (see `ftp://legacy.gsfc.nasa.gov/suzaku/doc/hxd/suzakumemo-2006-35.pdf`). Data in the 1.5–2.0 keV range are retrieved after the fit and shown in Fig. 6.7.

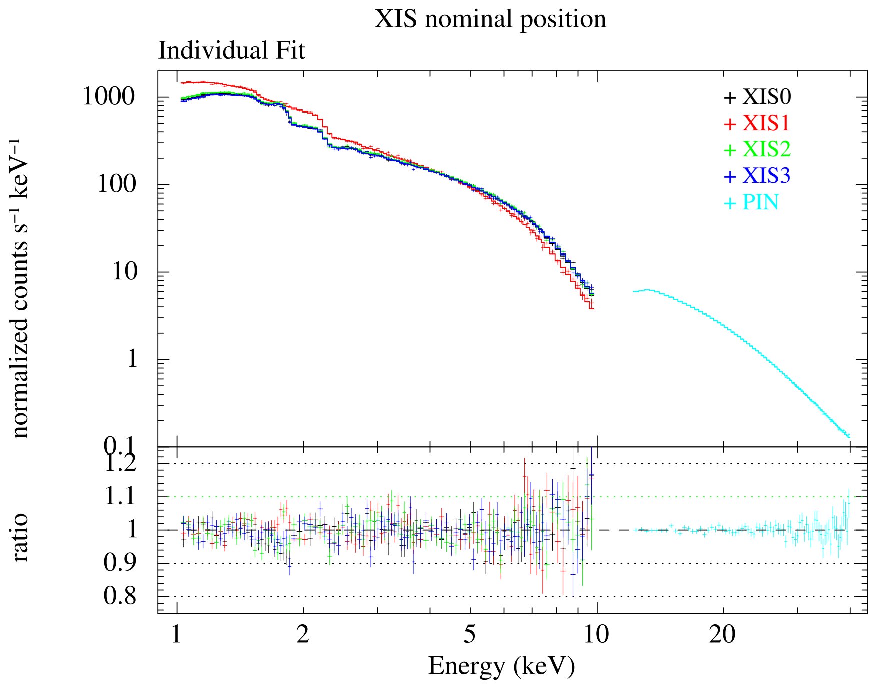

Figure 6.7: Power-law fit to the Crab spectra of all four XIS modules taken at the XIS-default position. All the parameters are allowed to vary independently for each XIS module. The fit is carried out in the 1.0–10.0 keV band, excluding the 1.5–2.0 keV interval where large systematic uncertainties associated with the Si K-edge remain. This energy range is retrieved after the fit.

Toor & Seward (1974, AJ, 79, 995) compiled the results from a number of rocket and balloon measurements available at that time, and derived the photon index and the normalization of the power law of the Crab nebula to be 2.10 ± 0.03 and 9.7 photons $\mathrm{cm}^{-2}\ \mathrm{s}^{-1}\ \mathrm{keV}^{-1}$ at 1 keV, respectively. Overlaying photoelectric absorption with $N_{\rm H} = 3 \times 10^{21}\ \mathrm{cm}^{-2}$, we obtain the flux to be 2.1×10^{-8} erg $\mathrm{cm}^{-2}\ \mathrm{s}^{-1}$ in the 2–10 keV band. The best-fit parameters of all the XIS modules at the XIS- and HXD-default positions are close to these standard values.

Since the best-fit parameters of the four XIS modules are close to the standard values, we have attempted to constrain the photon index to be the same for all the detectors. The best-fit parameters are summarized in Table 6.4.

The hydrogen column density $(0.28–0.32)\times10^{22}\ \mathrm{cm}^{-2}$ and the photon index 2.09 ± 0.01 are consistent with the standard values.

Table 6.4: Best-fit parameters of the contemporaneous power-law fits to the Crab spectra taken in 2005 September 15–16.

Sensor ID	N_H	Photon Index	Normalization	Flux	χ^2_ν (d.o.f.)
		XIS-default position			
XIS0	0.321±0.009	2.090±0.006	9.55±0.10	2.080	1.24 (432)
XIS1	0.298±0.008		9.79±0.10	2.14	
XIS2	0.302±0.008		9.72±0.10	2.13	
XIS3	0.311±0.009		9.43±0.10	2.06	
PIN	0.3 (fix)		11.06±0.11	2.42	
		HXD-default position			
XIS0	0.307±0.011	2.086±0.007	$9.19^{+0.12}_{-0.11}$	2.019	1.13 (432)
XIS1	0.277±0.009		9.28±0.11	2.11	
XIS2	0.298±0.010		9.74±0.11	2.21	
XIS3	0.300±0.010		9.28±0.15	2.11	
PIN	0.3 (fix)		10.80±0.01	2.45	

N_H : Hydrogen column density in $10^{22}\,\mathrm{cm}^{-2}$.
Normalization : Power-law normalization in photons $\mathrm{cm}^{-2}\mathrm{s}^{-1}\mathrm{keV}^{-1}$ at 1 keV.
Flux : Energy flux in $10^{-8}\,\mathrm{cm}^{-2}\mathrm{s}^{-1}$ in the 2–10 keV band.

6.2.4 Vignetting

The vignetting curves calculated by the ray-tracing simulator are compared with the observed intensities of the Crab nebula at various off-axis angles in Figs. 6.8–6.10.

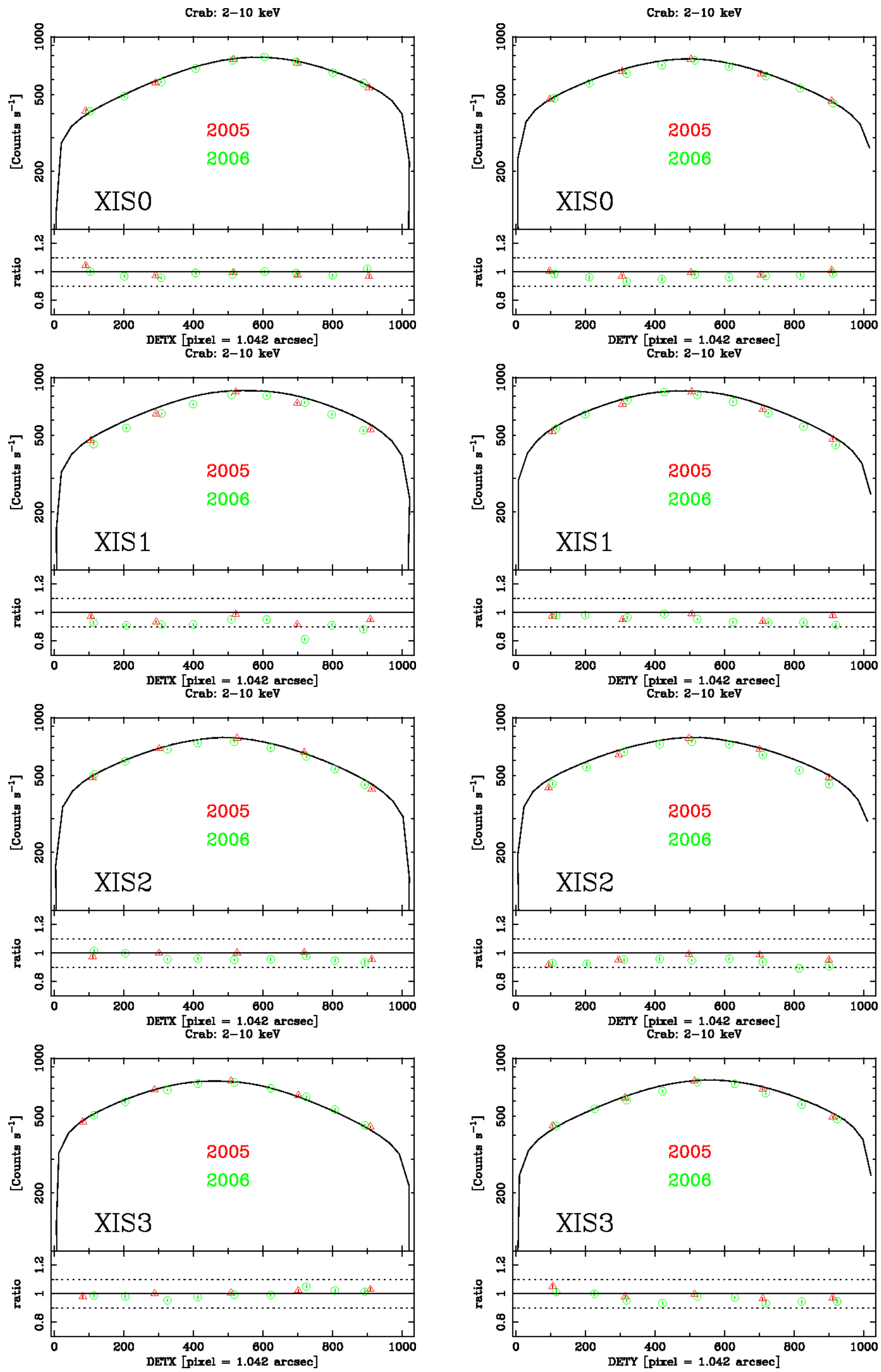

Figure 6.8: Count rates of the Crab pointings offset in DETX (left) and DETY (right) in the 2–10 keV band. Red and green symbols correspond to the data during 2005 and 2006, respectively. The solid line corresponds to the output of the ray-tracing simulator `xissim`. The bottom panels show the ratios of the data to the simulator output.

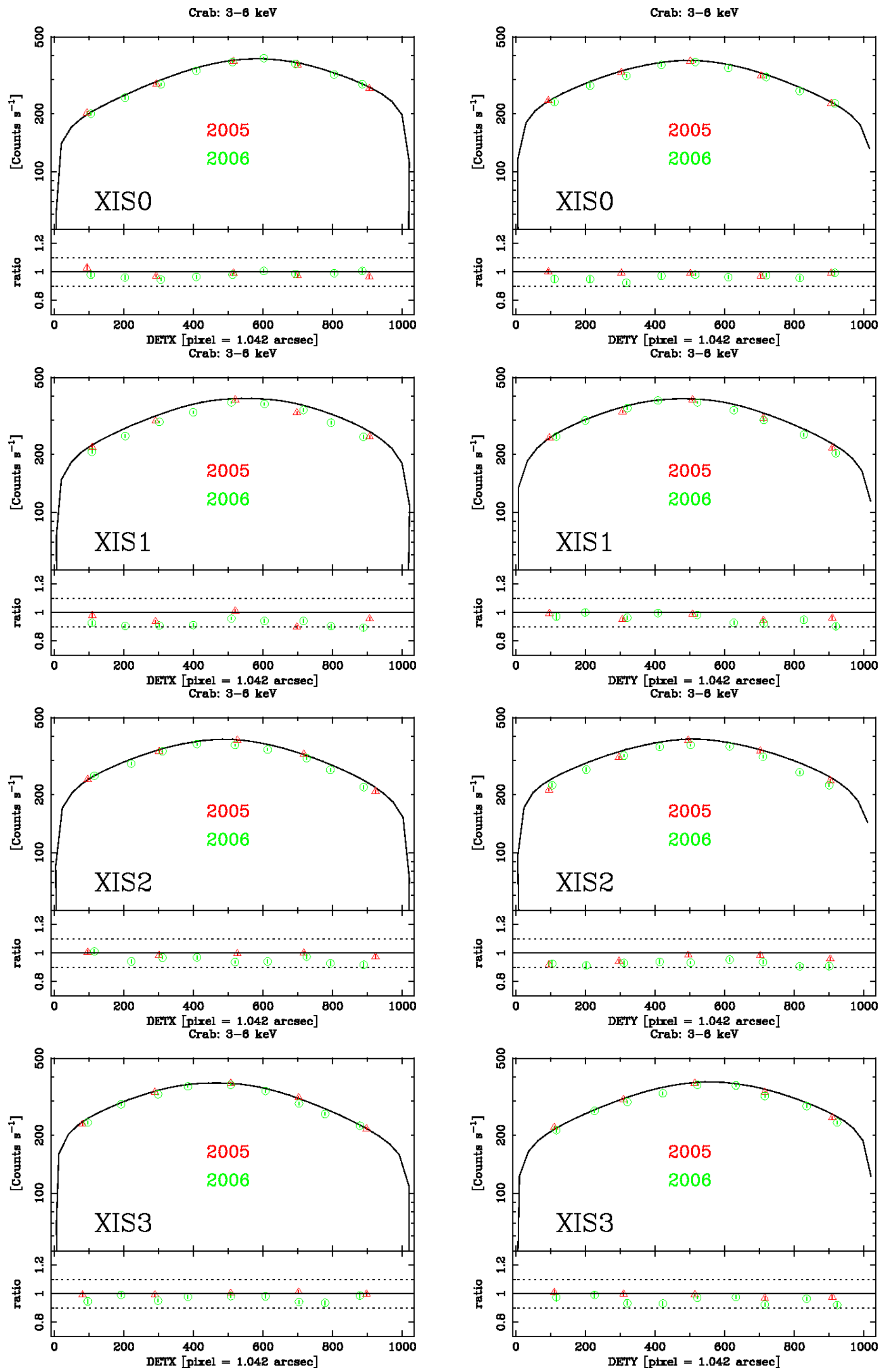

Figure 6.9: The same as Fig.6.8 but in the 3–6 keV band.

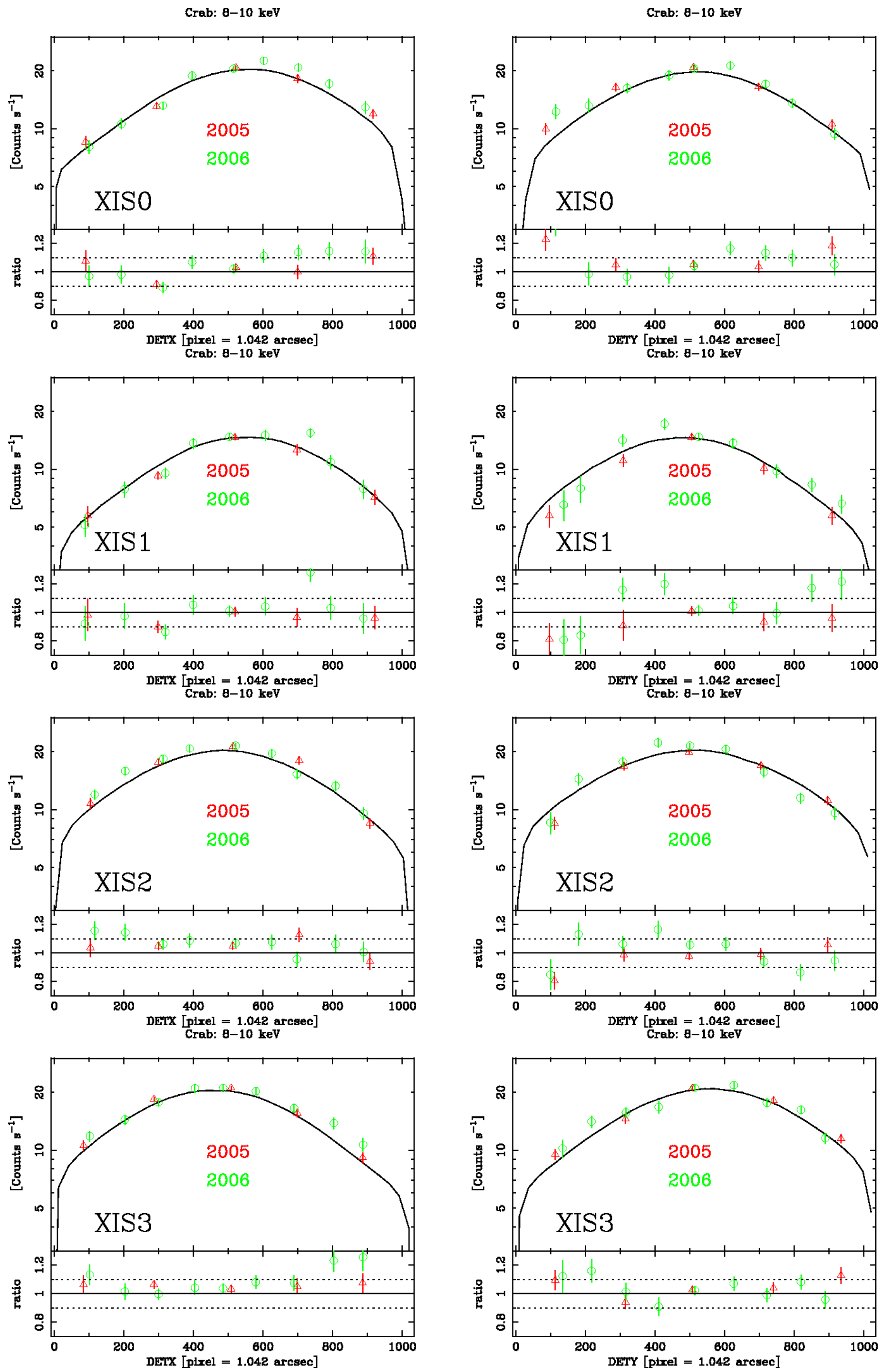

Figure 6.10: The same as Fig.6.8 but in the 8–10 keV band.

We have utilized the data of the Crab nebula taken during 2005 August and 2006 August. In the figures, we have drawn the vignetting curves for the energy bands 2–10 keV, 3–6 keV and 8–10 keV. To obtain this, we first assume the spectral parameters of the Crab nebula to be a power law with $N_{\rm H} = 0.33 \times 10^{22}\,{\rm cm}^{-2}$, photon index=2.09, and normalization=9.845 photons $\rm cm^{-2}\ s^{-1}\ keV^{-1}$ at 1 keV. These values are the averages of the four detectors at the XIS-default position (Table 6.4). We then calculate the count rate of the Crab nebula on the entire CCD field of view in $0.'5$ steps in both the DETX and DETY directions using the ray-tracing simulator. Note that the abrupt drop of the model curves at $\sim 8'$ is due to the source approaching the detector edge. On the other hand, the data points provide the real count rates in the corresponding energy bands within an aperture of $13.'3$ by $17.'8$. Note that the aperture adopted for the observed data can collect more than 99% of the photons from the Crab nebula, and hence the difference of the integration regions between the simulation and the observation does not matter. Finally, we re-normalize both the simulated curves and the data so that the count rate of the simulated curves at the origin becomes equal to unity.

These figures roughly show that the effective area is calibrated within ∼5% over the XIS field of view, except for the 8–10 keV band of XIS1. The excess of these XIS1 data points at the XIS-default position has already been seen in Fig. 6.7 (see also Table 6.3).

6.2.5 Angular Resolution

As shown in Serlemitsos et al. (2007), verification of the imaging capability of the XRTs has been made with the data of SS Cyg in quiescence taken on 2005 November 2 01:02UT–23:39UT. The total exposure time was 41.3 ks. SS Cyg is selected for this purpose because it is a point source and moderately bright (3.6, 5.9, 3.7, and 3.5 counts $\rm s^{-1}$ for XIS0 through XIS3), and hence, it is not necessary to care about pile-up even at the image core. In Fig. 6.11, we give the images of all the XRT-I modules thus obtained. The HPD is obtained to be $1.'8$, $2.'3$, $2.'0$, and $2.'0$ for XRT-I0, 1, 2, and 3, respectively.

In Fig. 6.11, we also show corresponding images produced by the updated "new" simulator `xissim` (version 2008-04-05). The simulator has been tuned for each quadrant. Therefore, the simulated images look different from quadrant to quadrant. More local or spiky structures seen in the observed images, however, are not reproduced.

In Fig. 6.12, we show Point Spread Functions (PSFs) using the data shown in Fig. 6.11 before smoothing. Note that the core shape within $0.'2$ is not tuned at all. The core broadening is mainly due to the attitude error of the satellite control (Uchiyama et al. 2007). In Fig. 6.13, we show encircled energy functions (EEFs). The reproducibility of the EEF is important when extracting spectra from a circular region with a given radius. In the new simulator, the EEF of the simulations coincides with that of the observed data to within 4% for radii from $1'$ to $6'$.

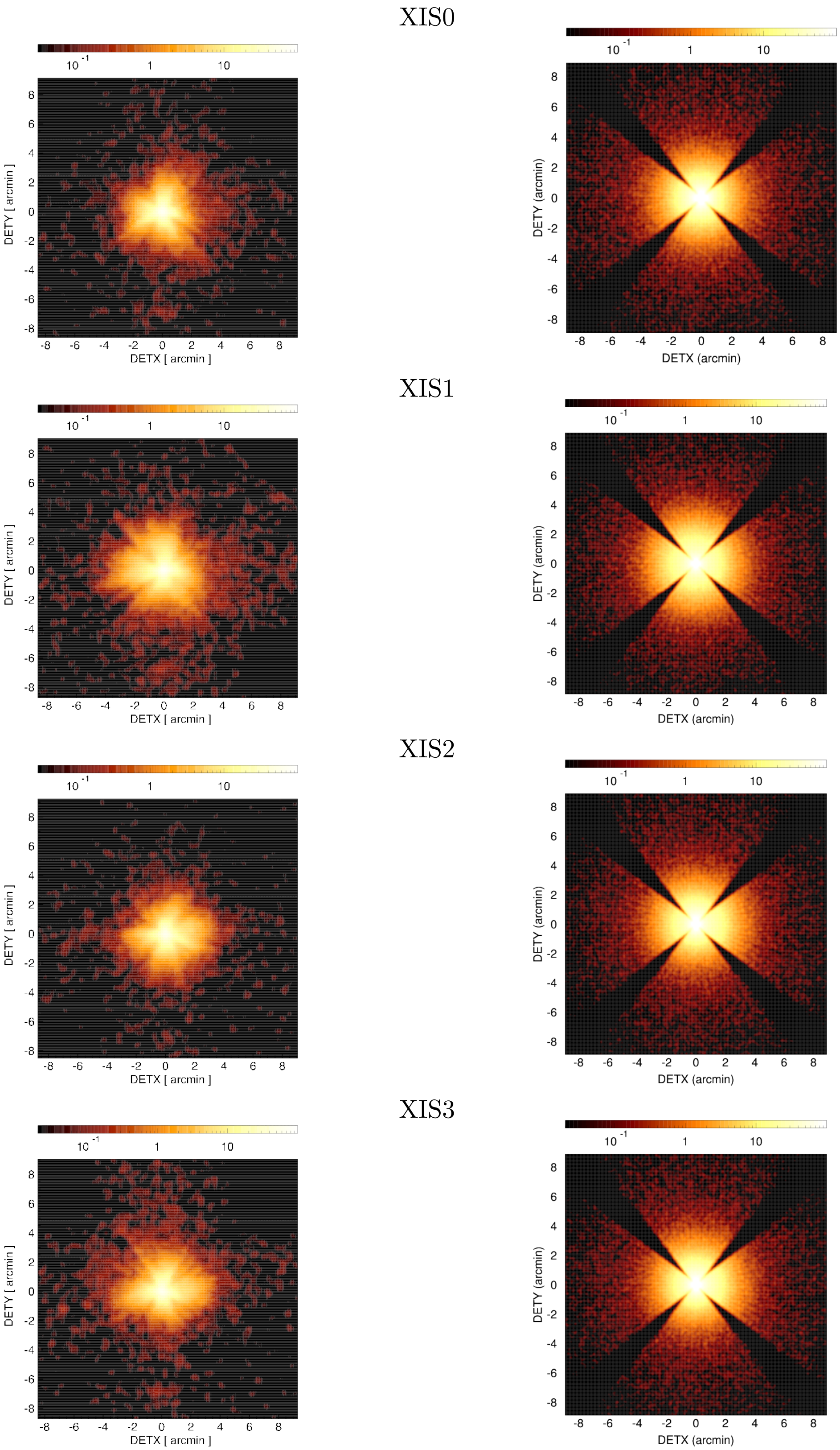

Figure 6.11: Images of the four XRT-I modules in the focal plane: SS Cyg (left) and simulation (right). All the images are binned to 2×2 pixels and then smoothed with a Gaussian with a sigma of 3 pixels, where the pixel size is 24 μm. The Fe55 events were removed from the SS Cyg image.

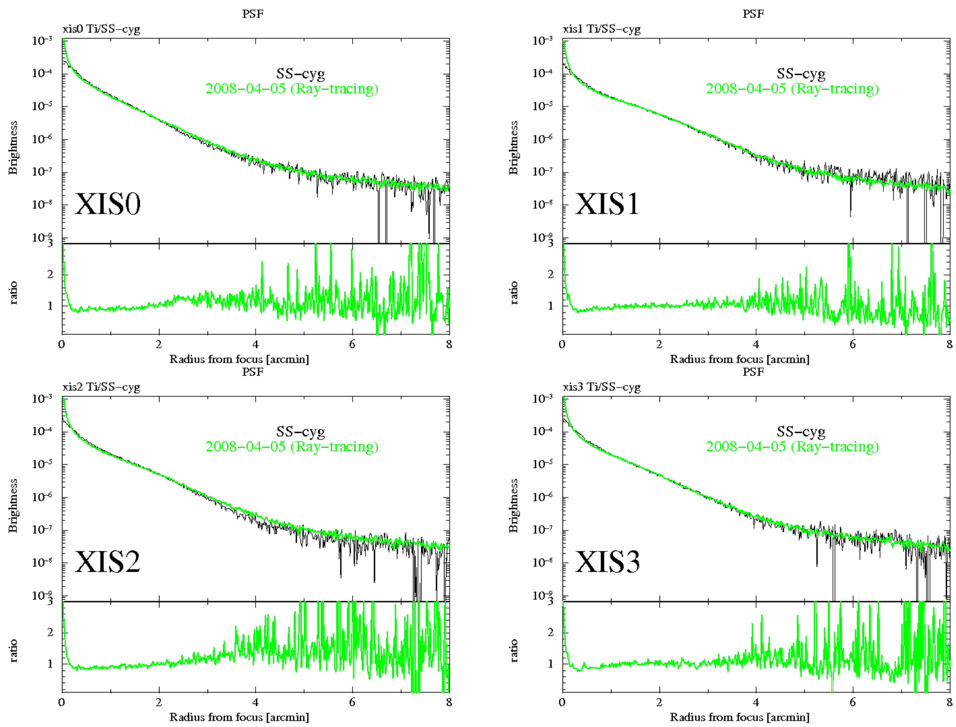

Figure 6.12: PSF of the four XRT-I images. The lower panels show the ratio between the observed and simulated data.

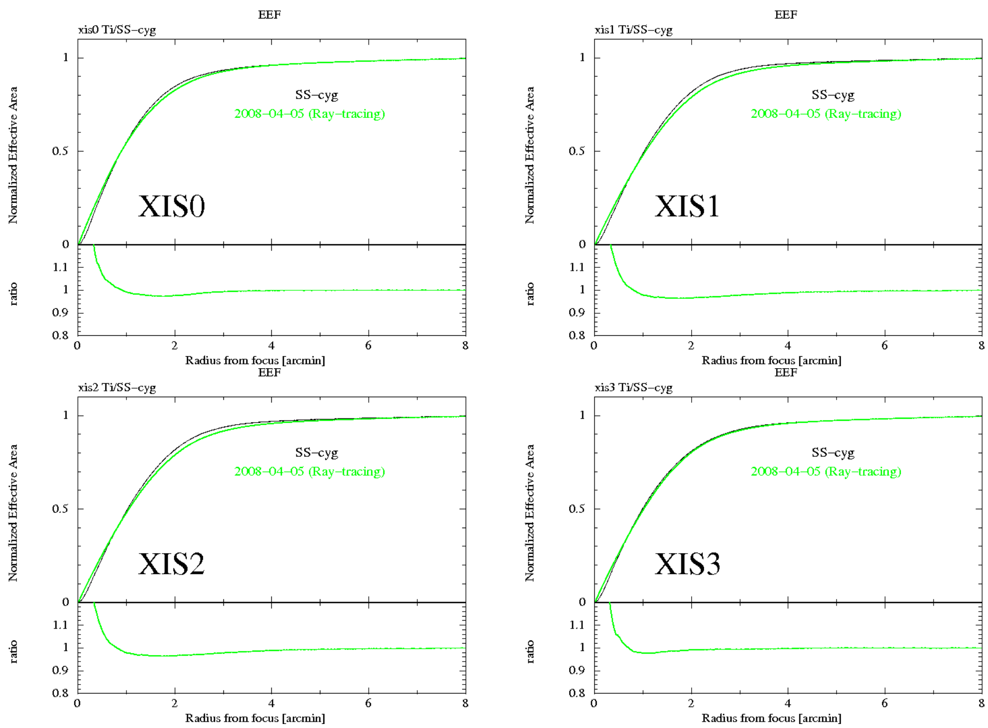

Figure 6.13: EEF of the four XRT-I images. The EEF is normalized to unity at the edge of the CCD chip (a square of $17'.8$ on the side). The lower panels show the ratio between the observed and simulated data.

6.2.6 Stray Light

Studies of the stray light were carried out with Crab nebula off-axis pointings during 2005 August 22 – September 16 for a range of off-axis angles. An example of a stray light image is shown in the right panel of Fig. 6.14.

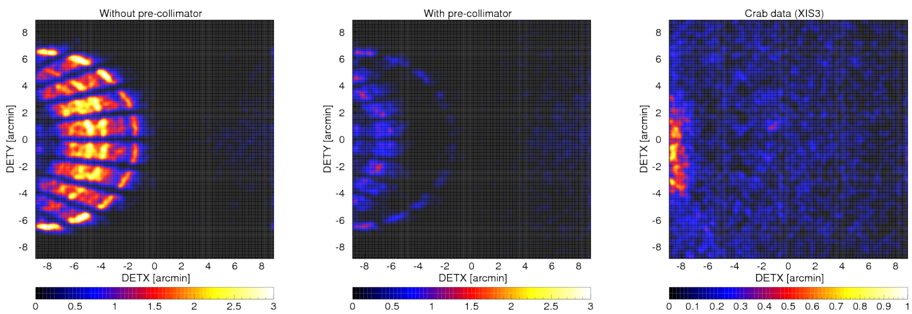

Figure 6.14: Focal plane images formed by stray light. The left and middle panels show simulated images of a monochromatic point-like source of 4.51 keV located at $(-20', 0')$ in (DETX, DETY) without and with the pre-collimator, respectively. The radial dark lanes are the shadows of the alignment bars. The right panel is the in-flight stray image of the Crab nebula in the 2.5–5.5 keV energy band located at the same off-axis angle. The unit of the color scale of this panel is counts per 16 pixels over the entire exposure time of 8428.8 s. The count rate from the whole image is 0.78 ± 0.01 counts s^{-1} including background. Note that the intensity of the Crab nebula measured with XIS3 at the XIS-default position is 458 ± 3 counts s^{-1} in the same 2.5–5.5 keV band. All images are binned to 2×2 pixels and then smoothed with a Gaussian with a sigma of 2 pixels, where the pixel size is 24 μm.

This image is taken with the XIS3 in the 2.5–5.5 keV band with the Crab nebula offset at $(-20', 0')$ in (DETX, DETY). The left and central panels show simulated stray light images without and with the pre-collimator, respectively, of a monochromatic point source of 4.5 keV being located at the same off-axis angle. The ghost image seen in the left half of the field of view is due to "secondary reflection". Although "secondary reflection" cannot completely be diminished at the off-axis angle of $20'$, the center of the field of view is nearly free of stray light. The semi-circular bright region in the middle panel, starting at (DETX, DETY)=$(-8''9, +6''5)$, running through $\sim(0', 0')$, where the image becomes fainter, and ending up at $(-8'.9, -6'.5)$, originates from the innermost secondary reflector, because the space between the innermost reflector and the inner wall of the telescope housing is much larger than the reflector-reflector separation. This semi-circular bright region is only marginally visible in the real Crab nebula image in the right panel. Another remarkable difference between the simulation and the real observation is the location of the brightest area; in the simulation, the left end of the image (DETX $\lesssim -7'.5$, $|\mathrm{DETY}| \lesssim 3'$) is relatively dark whereas the corresponding part is brightest in the Crab nebula image. These differences originate from relative alignments among the primary and secondary reflectors, and the blades of the pre-collimator, which are to be calibrated by referring to the data of the stray light observations in the near future.

Overall, in-flight stray light observations of the Crab were carried out with off-axis angles of $20'$ (4 pointings), $50'$ (4 pointing) and $120'$ (4 pointing) in 2005 autumn. Follow-up observations covering more offset angles of $50'$ (4 pointing) , $65'$ (8 pointing) were made in 2010 autumn. Examples of mozaic images made with the offset observations in SKY coordinate are shown in Figures 6.15 and 6.16. The stray images differ from offset to offset and from azimuth to azimuth in the XRT coordinate. It also strongly depends on energy.

Figure 6.17 shows the measured and simulated angular responses of the XRT-I at 1.5 and 4.5 keV up to 2°. The effective area is normalized to 1 at the on-axis position. The integration area corresponds to the detector size of the XIS ($17'.8 \times 17'.8$). The plots are necessary to plan observations of diffuse sources or faint emissions near bright sources, such as outskirts of cluster of galaxies, diffuse objects in the Galactic plane, SN 1987A, etc.. The four solid lines in the plots correspond to raytracing simulations for the different detectors, while the crosses are the normalized effective area using the Crab pointings. For example, the effective area of the stray light at 1.5 keV is $\sim 10^{-3}$ at off-axis angles smaller than $70'$ and $< 10^{-3}$ at off-axis angles larger than $70'$. The measured stray light flux is in agreement with that of the simulations to within an order of magnitude. The solution of the solid lines is incorporated into the `xissim` and the `xissimarfgen` tools using CALDB 2008-06-02.

For feasibility studies of XIS data analyses of faint objects near bright sources, proposers are encouraged to simulate observations using `xissim` in order to determine whether the stray light flux might dominate that of the faint object or not. Proposers who do observe a target heavily suffering from stray light contamination need to handle the data with special care regarding calibration errors. Faint objects in the Galactic center and plane often suffer from stray light contamination from bright X-ray stars, and the flux of the outskirts of galaxy clusters, widely extended over the detector field of view, is sometimes dominated by stray light from the bright core.

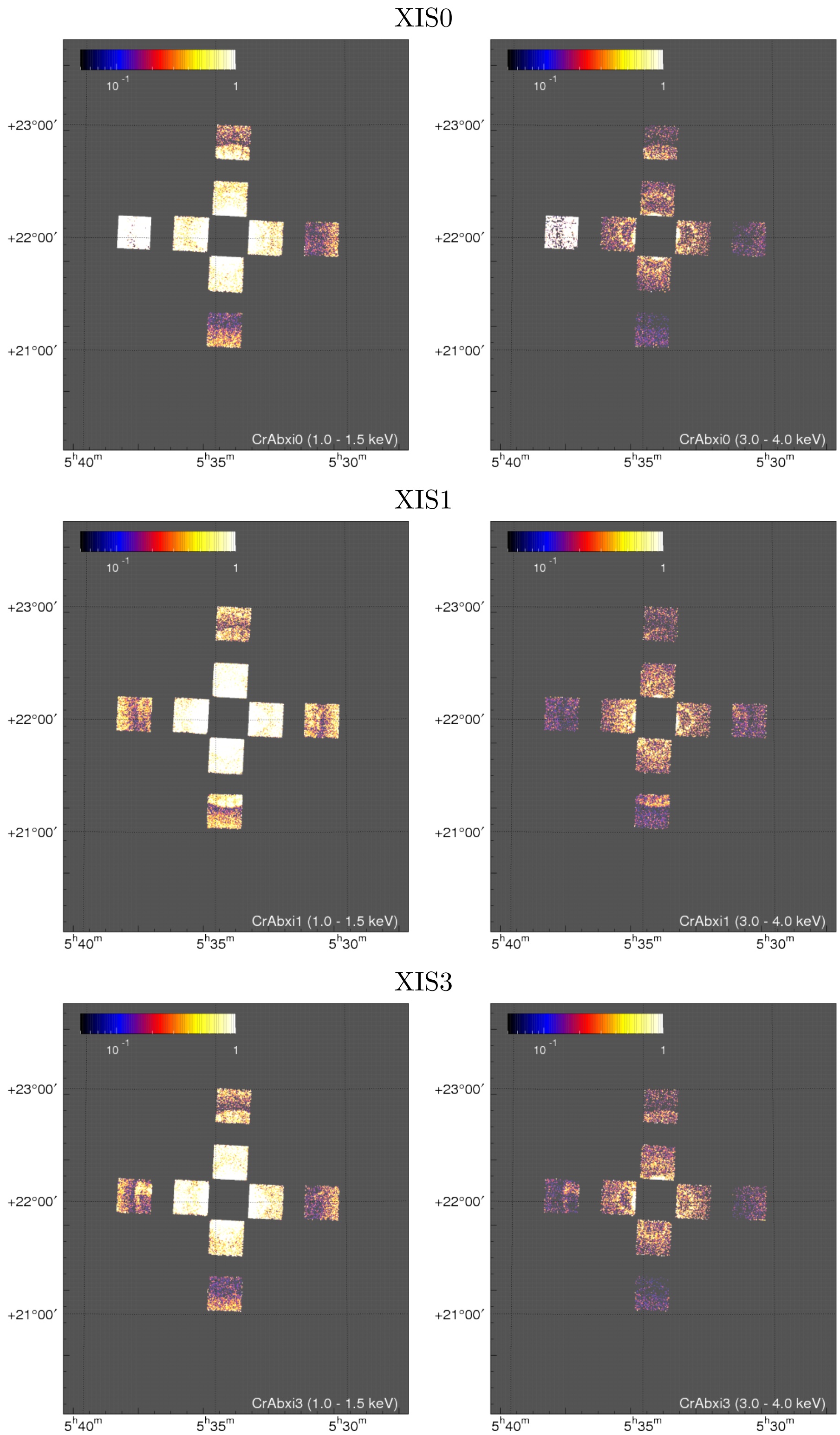

Figure 6.15: Mosaic images of offset observations of the Crab taken in 2005.

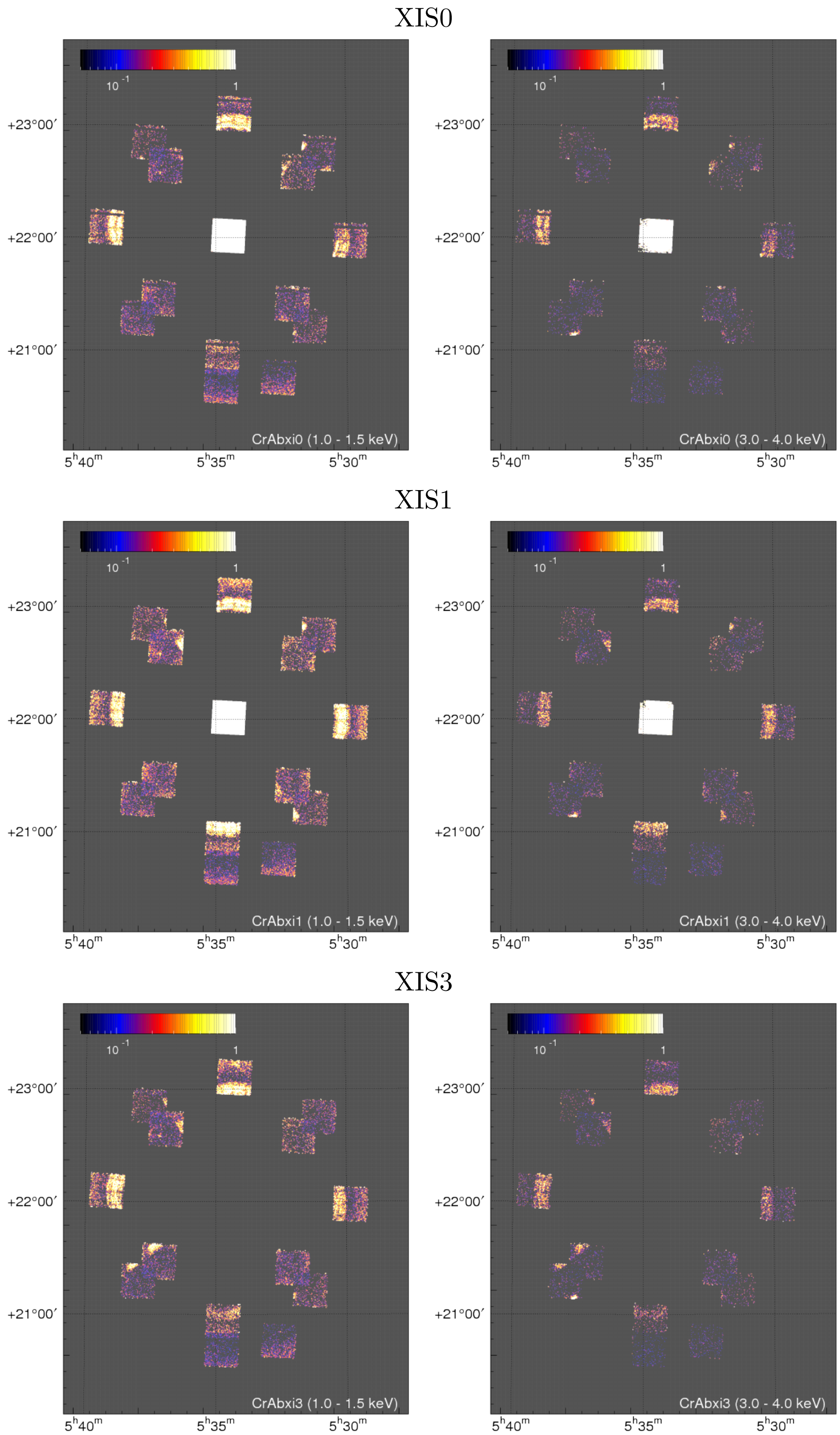

Figure 6.16: Same as figure 6.15, but taken in 2010.

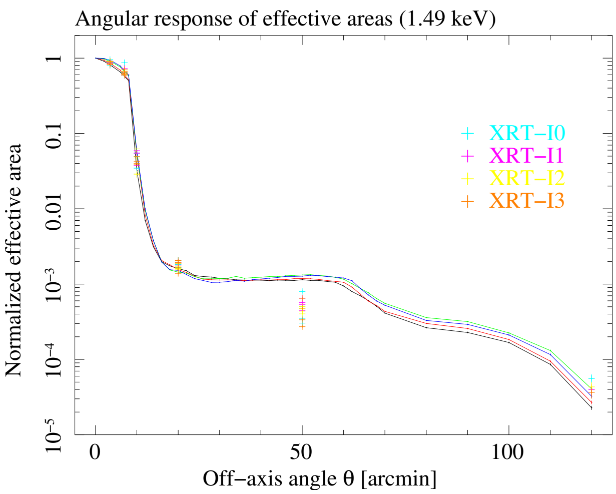

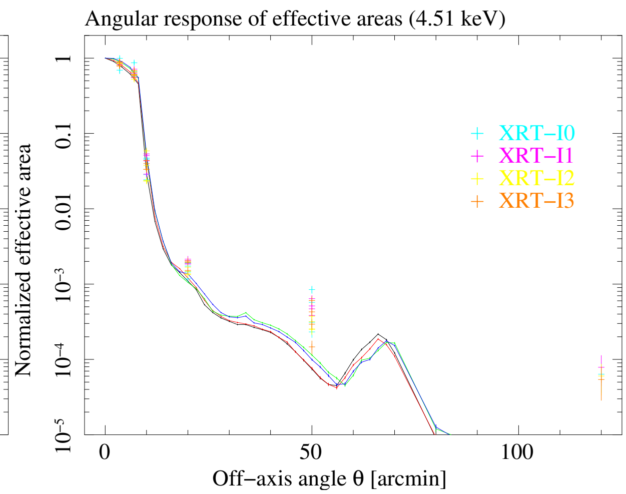

Figure 6.17: Angular responses of the XRT-I at 1.5 (left) and 4.5 keV (right) up to 2°. The effective area is normalized to 1 at the on-axis position. The integration area is corresponding to the detector size of the XISs ($17'.8 \times 17'.8$). The four solid lines in the plots correspond to different detector IDs. The crosses are the normalized effective area using the Crab pointings.

Observers can avoid contamination from stray light if they choose the roll and offset angles properly. Fig. 6.18 shows a schematic diagram of the stray light patterns for a stray light source at an azimuth angle of α and an offset angle of R. The square in Fig. 6.18 corresponds to the XIS field of view. The nominal position is located within 1 arcmin from the optical axis of the XIS system within a couple of arcmins. The XIS field of view near to and far from a stray light source is contaminated by stray light of the "Secondary-reflection component" and the "Backside component", respectively (Mori et al. 2005, PASJ 57, 245). On the other hand the near and far sides are free from the "Backside component" and the "Secondary-reflection component", respectively. There is another stray light free region corresponding to the "Quadrant Boundary" with a cone angle of 12.8 deg at an azimuth angle of 45 deg with 90 deg pitch. Observers can thus choose between three kinds of the "stray light free" regions. Fig. 6.19 shows pointing positions targeting these three kinds of stray light free regions, marked in white: the "Quadrant Boundary" region (top), the " Secondary-reflection component free" region (middle) and the "Backside component free" region (bottom).

1. Quadrant Boundary:
   If an azimuth angle of 45, 135, 225, or 315 deg is possible, the target at the XIS nominal position will fall into the stray light free region of the Quadrant Boundary. The integrated radius r which is free from stray light can be expected to be $\sim 6.8\frac{R}{1\mathrm{deg}}$ arcmin. The radius has an uncertainty of a couple of arcmins due to the misalignments between the optical axis and the nominal position.

2. Secondary-reflection component free region:
   The Backside component is important in the energy band below 1.5 keV. It arises from scattering at the aluminum surface of the backside of the primary reflector. Therefore, if the stray light source is heavily absorbed below 1.5 keV or the interesting energy band of the target is limited to above 1.5 keV, it is recommended to locate the target in the secondary-reflection component free region. The recommended pointing position offset in this case is:

   Δ DET-X $= -(r+2)\sin\alpha$ [arcmin]
   Δ DET-Y $= -(r+2)\cos\alpha$ [arcmin].

   Note that the offset direction is towards the near side of the stray light source. The margin of 2 arcmin corresponds to the misalignment between the optical axis and the nominal position. The Backside component appears within an offset angle R of up to $\sim 1.3(\frac{E}{1.5\,\mathrm{keV}})^{-1}$ deg (E <1.5 keV). If the stray light source is located further away than the critical offset angle, observers can choose the Secondary-reflection component free region, as well.

3. Backside component free region:
   The secondary-reflection component focusses at the middle of the detector only for offset angles of 40–75 arcmin at any energy. Therefore, if the stray source is located

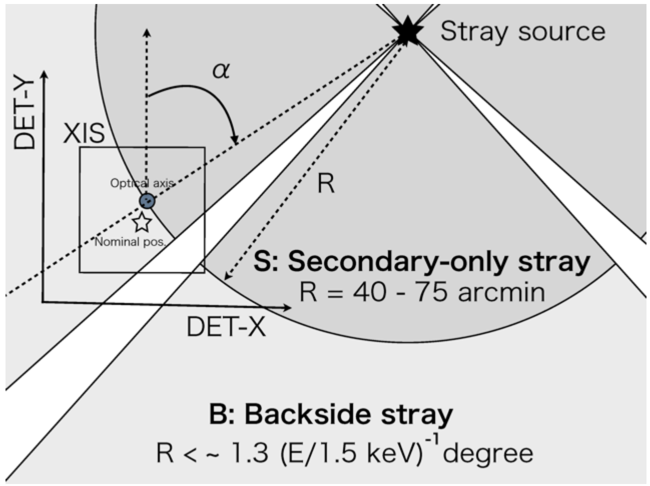

Figure 6.18: Stray patterns for a stray source at an azimuth angle of α and an offset angle of R.

within 40 arcmin or further away than 75 arcmin, it is recommended to located the target in the backside component free region. The recommended pointing position offset in this case is:

Δ DET-X $= +(r + 2)\ \sin\alpha$ [arcmin]
Δ DET-Y $= +(r + 2)\ \cos\alpha$ [arcmin].

The offset direction is towards the far side of the stray light source.

If observers cannot choose any of the three stray light free regions, the possibility of contamination through stray light exists.

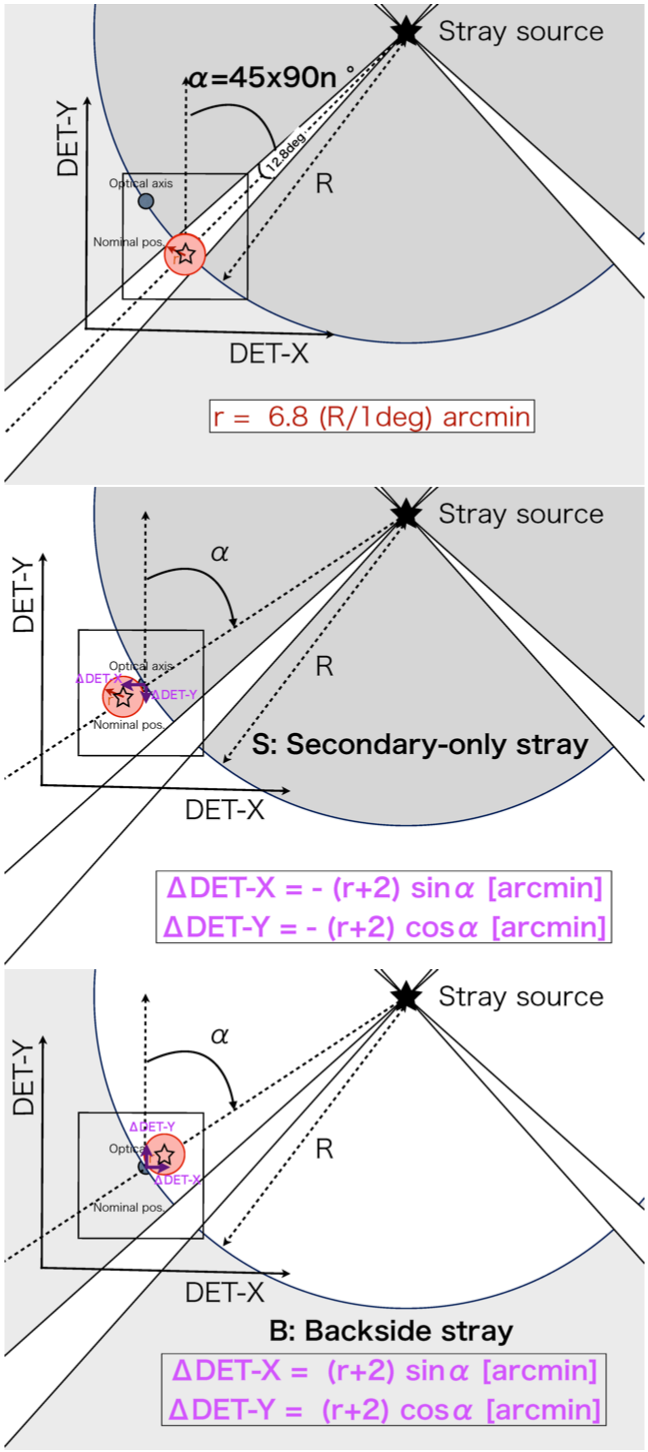

Figure 6.19: Pointing positions targeting the three kinds of stray light free regions: the "Quadrant Boundary" region (top), the "Secondary-reflection component free" region (middle) and the "Backside component free" region (bottom).

Chapter 7

X-Ray Imaging Spectrometer (XIS)

7.1 XIS Overview

7.1.1 XIS Basics

The X-ray Imaging Spectrometer (XIS, Koyama et al., 2007) celebrated its first light on 2006, August 11, about a month after the launch of *Suzaku*. The instrument has been operated successfully since then, producing many scientific results. The entire instrument has a weight of 48.7 kg and consumes 67 W at a bus voltage of 50 V during normal operations. The XIS is composed of four units of Si-based X-ray charge coupled device (CCD) cameras (Fig. 7.1). In these X-ray sensors, incident X-ray photons are converted into a number of electron-hole pairs via photoelectric absorption and subsequent ionization by photoelectrons and their secondaries. The energy of the incident photon can be measured since it is proportional to the amount of charge produced.

Each XIS unit is located at the focal plane of one of four independent, identical, and co-aligned X-Ray Telescope modules (XRT, Serlemitsos et al., 2007), which are called XRT-I0, XRT-I1, XRT-I2, and XRT-I3. The XIS is operated in photon-counting mode, in which each X-ray event is discriminated from the others and its position, energy, and arrival time are reconstructed. This gives the XIS imaging-spectroscopic capabilities in the 0.2–12.0 keV energy band over an $18' \times 18'$ region.

Similar instruments The XIS is similar to its predecessor, the Solid-state Imaging Spectrometer (SIS) onboard the ASCA satellite, in its working principle. Many improvements were made based on successful use of the SIS over eight years. It is also similar to its brothers: *Chandra* ACIS (Garmire et al., 2003), *XMM-Newton* EPIC (Turner et al.,

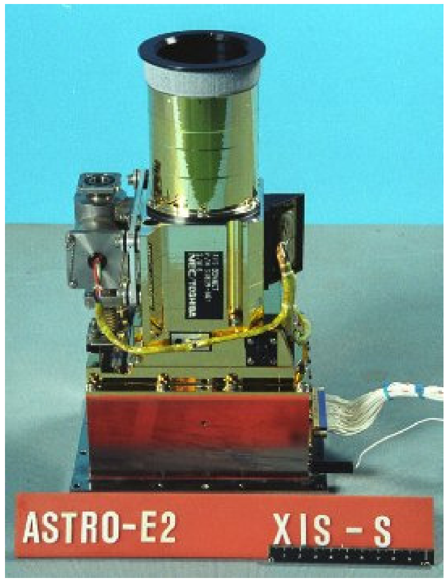

Figure 7.1: A photo of one of the four XIS sensors before installation on the satellite.

2001; Strüder et al., 2001), and *Swift* XRT (Burrows et al., 2004).

X-ray CCD instruments, including the XIS, are characterized by their flexibility in operation and possible rapid performance changes on orbit. In particular, micro-meteorite hits can leave unrecoverable damage to a part of the instrument. The entire imaging area of the XIS2 was lost in 2005 November and a part of the XIS0 in 2009 June.

Merits The XIS has several advantages over other instruments.

- The XIS is suited to investigate extended emission of low surface brightness for the following reasons:
  - It has a low and stable background environment through a combination of the low Earth orbit of the satellite and the instrument design.
  - It has a large effective area, which is comparable to the EPIC in the Fe K band.
  - The energy resolution and gain are well calibrated over the entire chip.
- The XIS is more tolerant regarding pile-up when observing bright sources for the following reasons:
  - The PSF of the XIS is much larger than those of ACIS and EPIC while the plate scale is comparable. This means a heavy oversampling of the PSF.
  - It has a wide range clocking mode options provided as user options.
- Together with the HXD, simultaneous wide-band spectral coverage is available.

Responsible parties The XIS was developed and has been maintained jointly by Japan and the United States, with participating organizations including the MIT, ISAS, Kyoto University, Osaka University, Rikkyo University, Ehime University, Miyazaki University, Kogakuin University, Nagoya University, Aoyama Gakuin University, and major participating contractors including the Mitsubishi Heavy Industries (MHI), the NEC-Toshiba Space Systems, and the System Engineering Consultation (SEC) Co. Ltd.

7.1.2 XIS Components

7.1.2.1 Sensors

Dimensions Each CCD camera has a single CCD chip, which consists of the imaging area and the frame store area. The imaging area is exposed to the sky for observations, while the frame store area is shielded. Each chip is composed of four segments called segment A, B, C, and D. Each segment has its own readout node (Fig. 7.3).

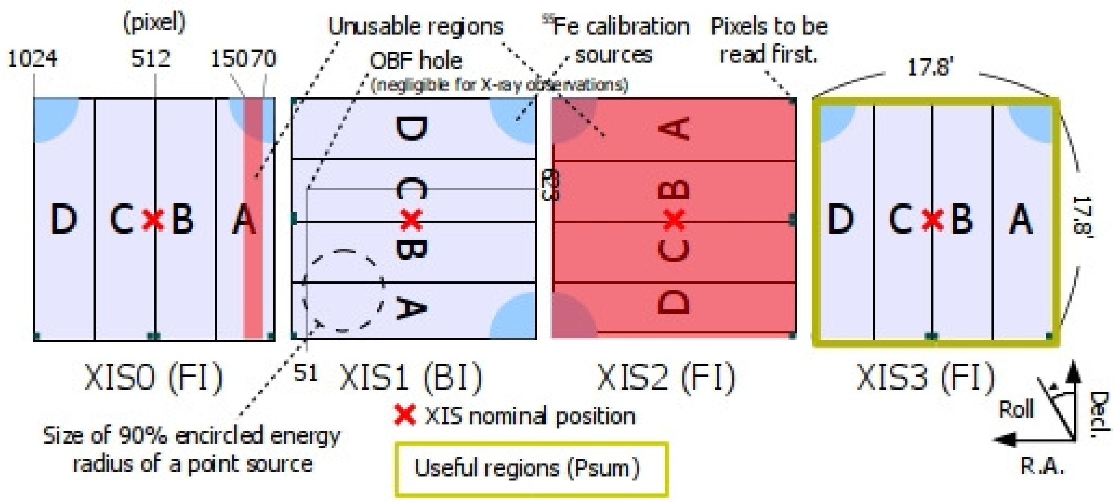

Figure 7.2: Field of view of the XIS. All sensors are co-aligned.

The imaging area has a pixel size of 1024×1024 pixels. The pixel scale is 24 μm pixel^{-1} and the physical size is 25 mm squared. The plate scale is 1.04$''$ pixel^{-1} and the total sky coverage is 18$'$ squared.

CCD types The XIS1 is a back-side illuminated (BI) chip. The other three sensors (XIS0, 2, and 3) are front-side illuminated (FI) chips. The BI and FI chips are superior to each other in the soft and hard band responses, respectively.

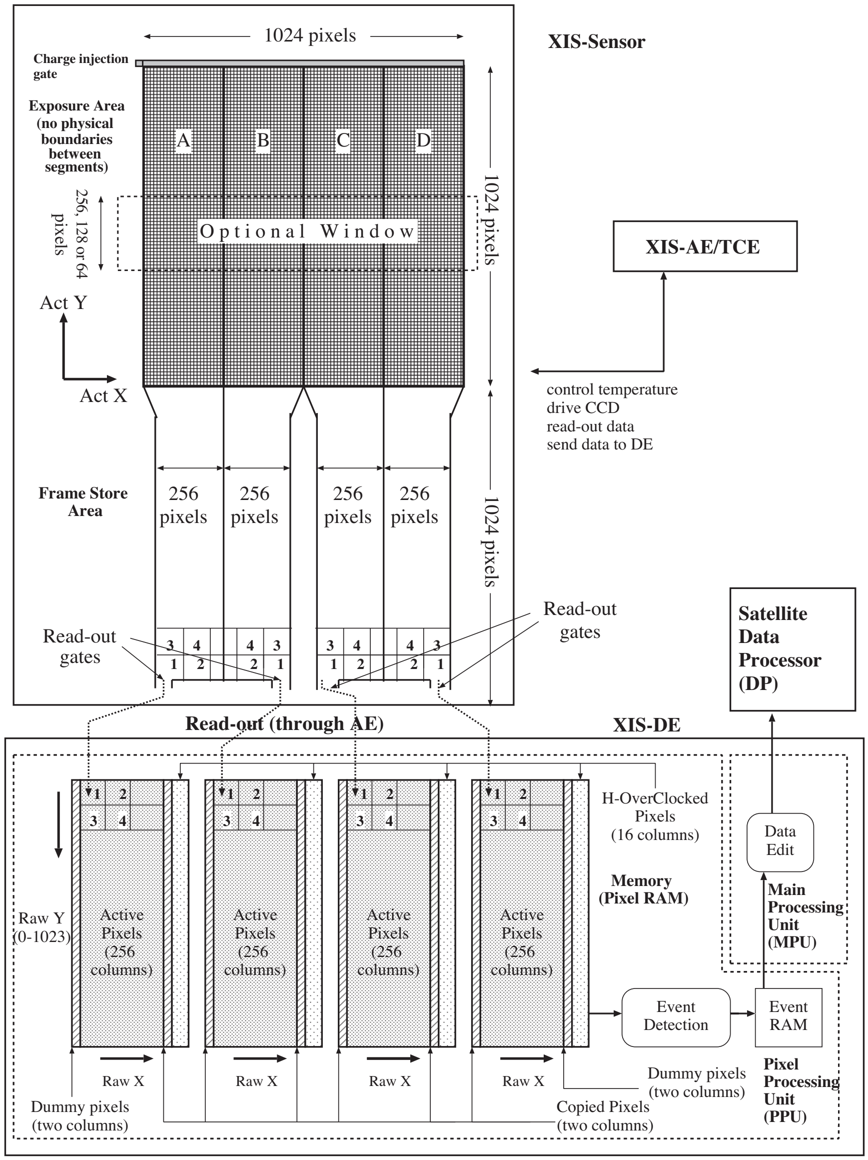

Figure 7.3: Schematic view of the data flow in one XIS unit.

Optical blocking filter (OBF) X-ray CCDs are also sensitive to optical and UV photons. To suppress such signals, an optical blocking filter (OBF) is installed on the surface of the CCDs. The OBF is made of polyimide with a thickness of 1000 Å, which is coated with a total of 1200 Å of Al (400 Å on one side and 800 Å on the other).

Calibration sources For in-flight calibration, three ^{55}Fe calibration sources with a half life of 2.73 years are installed in each XIS unit. The ^{55}Fe sources emit strong Mn Kα and Kβ lines at 5.9 keV and 6.5 keV, respectively. Two sources illuminate corners of the segments A and D of the imaging area at the far side of the readout node. The other one is installed in the door. It was used to illuminate the entire chip before opening the door for the final check before launch and the initial check after launch. Because the door was opened for observations, the door calibration sources are not used any longer. Scattered X-rays from the door calibration sources may appear in the entire imaging area.

7.1.2.2 Cooling System

To reduce the dark current, the sensors are kept at $\sim -90°$C all the time. Thermo-electric coolers (TECs) using the Peltier effect are used for cooling, which are controlled by the TEC Control Electronics (TCE).

7.1.2.3 Electronics

Analogue electronics The analog electronics (AE) system drives the CCD by providing driving clocks for exposure and charge transfer, sampling the voltage, amplifying the data, and converting to the digital values. The XIS has two identical units of the AE and the TCE (see 7.1.2.2, Cooling system control), which are stored in the same housing for each unit. One unit (AE/TCE01) is used for XIS0 and XIS1, while the other (AE/TCE23) is used for XIS2 and XIS3.

Digital electronics The digital electronics (DE) system processes the digitized data. The DE has two pixel processing units (PPU01 and PPU23) and a main processing unit (MPU). The digital data from the AE are stored in the Pixel RAM of the PPUs; PPU01 for data taken with AE/TEC01 and PPU23 for AE/TEC23. The PPUs access the raw CCD data in the Pixel RAM, carry out event detection, and send event data to the MPU. The MPU edits the telemetry packets and sends them to the satellite's main digital processor.

7.1.3 CCD Pixels & Coordinates

RAW XY coordinates Pixel data collected in each segment are read out from the corresponding readout node and sent to the Pixel RAM. In the Pixel RAM, pixels are given RAW X and RAW Y coordinates for each segment in the order of the readout, such that RAW X values are from 0 to 255 and RAW Y values are from 0 to 1023. These pixels in the Pixel RAM are named *active pixels*. In the same segment, pixels closer to the read-out node are read out earlier and stored in the Pixel RAM earlier. Hence, the order of the pixel read-out is the same for segments A and C, and for segments B and D, but different between these two segment pairs, because of the different locations of the readout nodes. In Fig. 7.3, numbers 1, 2, 3 and 4 marked on each segment and the Pixel RAM indicate the order of the pixel read-out and the storage in the Pixel RAM. In addition to the active pixels, the Pixel RAM stores *copied pixels*, *dummy pixels* and *H-over-clocked pixels* (Fig. 7.3). At the borders between two segments, two columns of pixels are copied from each segment to the other. Thus these are named copied pixels. Two columns of empty dummy pixels are attached to the segments A and D. In addition, 16 columns of H-over-clocked pixels are attached to each segment.

ACT XY coordinates Actual pixel locations on the chip are calculated from the RAW XY coordinates and the segment ID during ground processing. The coordinates describing the actual pixel location on the chip are named ACT X and ACT Y coordinates (Fig. 7.3). It is important to note that the RAW XY to ACT XY conversion depends on the on-board data processing mode.

7.1.4 Major Events

The detector performance changes both continuously and discontinuously over time. This is especially the case for CCD instruments. Users need to take the latest information into account in order to make the best use of the instrument. Some major changes and their causes are:

- Continuous degradation of the gain and energy resolution by increasing charge transfer inefficiency due to radiation damage.
- Continuous degradation of low-energy efficiency due to accumulating contaminating material on the optical blocking filter.
- Discontinuous change of the non X-ray background due to solar flares.
- Discontinuous change of the gain and energy resolution by applying the charge injection operation with changing settings.
- Discontinuous loss of a part of the detector performance due to micro-meteorite hits.
- Discontinuous change of the detector performance due to policy changes with respect to operations in order to keep up with the changes above and others.

Table 7.1 shows major events since the start of the mission in chronological order. The XIS log at `http://www.astro.isas.jaxa.jp/suzaku/log/xis/` gives a complete list of events relevant for data reduction.

Table 7.1: Operation history

Date	Sensor	Description
2005-08-11	All	First light with 1E0102.2–7219
2006-01-18	All	Onboard software update to remove grade 7 events onboard.
2006-02-17	XIS023	Event threshold was changed to 100.
2006-10	All	SCI operation started.
2006-11-09	XIS2	A micro-meteorite hit. The entire imaging area became dysfunctional.
2008-01-30	All	MPU0 is lost and replaced with MPU2.
2009-06-23	XIS0	A micro-meteorite hit. A 1/8 of the imaging area became dysfunctional.
2009-04-01	All	P-sum clocking mode officially supported.
2009-11-02	All	MPU1 reset after a ROM update.
2009-12-18	XIS1	A micro-meteorite hit. No major impact in scientific capability.
2009-04-01	All	SCI off operation support terminated.
2010-04-01	All	Edit mode selection automated.
2011-03-09	All	XIS halted due to non-maskable interruption and was restarted.
2011-06-01	XIS1	Injection charge increased to 6 keV for Normal (no option).
2011-08-22	XIS1	Injection charge increased to 6 keV for Normal (1/4 win).
2011-09-01	XIS1	Injection charge increased to 6 keV for Normal (0.1s burst).
2011-09-29	All	The default PPU ratio changed to the optimum for each editing mode combination.
2011-10-06	XIS1	Injection charge increased to 6 keV for Normal (1/4 win+1.0s burst, 1/8 win).
2011-10-11	XIS1	Injection charge increased to 6 keV for Normal (1/4 win+0.1s, 0.3s, & 0.5s burst).
2011-10-25	XIS1	Injection charge increased to 6 keV for Normal (0.5s, & 0.62s burst).
2011-10-25	XIS1	Support for XIS1 2.0s burst with CI=6 keV terminated.
2012-01-26	All	XIS restarted after the satellite UVC. TEC2 power terminated to save power.
2012-04-01	All	Choice of using the HXD nominal position was removed.
2012-07-11	All	XIS stopped during the satellite ejection of RCS hydrazine,
2012-07-14	XIS2	TEC2 for the XIS2 was terminated permanently for saving power.

7.2 XIS Observation Planning

7.2.1 User Options

Available options The XIS has numerous instrumental settings, which are fine-tuned to serve a wide range of observational purposes. A few of them are left as user options. Different options can be used for different sensors.

1. Clocking mode
2. Editing mode
3. PPU ratio
4. Lower event threshold
5. Area discrimination

In many cases, the default settings are adequate. If this is not the case, the appropriate choice of clocking mode options is generally enough and there is little need to change the other options. The choice between the XIS and HXD nominal positions is no longer available: all observations are made at the XIS nominal position (the center of the XIS field of view) unless otherwise requested.

Observations requiring non-default settings Users need to consider an appropriate choice of clocking mode options when they are planning observations of bright (>10 mCrab in 0.5–10 keV) sources or those requiring a higher temporal resolution than 8 s.

Declaration of the use of non-default setting Use of non-default options should be stated clearly in the technical justification of the proposal document. The choice of clocking mode needs to be specified in the cover page. These choices can be tentative. For successful proposals, an inquiry is sent to the PI about three weeks prior to the observation. The choice of user options can be revised at this time.

Last-minute changes The behavior of very bright sources is often unpredictable. The XIS operation team waits until the last minute before finalizing the options, if necessary. The deadline is 10:00 JST (1:00 in UT) every weekday and Saturday, at which the operation team starts generating the command sequence. Users need to submit the final choice of options by this deadline 1–3 days before the start of their observation. Prior consultation with the XIS operation team is necessary for their availability and the exact deadline.

Consultation The appropriate choice of options is the responsibility of the observer. A summary is provided by the XIS quick reference at:

`http://www.astro.isas.jaxa.jp/~tsujimot/pg_xis.pdf`
The XIS operation team can be consulted at:
`xisope@astro.iasa.jaxa.jp`
The team will make the best use of the operational flexibility to maximize the scientific output of the observations.

7.2.1.1 Clocking Modes

The clocking mode specifies how the CCD pixels are read out. Each clocking mode has its own μ-code, a pattern of voltage clocking for exposure and charge transfer. It enables full read, partial read, or stacked read (Table 7.2). With a partial or stacked read, a higher pile-up limit and timing resolution can be achieved at a sacrifice of observing efficiency and imaging information.

Table 7.2: Clocking modes

Clocking mode	Options	Readout	Area (pixels)	t_{exp} frame^{-1} [a] (s)	Obs eff. [b]
Normal	none	full	1024×1024	8	1.0
	$1/w$ win	partial in space	$1024/w\times1024$	$8/w$	1.0
	b s bst	partial in time	1024×1024	b	$b/8$
	$1/w$ win+b s bst	partial n space & time	$1024/w\times1024$	b	$wb/8$
P-sum	—	stacked	1×1024	—	1.0

[a] Effective exposure time per frame.
[b] Observing efficiency, not including events falling outside of a window for the window options.

There are two major types of clocking mode: the Normal mode and the P-sum mode. The **Normal mode** is for timed-exposure readout. It can be combined with a window option (partial readout in space), burst option (partial readout in time), or both (partial readout in both space and time). Fig. 7.4 shows the time sequence of exposure, frame-store transfer, readout, and storage to the Pixel RAM (in the PPU) for the Normal clocking mode. The **P-sum mode** is for stacked readout. The P-sum clocking mode is in principle available for all FI sensors. However, because it is severly affected by leaked charge in areas damaged by micrometerorite hits, the P-sum clocking support was terminated for the XIS2 and XIS0. Therefore, it is currently available only for the XIS3. Observers using the P-sum clocking mode for the XIS3 need to use a Normal clocking mode for the other sensors.

Normal clocking mode

1. No option: full readout of all pixels with a frame time of 8 s.
2. Window option: partial readout in space. In the $1/w$ window mode, the central $1024/w$ pixels are read out in the Y direction and the entire pixels are read out in

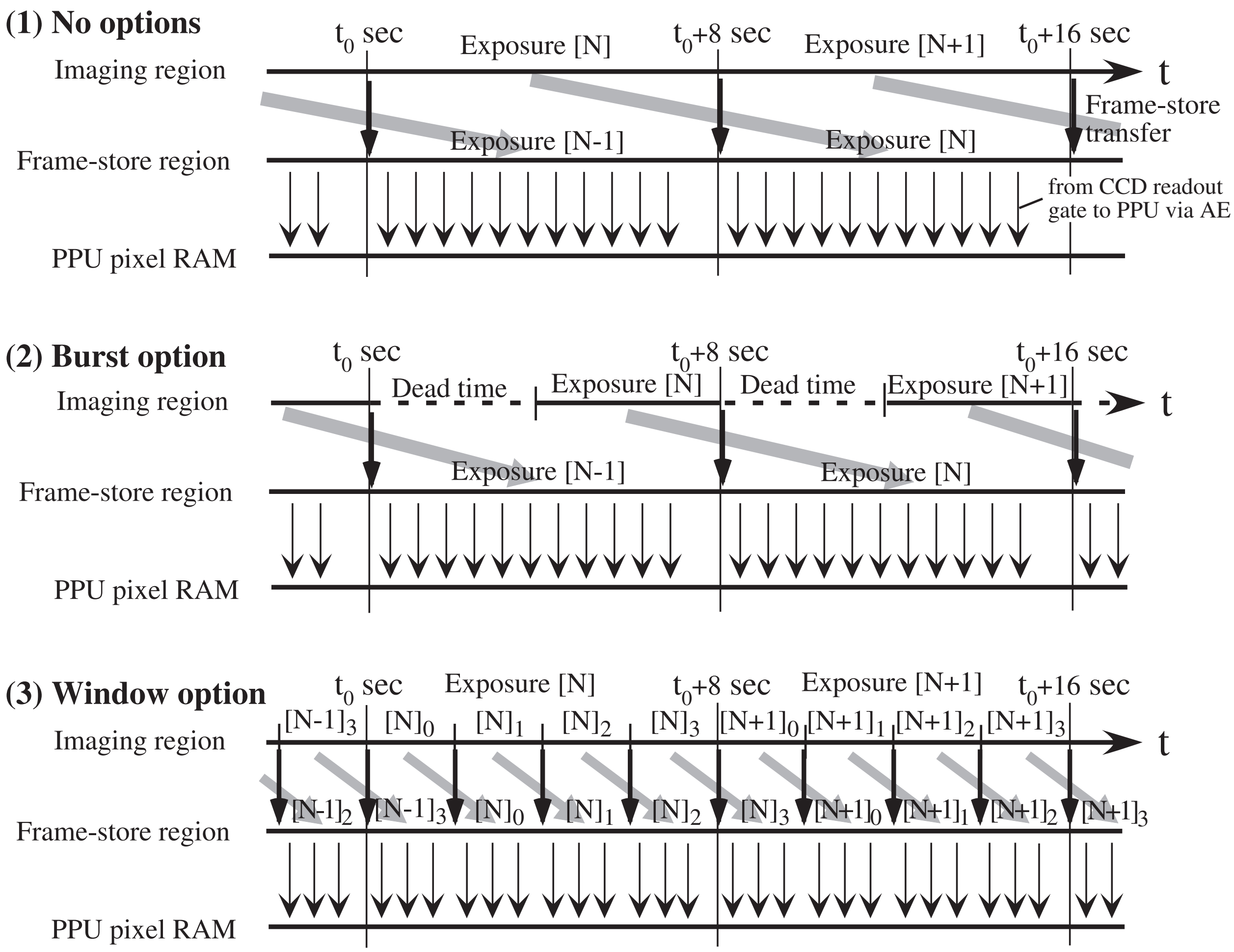

Figure 7.4: Time sequence of the exposure, transfer, and readout. For the window option, 1/4 window is assumed.

the X direction, yielding a $1024 \times 1024/w$ pixel image. The exposure time is $8/w$ s.

3. Burst option: partial readout in time. In the b s burst mode, all pixels are read out, but the effective exposure time is limited to b s (b <8 s). During 8 s of exposure time, events detected in the first $(8 - b)$ s are transfered and discarded without being recorded. Events detected in the remaining b s are transfered and recoreded.
4. Window+burst option: partial readout in both time and space. In $1/w$ window and b s burst mode, the central $1024 \times 1024/w$ pixel image is read out with an exposure time of $8/w$ s. During the exposure time, events in the first $(8/w - b)$ s are discarded and those in the last b s are recoreded. The inequity of $8/w > b$ always holds.

The available window and burst options are summarized in Table 7.3.

Table 7.3: Window and burst options (XIS nominal position)

Option	none	win		burst				win+burst				
Window	1/1	1/4	1/8	1/1	1/1	1/1	1/1	1/4	1/4	1/4	1/4	1/8
Burst (s)[a]	8.0	8.0	8.0	2.0	0.62	0.5	0.1	1.0	0.5	0.3	0.1	0.5
XIS0	x	x	x	x			x	x	x	x	x	x
XIS1	x	x	x		x	x	x	x	x	x	x	x
XIS3	x	x	x	x			x	x	x	x	x	x
Pile-up limit (s^{-1})	12	48	96	48	155	192	960	96	192	320	960	192
Obs efficiency[b]	1.0	1.0	1.0	0.25	0.08	0.06	0.01	0.5	0.25	0.15	0.05	0.5

[a] The approximate burst time. The exact time may be different; e.g., 0.297 s for 0.3 s burst due to restrictions in the design of the clock pattern.

[b] The observing efficiency. This does not include the loss of events outside of the window in the window and window+burst options. This does not include the loss of effective exposure time by charge transfer of 156 ms.

Some advice in selecting window and burst options

- The observing efficiency is always smaller than 1 for window, burst, or both options due to their partial readout nature. The efficiency can be very small.
- In the window mode, a part of the events falls outside of the window. With a half-power diameter of $2'$ and the telescope wobbling of $\sim 0.5'$, this is not negligible especially for $w = 8$ with $2.2'$ for the window height and for the XIS1 with the wobbling direction perpendicular to the window. The telescope wobbling is synchronous to the rotation period of the satellite of ∼96 min, which gives an artificial fluctuation in the count rate with this frequency.
- The window mode does not include the ^{55}Fe calibration sources at the top corners, so self-calibration of gain and energy resolution using the calibration sources cannot be used.
- The observing efficiency is always larger for the $1/w$ and b s burst mode over the b s burst mode.
- In short burst modes, out-of-time events are non-negligible.
- It is always helpful to retrieve archive data taken in the same clocking mode as a planned observation to evaluate its properties. The *Suzaku* XIS log at `http://darts.isas.jaxa.jp/astro/suzaku/suzakuxislog/top.do` can be used to find an appropriate observation.

P-sum clocking mode The pulse height from 128 rows are stacked into a single row along the Y direction. Charge is transferred continuously, thus the spatial information along the Y direction is lost and replaced with the arrival time information. The arrival time is ticked at a 7.8 ms resolution. This is smeared by the point spread function with a HPD of $2'$, which is equivalent to 0.9 s.

7.2.1.2 Editing Modes

The editing mode specifies the telemetry format of the events. The XIS has several editing modes (Table 7.4). Four of them are for observational purposes, the remaining ones are for diagnostic purposes.

Table 7.4: Editing modes and size per event for observation modes

Purpose	Clocking mode	Editing mode	Event size (byte)[a]		
			min	max	mean
Observations	Normal	5×5	28	52	40
		3×3	15	23	19
		2×2	8	11	9
	P-sum	timing	4	4	4
Diagnostics	Normal/P-sum	frame			
		dark frame			

[a] Data are compressed onboard, The compression rate varies depending on the grade.

Editing modes for observations For Normal clocking modes three editing modes (5×5, 3×3, and 2×2) are available. The 2×2 mode is used only for the FI sensors. For P-sum clocking mode, the editing mode is fixed to the timing mode. Each editing mode has a different telemetry format, which includes the x and y position and the pulse height (PH) of the event (Fig. 7.5). Different editing modes have different sizes per event (Table 7.4).If the dark-subtracted PH value is above the split threshold in the neighboring pixels, they are considered to be a part of the charges generated by the event and thus are summed in the event reconstruction. Different thresholds are applied for the immediately neighboring pixels (inner split threshold) and those around them (outer split threshold).

1. 5×5 mode: The PH values of each 5×5=25 pixel around the event center are sent to the telemetry.
2. 3×3 mode: The PH values of each 3×3=9 pixel around the event center and the 1-bit information (whether the PH is larger than the outer split threshold or not) for the surrounding 16 pixels are sent to the telemetry.
3. 2×2 mode: The PH values of each 2×2=4 pixel around the event center and the 1-bit information (whether the PH is larger than the outer split threshold or not) for the attached 8 pixels are sent to the telemetry. The 2×2 pixels are selected such that they include the pixels with the highest, the second highest, the third highest (,and the fourth highest) PH values.
4. Timing mode: The summed PH value of the 1×3 pixels around the event center and the event grade are sent to the telemetry. The PH is summed if the neighboring pixels have a PH value above the inner split threshold.

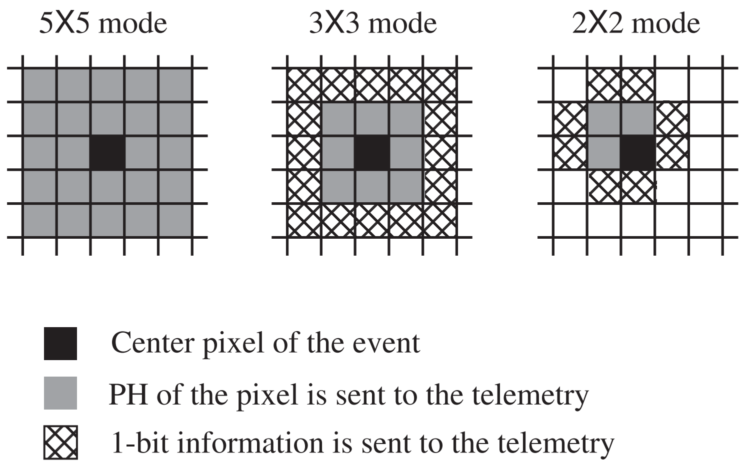

Figure 7.5: Data pattern for 5×5, 3×3, and 2×2 editing modes. 1-bit information indicates whether the pulse height of the pixel exceeds the outer split threshold.

Although the amount of information for event reconstruction is different among the 5×5, 3×3, and 2×2 modes, no significant difference has been found so far between the former two modes. Only a small difference is seen for the 2×2 mode for its lack of ability to perform trail correction (§ 7.3.2.4). The 2×2 mode and the timing mode are not available for the XIS1 because the trailing correction does not work properly for the former mode and the amount of flickering pixel is larger than for the other sensors for the latter mode.

Editing mode combinations Technically speaking, arbitrary combinations of editing modes for the four sensors are possible. However, for reasons of operational reliability, combinations are restricted to those listed in Table 7.5.

Editing modes for diagnastics The diagnositic modes are only for diagnostic purposes and not available to general users. The XIS is operated in these modes outside of observing times.

1. Frame mode: The pulse height data of all pixels are dumped.
2. Dark frame mode: The dark levels of all pixels are dumped. A dark frame is taken once every day during an SAA passage.

7.2.1.3 PPU Ratio

The PPU ratio controls the relative fractional telemetry allocation for the four sensors. The ratio is fixed to be the optimum value assuming the use of the Normal clocking mode with the same options for all the sensors (5x5, 3x3, or f2x2_b3x3 combination) or the use of the P-sum clocking mode for XIS3 and the Normal clocking mode with the 1/4win + 0.5 s burst option for XIS0 and 1 (s3tim_s015x5, s3tim_s013x3, or s3tim_s02x2_s13x3 combination).

Table 7.5: Combination of editing modes and PPU ratio

Mode	5x5	3x3	f2x2_b3x3	s3tim_s015x5	s3tim_s013x3	s3tim_s02x2_s13x3
PPU ratio[a]	3:3:0:3 (CF)	3:3:0:3 (CF)	1:2:0:1 (49)	2:2:0:1 (4A)	3:3:0:3 (CF)	2:3:0:3 (CE)
XIS0	5x5	3x3	2x2	5x5	3x3	2x2
XIS1	5x5	3x3	3x3	5x5	3x3	3x3
XIS2	none	none	none	none	none	none
XIS3	5x5	3x3	2x2	timing	timing	timing

[a] The PPU ratio controls the relative fractional telemetry allocation for the four sensors. The fraction is an integer from 0 to 3. The hexagonal representation is with 8 bits = 2 bits × 4 sensors in the order of XIS0, 1, 2, 3 from the least significant bit, wherein the 2 bits are used for the PPU ratio value.

7.2.1.4 Lower Event Threshold

The lower event threshold defines the pulse height above which an event is recognized. It practically controls the lowest bandpass of the detector. The default event threshold is shown in Table 7.6. For XIS calibration observations, the FI event threshold is set to 50.

Table 7.6: Event threshold

Sensor	Event threshold (ADU)	(keV)
FI	100	0.365
BI	20	0.073

7.2.1.5 Area Discrimination

A part of the image can be masked with an area discrminator. Either the inside or the outside of a single rectangular region can be applied as a mask separately for each sensor. This is useful to supress telemetry of unwanted bright sources within the field of view of the target source. Currently, an area discrimination mask is applied permanently to the XIS0 to suppress leaked charge from the area damaged by a micrometeorite hit.

7.2.2 Systematic Observational Effects and their Mitigation

7.2.2.1 Photon Pile-Up

Description Photon pile-up is caused when multiple photons arrive at a detection cell within the frame time. If two photons with energies of E_1 and E_2 arrive, they are wrongly recognized as a single photon with an energy of E_1+E_2. This causes underestimation of the count rate, spectral hardening, PSF distortion, grade migration, and various other effects. Photon pile-up is a concern in observing point-like sources brighter than ∼10 mCrab. The degree of pile-up is measured by the pile-up fraction. Assume the mean count rate of photons landing in a pixel is $\lambda\,\mathrm{s}^{-1}\,\mathrm{pixel}^{-1}$. Then, the mean number of counts ($\overline{n}$) in a detection cell (A_{cell}) within the frame time (t_{frame}) is

$$\overline{n} = \lambda A_{\mathrm{cell}} \Delta t_{\mathrm{frane}}. \tag{7.1}$$

The number (n) fluctuates around $\overline{n}$ following Poisson statistics. The probability to have $n = k$ photons in a detection cell within the frame time is

$$P(n = k; \overline{n}) = \frac{\overline{n}^k e^{-\overline{n}}}{k!}. \tag{7.2}$$

The pile-up fraction (PF) is defined as the fraction of pile-up events among all incoming events as

$$\mathrm{PF}(\overline{n}) = \frac{\sum_{k=2}^{\infty} P(n = k; \overline{n})}{\sum_{k=1}^{\infty} P(n = k; \overline{n})} = \frac{1 - \sum_{k=0}^{1} P(n = k; \overline{n})}{1 - \sum_{k=0}^{0} P(n = k; \overline{n})} = 1 - \frac{\overline{n}}{e^{\overline{n}} - 1}. \tag{7.3}$$

Obviously, $\mathrm{PF}(\overline{n}) \to 0$ as $\overline{n} \to 0$ and $\mathrm{PF}(\overline{n}) \to 1$ as $\overline{n} \to \infty$.

λ is a function of the position in the PSF $f_{\mathrm{PSF}}(x, y)$ as

$$\lambda(x, y) = N_{\mathrm{total}} f_{\mathrm{PSF}}(x, y) \Delta x \Delta y \tag{7.4}$$

where $N_{\mathrm{total}}\ \mathrm{s}^{-1}$ is the total count rate of a source and $\Delta x \Delta y$ is the area of a pixel. $\lambda(x, y)$ is largest at the center $\lambda(x = 0, y = 0)$ and becomes smaller as the distance from the PSF center ($r = \sqrt{x^2 + y^2}$) increases in the outskirts.

Limits The pile-up limit is defined as the total count rate ($N_{\mathrm{pileup}}\,\mathrm{s}^{-1}$) at which the $\mathrm{PF}(\overline{n})$ at the center of the PSF exceeds 3%. In the XIS, this happens at roughly $12\,\mathrm{s}^{-1}$, or 10 mCrab. The limit should be regarded as an approximate value as the exact value depends on the spectral shape of the observed target. The tolerance also depends on scientific goals. For example, if the detection of a weak hard tail is the goal, the pile-up effect should be minimized. If the detection of a line is the goal, some degree of pile-up can be tolerated.

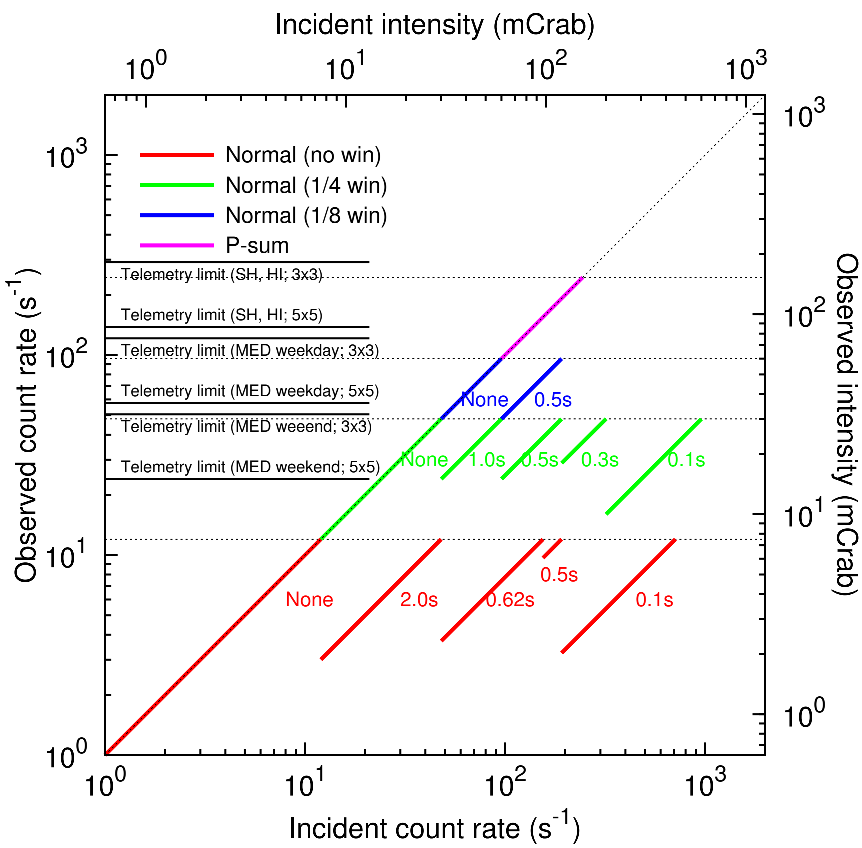

Figure 7.6: Incident versus observed count rates for a point-like source. The ratio of the two gives the observing efficiency. The thick lines indicate the range below the pile-up limit. Telemetry saturation is applicable only to Normal clocking modes.

Mitigation There are two major strategies to mitigate the effects of pile-up. They can be used together. One is to raise the pile-up limit by **using an option in the Normal clocking mode**. The pile-up limit for various options is summarized in Table 7.3 and shown in Fig. 7.6. The other is to only use events from the outskirts of the PSF, where the incoming rate per pixel is substantially smaller than in the center. This is called the **annulus extraction method** and is discussed in detail in Yamada et al. (2011). The tools are available at
`http://www-utheal.phys.s.u-tokyo.ac.jp/~yamada/soft/XISPileupDoc_20120221/XIS_PileupDoc_20120220.html`.
Table 7.7 gives the total incoming rate, at which some representative pile-up limit is hit at various radii in the PSF. In this approach, the fraction of grade 1 events is known to be a good indicator to assess the degree of pile-up. Note that the **attitude fluctuation of the satellite does not mitigate the photon pile-up** as its typical time scale is much

Table 7.7: Total count rate (s^{-1}) to cause the indicated pile-up fraction as a function of PSF radius.

Radius (pixel)	Pile-up fraction		
	3%	20%	50%
∼5	13.4	30.0	45.9
5∼10	17.6	43.3	67.7
10∼15	25.6	64.3	101
15∼20	33.8	85.4	134
20∼25	42.6	108	171
25∼30	55.8	142	224
30∼35	70.6	180	285
35∼40	88.2	226	356
40∼45	100	256	404
45∼50	119	304	480
50∼55	141	362	571

longer than the frame time of 8 s.

7.2.2.2 Telemetry Saturation

Description The XIS has a quota for the size of telemetry per unit time. The quota depends on the data rates (DR; SH=super high, HI=high, MED=medium, and LOW=low) and whether the observation is conducted on weekends or weekdays (Table 7.8). The satellite is also operated with a weekend allocation for a few days at the end and the beginning of the year. The operations team is responsible for deciding on the data rates depending on the observing conditions. The schedule is made to avoid bright sources to be observed on weekends, during which the telemetry allocation is small. Possible excess use of the quota is determined every 8 s during observations. Beyond the limit, a part of the telemetry is lost. Events in the segments B and C are prioritized over those in the segments A and D. Telemetry saturation occurs only when observing bright sources. Fortunately, in the XIS, the telemetry saturation is always avoided when users select an appropriate clocking mode to avoid pile-up. In practice, the following users need to consider the possibility of telemetry saturation seriously:

- Users planning to observe a very bright extended source.
- Users planning to observe a very bright point-like sources with a strategy of intentional pile-up for annulus extraction.

Table 7.8: Telemetry allocation for XIS

DR	Condition	Date	Rate (kbps)
SH	During contact		144
HI	Contact passes		144
MED	Remote passes	weekday	60
MED	Remote passes	weekend	25
LOW	Bad conditions[a]	weekday	15
LOW	Bad conditions[a]	weekend	1

[a] Bad conditions include SAA passages, low geomagnetic cut-off rigidity, etc.

Limits The telemetry saturation limit depends on the DR, choice of clocking modes, editing modes, and the PPU ratio. The resultant telemetry saturation limits are shown in Table 7.9 for the six editing mode combinations. A 10% margin for the headers and the background rates of $10\,s^{-1}$ (FI) and $20\,s^{-1}$ (BI) are included. The exact limit depends on the choice of clocking mode options. Users can use the XIS limit calculator at `http://www.astro.isas.jaxa.jp/~tsujimot/limits_xis.ods`.

Table 7.9: Incoming rate to cause telemetry saturation (s^{-1})

Edit mode	5x5	3x3	f2x2_b3x3	s3tim_s015x5	s3tim_s013x3	s3tim_s02x2_s13x3
SH	118.24	271.03	416.55	663.24	1163.81	1309.33
HI	118.24	271.03	416.55	663.24	1163.81	1309.33
MED (weekday)	37.6	101.26	161.89	276.17	484.74	545.37
MED (weekend)	4.00	30.53	55.79	114.89	201.79	227.06
LOW (weekday)	0.00	10.32	25.47	68.81	120.95	136.11
LOW (weekend)	0.00	0.00	0.00	0.00	0.00	0.80

[a] The lowest limit among the three operating sensors (XIS0, 1, 3) is given. A 10% margin for the headers and the background rates is included. The Normal clocking mode for the same options is assumed for 5x5, 3x3, and f2x2_b3x3, and the P-sum clocking mode (XIS3) and the Normal clocking mode with the 1/4win + 0.5 s burst option (XIS0 and 1) is assumed for s3tim_s015x5, s3tim_s013x3, and s3tim_s02x2_s13x3.

Mitigation The operations team is fully responsible for an appropriate choice of editing mode combinations among those in Table 7.5. The PPU ratio is optimized for a wide range of cases. Therefore, not much can be done by users in the observation planning stage to avoid telemetry saturation. In the data analysis step, however, users can remove time intervals afflicted by saturation by filtering the events using the distributed "non-saturated" good time interval files. The detailed procedure can be found in section 6.5.1 of the *Suzaku* Data Reduction Guide (ABC Guide).

7.2.2.3 Out-Of-Time Events

Description Out-of-time events are events recorded during charge transfer. They spread along the Y direction beyond the PSF with low surface brightness. For accurate photometry, users need to take out-of-time events into account. It is expected that they have the same spectrum as the on-source events. The effect is present for the Normal clocking mode with any option, but is different for those with and without burst option. For the Normal clocking mode without burst option, the out-of-time events spread uniformly along the Y direction at a surface brightness of 156 ms/(8–0.156) s=2.0% integrated over 1024 pixels. For the Normal clocking mode with a b s burst option, the out-of-time events spread uniformly in the upper and lower half of the image with different strengths (Fig. 7.7). This is because the clocking of the b s burst options consists of several steps: (1) exposure for $\sim$(8–b) s, (2) readout and flushing charges, (3) exposure for b s, (4) readout and recording. The flushing readout is performed without charge injection and takes 25 ms. The recording readout is with charge injection and takes 156 ms. The different strengths in the upper and lower half of the image are caused by this. The fraction of out-of-time events is $\sim$25 ms/b/2 s in the upper part and $\sim$156 ms/b/2 s in the lower part. The fraction can be significant for short burst options, i.e., for the 0.1 s burst option, the out-of-time events amount to 12.5% in the upper half and 78% in the lower half.

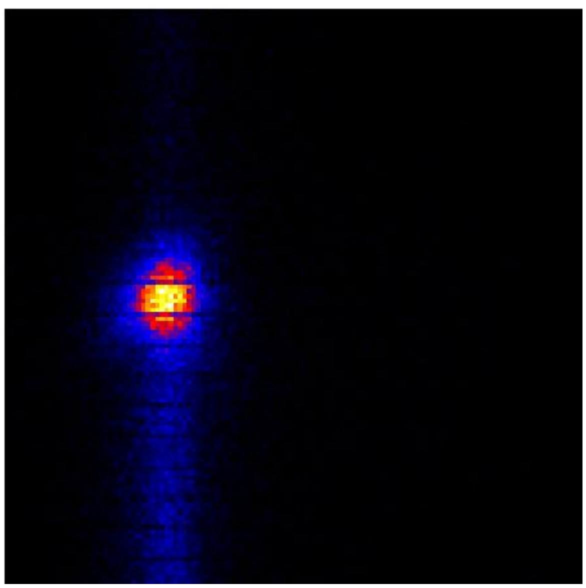

Figure 7.7: XIS1 image showing out-of-time events in an obersvation of the Crab at the HXD nominal position taken with a 0.1 s burst option.

Mitigation The contribution of out-of-time events can be estimated in the area far from the center of the image. This is difficult for observations taken with a window mode. In such cases, at least one of the sensors can be operated without a window option so that it can be used for estimating the out-of-time events also for other sensors.

7.2.2.4 Self Charge Filling

Description In principle, charge traps can be filled not only by artificially injected charges, but also by charges created by X-ray events. This effect is apparent in observations of some very bright sources (Todoroki et al., 2012). This effect is not included in the calibration. Users may encounter a better energy resolution than the distributed RMF files indicate.

Table 7.10: Routine calibration observations and their usage.

Target	Sensor	Mode	Option	Freq (yr^{-1})	Usage
E0102−72[b]	013	Norm	none	4	Gain & resolution at soft band.
	013				Chemical composition of contamination thickness at XIS center.
	013	Norm	1/4w	2	Gain difference for the 1/4 w mode at soft band.
RX J1856.5−3754[b]	013	Norm	none	2	Chemical composition of contamination thickness at XIS center.
PKS 2155–304[b]	013	Norm	1/4w	2	Chemical composition of contamination thickness at XIS center.
N132D[b]	013	Norm	none	2	Gain & resolution at medium band.
Perseus cluster	013	Norm	none	2	Gain & resolution at hard band.
Perseus cluster	013	Norm	1/4w	2	Gain difference for the 1/4 w mode at soft band.
Lockman hole[c]	3	P-sum	none	1	Gain & resolution at hard band.
Cygnus loop[b]	013	Norm	none	2	Spatial-dependence of contamination thickness.
Day earth	013	Norm	none	all time	Spatial-dependence of the contamination thickness.
Night earth	013	Norm	none	all time	NXB.

[a] Additional calibration observations are made upon necessity.
[b] Targets observed with the event threshold of 50 and 20 ADU for the FI and BI sensors, as opposed to normal observations of 100 and 20, respectively. One ADU corresponds to 3.65 eV.
[c] Signals from the ^{55}Fe sources are used for calibration.

7.3 XIS Performance & Calibration

7.3.1 Spaced-Row Charge Injection (SCI)

X-ray CCD devices are subject to degradation in orbit. One of the outcomes is an increase of charge traps under the constant radiation of cosmic rays in the space environment. This results in an increase of the charge transfer inefficiency (CTI), which leads to a degradation of the energy resolution.

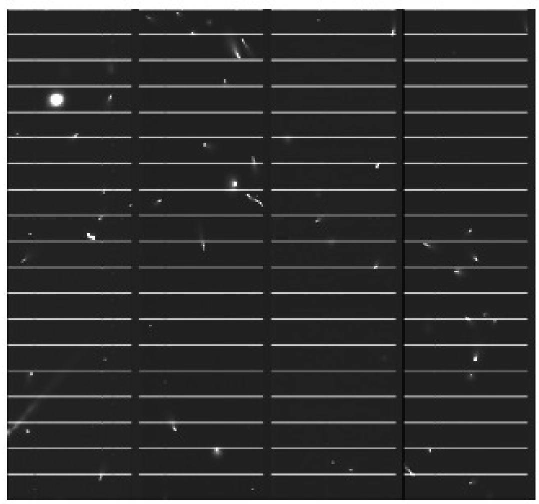

Figure 7.8: Frame dump image of XIS2 with SCI. The bright lines every 54 rows are rows with injected charges. Other events are mostly due to cosmic rays. The gaps between the segments are due to over-clock sampling.

The XIS has a function to precisely monitor and mitigate this effect. For monitoring each sensor has ^{55}Fe calibration sources at two corners on the far-side of the readout. For mitigation spaced-row charge injection (SCI) is implemented. Electrons are injected artificially from one side of the chip and are read out along with charges produced by X-ray events. The artificial charges are injected periodically in space (every 54 rows; Fig. 7.8). They fill up charge traps and thereby alleviate the increase in CTI for charges by X-ray events (Bautz et al., 2004; Nakajima et al., 2008; Uchiyama et al., 2009; Ozawa et al., 2009). SCI is not available for the P-sum clocking mode for its continuous clocking nature.

7.3.1.1 CTI Monitoring & Trend

Fig. 7.9 shows the long-term trend of the measured peak energy and width of the Mn I Kα line (5.9 keV) from the calibration sources. The peak decreases and the width increases gradually. Both quantities are restored by applying SCI.

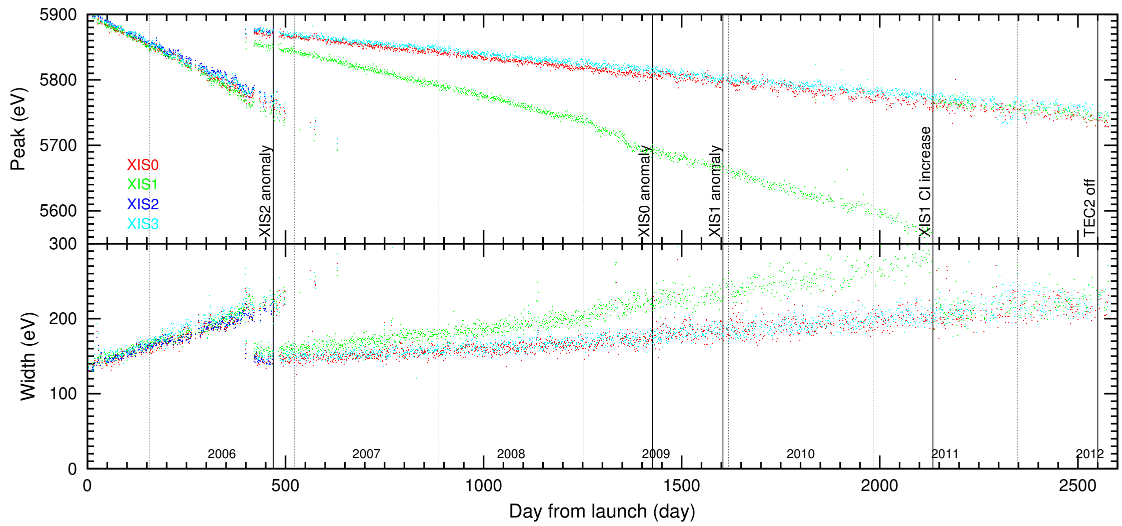

Figure 7.9: Trend of ^{55}Fe peak height and width. These are raw values without trail correction. See Fig. 7.11 for the gain and energy resolution for calibrated data.

7.3.1.2 SCI Operations History

Start of SCI The SCI technique was put into routine operation in the middle of 2006 and has brought a drastic improvement. At the start of SCI operations, it was decided to inject the amount of charges equal to the amount produced by a 6 keV X-ray photon ("6 keV equivalent") for the FI devices and a smaller amount ("2 keV equivalent") for the BI device. The smaller amount for XIS1 was chosen to minimize the expected SCI-related increase in noise in the soft spectral band, at which the BI device has an advantage over the FI device.

Choice of SCI on/off The choice between SCI on and SCI off was a user option for nearly one year after the start of SCI operations. This was because SCI observations suffer from a larger dead area and a larger fraction of out-of-time events in addition to providing an improved spectroscopic performance. The user option was terminated and all observations have been made exclusively with SCI on since AO4, as the number of users choosing SCI off had decreased substantially.

SCI Increase for XIS1 The accumulation of contaminating material on the surface of the CCDs made the soft-band advantage of the BI sensor less prominent (§ 7.3.3). The CTI for the BI device has increased at a faster rate due to the smaller amount of injection charges. As a consequence, the astrophysically important lines of Fe XXV (6.7 keV) and Fe XXVI (7.0 keV) became hardly resolved in 2010. The injection charge amount was changed from 2 keV to 6 keV equivalent for the BI sensor according to the schedule of Table 7.1. Detailed information can be found in the Suzaku memo 2010-07 available at `http://www.astro.isas.ac.jp/suzaku/doc/suzakumemo/suzakumemo-2010-07v4.pdf`.

7.3.1.3 SCI Notes for Users & Proposers

Users need to be aware of some drawbacks associated with the SCI operations:

- The injection rows and the rows immediately before and after the injection rows are dead areas, which amount to 5.6% of the image. The width of the dead rows are much smaller than the telescope PSF. Therefore, this does not significantly impact the imaging analysis.
- For the BI data with 6 keV equivalent charges, events in the second next rows to the charge injection rows may have wrong grades assigned. Details can be found at `http://www.astro.isas.jaxa.jp/suzaku/analysis/xis/xis1_ci_6_nxb/`.
- The number of out-of-time events increases. It takes a longer time (25 ms for SCI off versus 156 ms for SCI on) to transfer the data in the imaging area due to extra time needed to inject charges. The fraction of the out-of-time events increases from 0.3% to 2.0%.
- The number of hot pixels, which are removed in the data processing, slightly increases for SCI on.

7.3.2 Energy Gain and Resolution

The calibration of the spectroscopic performance of the XIS mainly consists of calibrating the energy gain and resolution. Regarding the energy gain, corrections for charge trails and for the CTI are performed.

For the energy resolution, the time-dependence is modeled as

$$\Delta E(\mathrm{PH_0}, t) = \sqrt{a(t) + b(t)\mathrm{PH_0} + c(t)\mathrm{PH_0}^2}, \tag{7.5}$$

where $\mathrm{PH_0}$ is the pulse height of the incident X-rays and t is the time from the launch. The time variable parameters $a(t)$, $b(t)$ and $c(t)$ are determined phenomenologically using the ^{55}Fe calibration sources and the E0102−72 observations.

For the normal clocking modes, data taken with the 3×3 and 5×5 editing modes are merged, since it is known that their differences are negligible.

7.3.2.1 Energy Calibration Results (1) — Normal Mode (No Options)

The Normal mode without options is the best calibrated mode of the XIS. The CTI is measured using observations of the Perseus Cluster (all segments, hard band), 1E0102−72 (segments B and C, soft band), and the ^{55}Fe calibration sources (segments A and D, hard band). Fig. 7.10 and 7.11, respectively, show the gain and energy resolution in the hard band using the ^{55}Fe calibration sources, while Fig. 7.12 and 7.13, respectively, show the gain and energy resolution in the soft band using the E0102−72 observations.

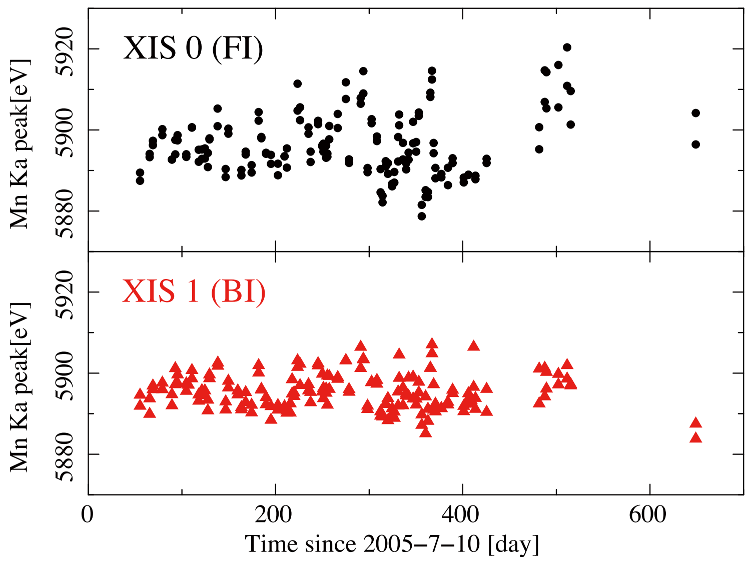

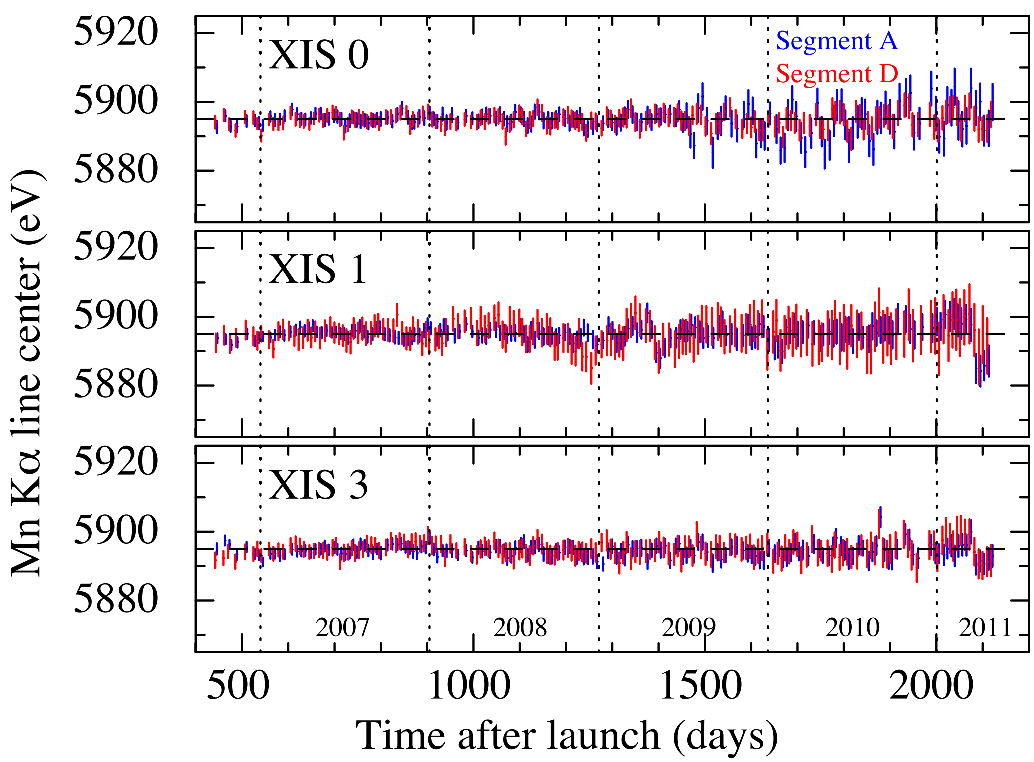

Figure 7.10: Gain in the hard band for the Normal mode (without options) using the ^{55}Fe calibration sources. The upper panel shows the data before turning on the SCI and the lower panel after. The CTI is corrected.

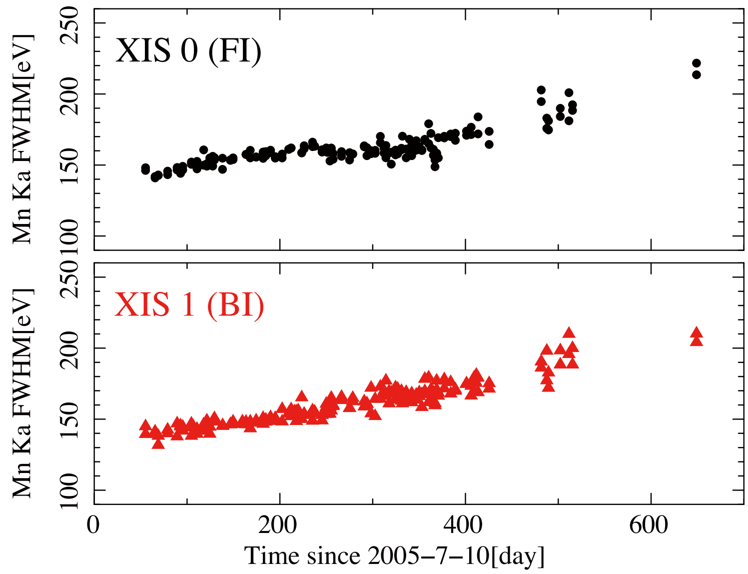

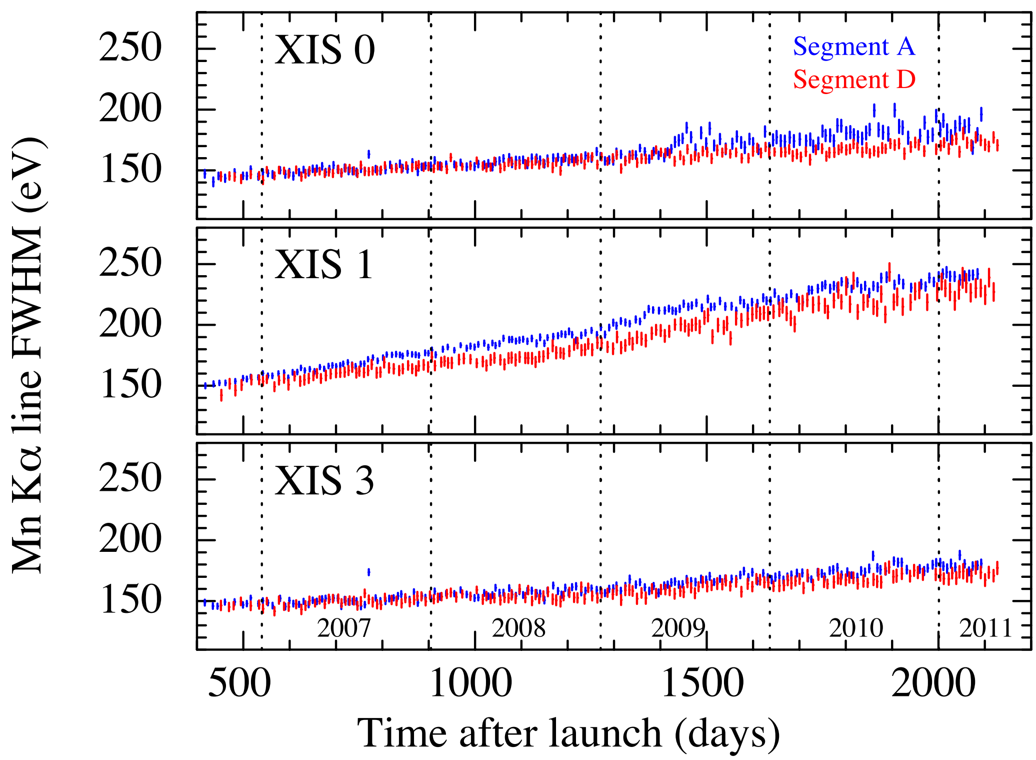

Figure 7.11: Energy resolution in the hard band for the Normal mode (without options) using the ^{55}Fe calibration sources. The upper panel shows the data before turning on the SCI and the lower panel after. The CTI is corrected.

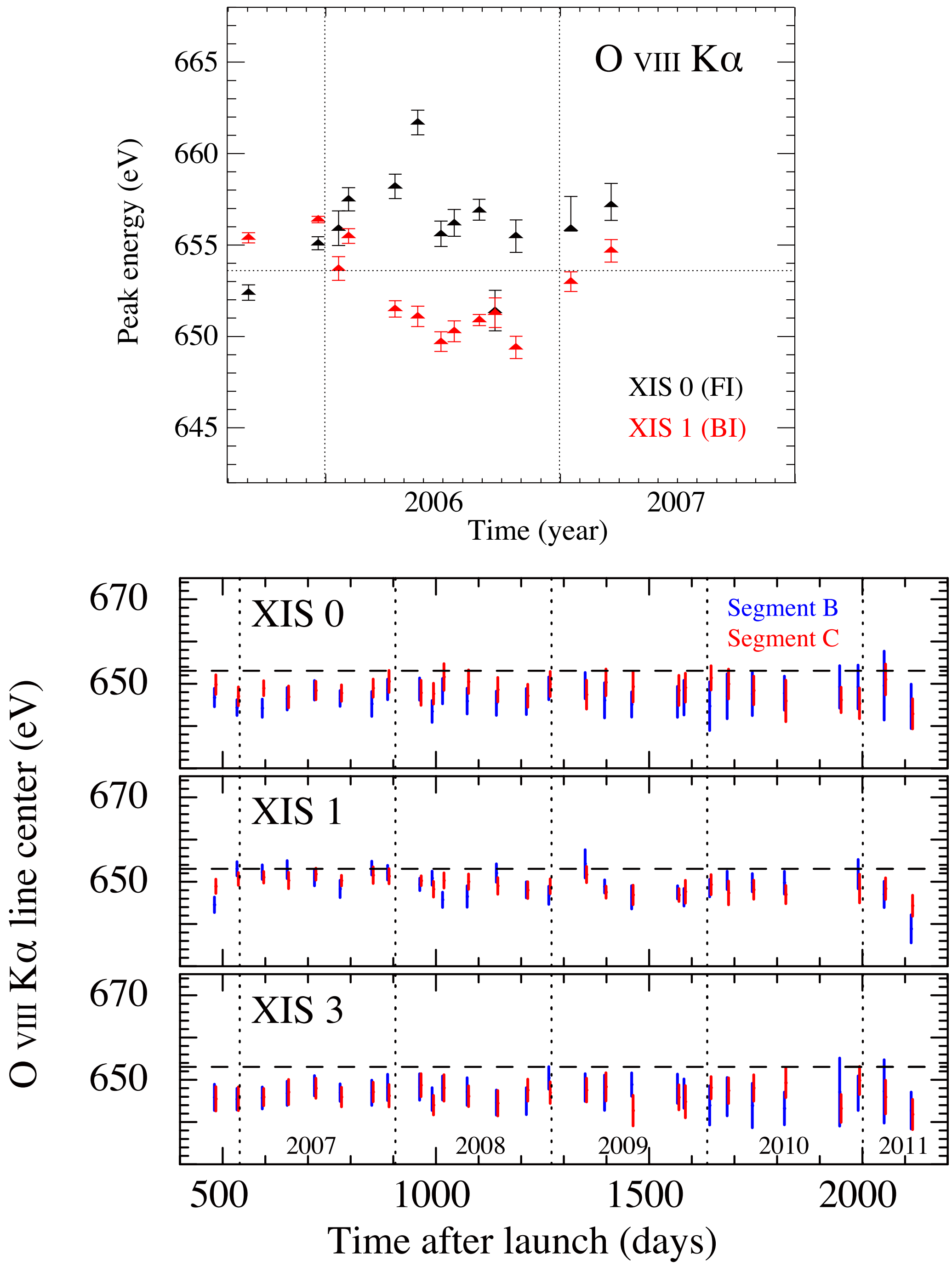

Figure 7.12: Gain in the soft band for the Normal mode (without options) using E0102−72 observations. The upper panel shows the data before turning on the SCI and the lower panel shows after. The CTI is corrected.

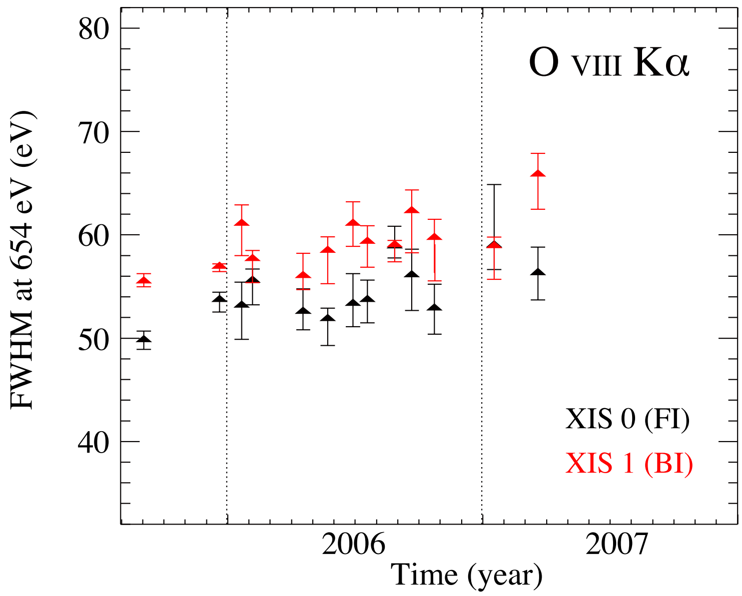

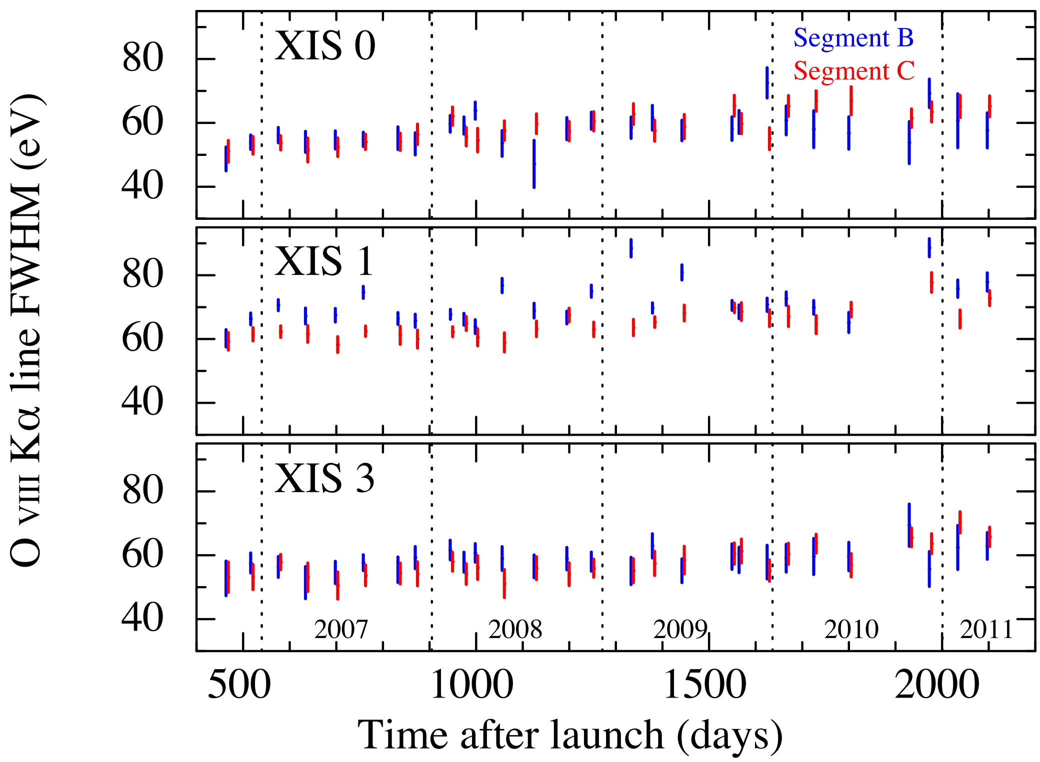

Figure 7.13: Energy resolution in the soft band for the Normal mode (without options) using the E0102−72 observations. The upper panel shows the data before turning on the SCI and the lower panel after. The CTI is corrected.

7.3.2.2 Energy Calibration Results (2) — Other Clocking Modes

Normal mode (window option) Since the ^{55}Fe calibration sources are unavailable for observations with window options, the Perseus Cluster is regularly observed with the 1/4 window option for calibration purposes (Table 7.10). The target is observed in Normal mode twice, without option and with 1/4 window option, with consecutive exposures, in order to construct a comparison data set at each epoch. No calibration sources are observed with the 1/8 window option. The pulse height correction for the Normal mode with window option is the same as that for the Normal mode without options, except that they use different numbers of fast and slow charge transfers. Fast and slow transfers are used for reading out the effective imaging area and the non-imaging area, respectively. They have different CTIs. For the window options, the non-imaging area includes the frame store area as well as the imaging area outside of the window. The CTI for each transfer is calibrated using the calibration observations with the 1/4 window option, which is also applied to the 1/8 window option. Fig. 7.14, 7.15, and 7.16 show the resulting gain using several emission lines, comparing the Normal mode without options and the Normal mode with 1/4 window option. The two gain calibrations are consistent to within ∼5 eV over the entire energy band for the whole mission to date.

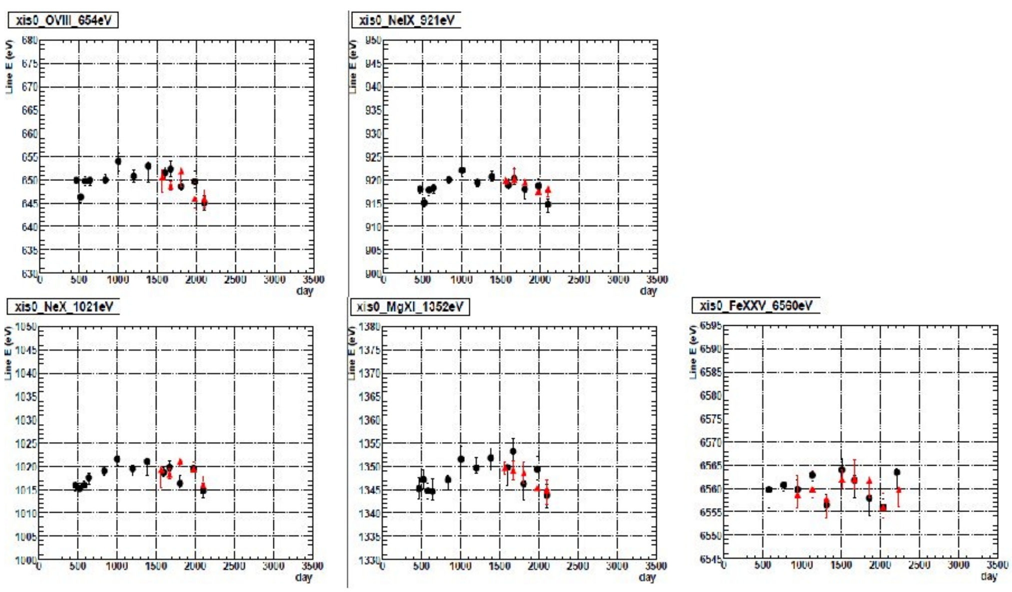

(a) XIS0

Figure 7.14: Comparison of the gain in the Normal mode with 1/4 window option (red) and with no option (black) for five conspicuous emission lines in XIS0. Events of all segments are used.

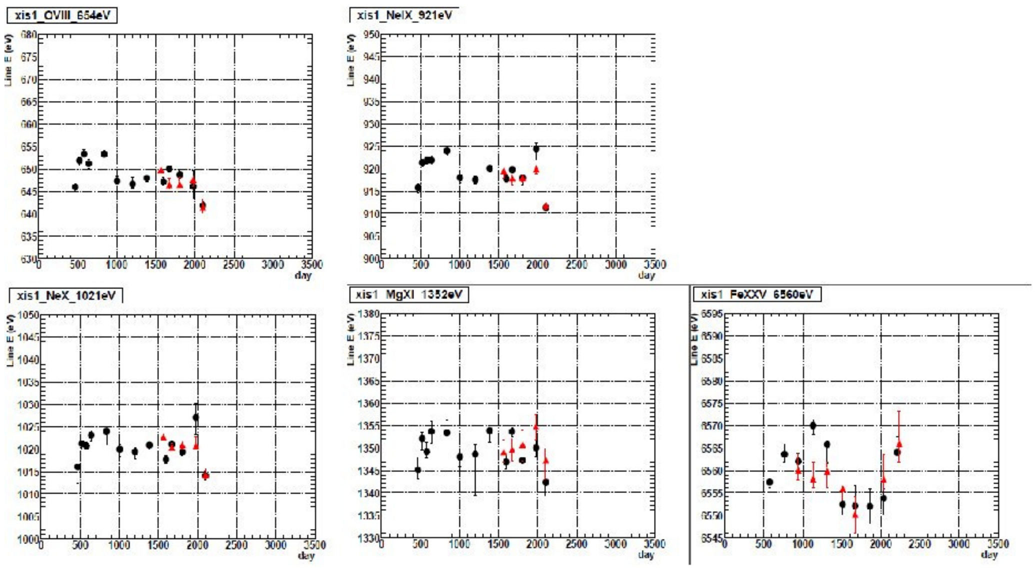

(a) XIS1

Figure 7.15: Comparison of the gain in the Normal mode with 1/4 window option (red) and with no option (black) for five conspicuous emission lines in XIS1. Events of all segments are used.

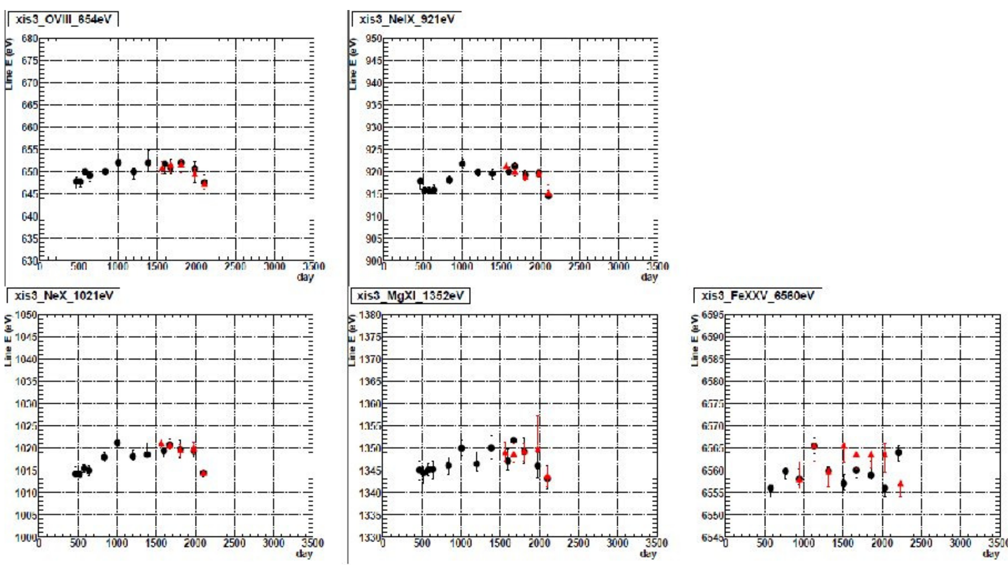

(a) XIS3

Figure 7.16: Comparison of the gain in the Normal mode with 1/4 window option (red) and with no option (black) for five conspicuous emission lines in XIS3. Events of all segments are used.

Normal mode (burst option) For the calibration of the Normal mode with burst option advantage is taken of the Crab calibration observations (which are primarily performed for HXD calibration purposes). Since the Crab has a featureless spectrum, the ^{55}Fe calibration source spectra are used in addition (Table 7.10). In the Normal mode with burst option no correction is made in addition to those for the Normal mode without options. The calibration observations are only used to confirm that there is no change in the instrumental response for the burst options. Fig. 7.17 shows a ^{55}Fe calibration source spectrum taken with the 2.0 s burst option during an observation of GX 17+2. It has been modeled using the RMF for the Normal mode (without options). There is no structure in the residuals. This is indicating that the response is the same for the Normal mode without options and the Normal mode with the 2.0 s burst option.

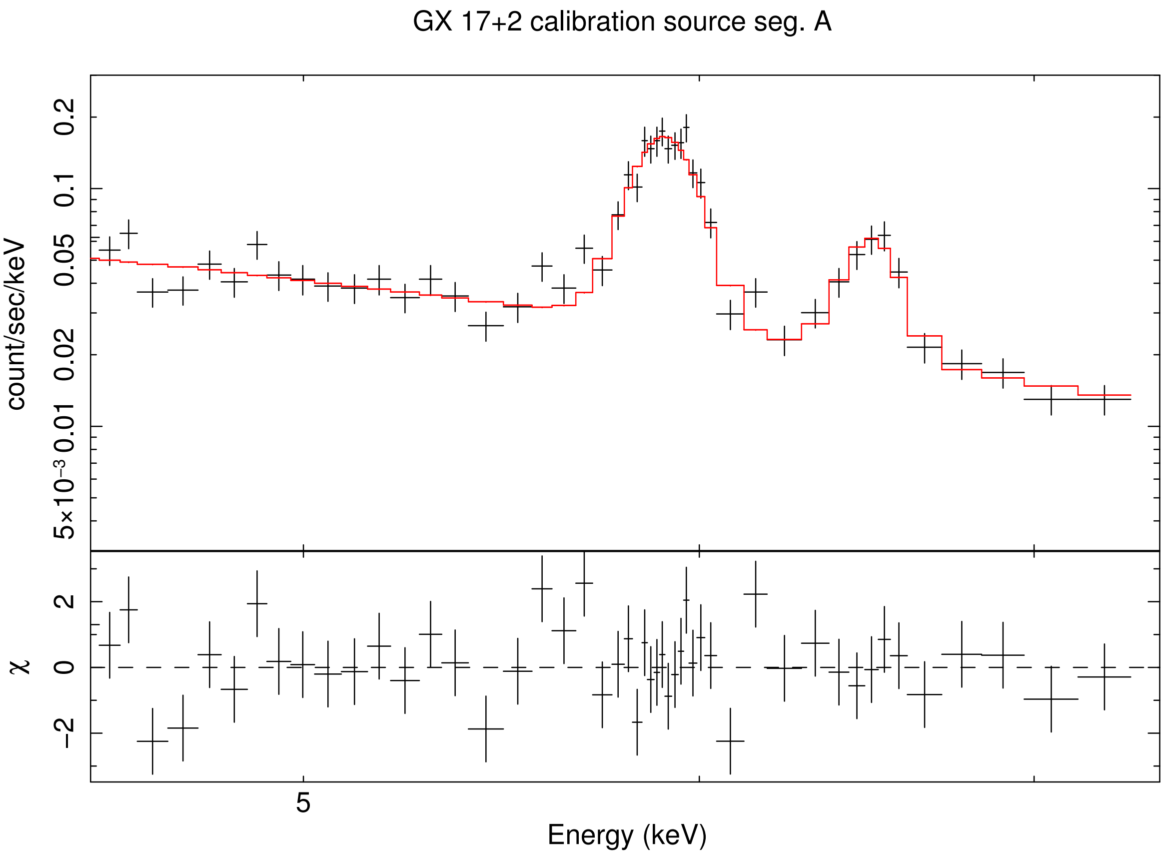

Figure 7.17: ^{55}Fe spectrum of a 2.0 s burst mode observation of GX17+2. The spectrum is fitted with a continuum plus two Gaussian lines using the response generated for the Normal mode (no burst option).

P-sum mode Because of the unavailability of the spaced-row charge injection technique for the P-sum clocking mode (§ 7.3.1), the data taken in this mode suffer from a substantially worse energy resolution than those taken with the Normal clocking mode. The P-sum clocking mode is only combined with the timing editing mode (§ 7.2.1.2), which has limited information about the charge distribution around an event. This makes the background level of the P-sum mode much higher than that of the Normal mode. Fig. 7.18 shows the history of phenomenological gain of the P-sum data. Fig. 7.19 shows the energy resolution for two representative lines, one in the soft and one in the hard band.

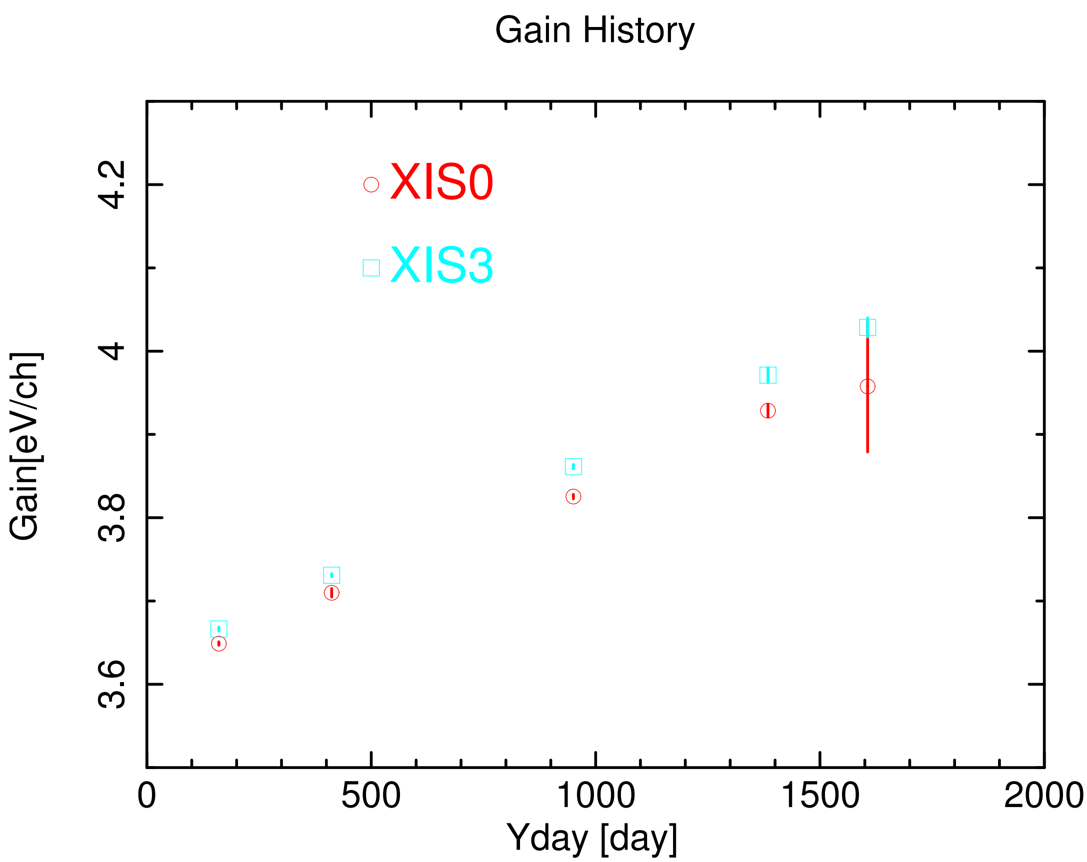

Figure 7.18: History of the P-sum gain.

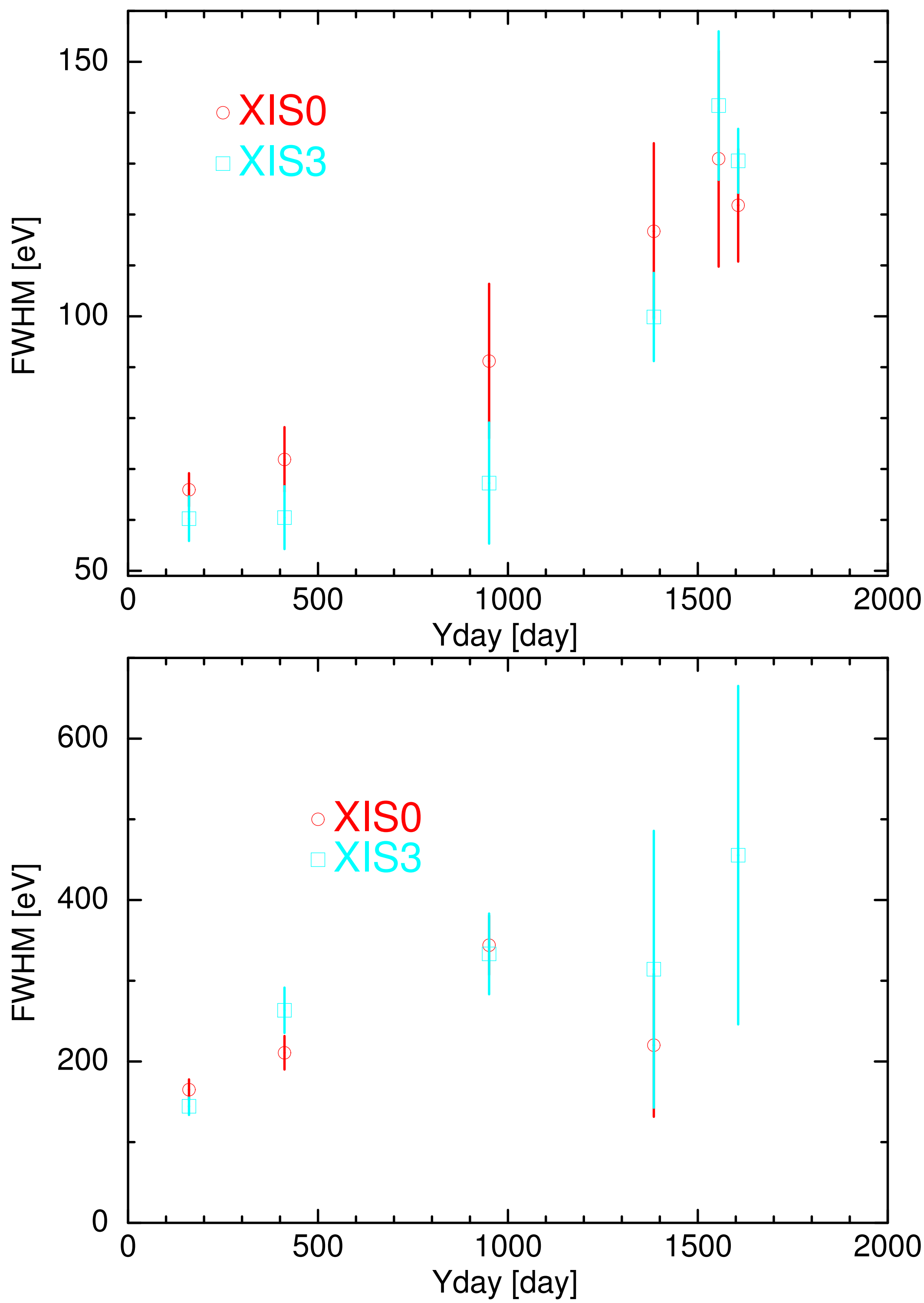

Figure 7.19: History of the P-sum energy resolution. The upper panel shows the change for the Ne IX Kα line, whereas the lower panel shows the change for the Mn I Kα line.

7.3.2.3 Energy Calibration Results (3) — Other Editing Modes

2×2 editing mode The data taken with the 2×2 editing mode have insufficient information to conduct trail correction around each event, unlike those taken with the 3×3 or 5×5 editing modes. It is therefore inevitable for the 2×2 editing mode to have different gain compared to the other editing modes. In particular, the gain difference between 3×3/5×5 and 2×2 depends on the ACTY position of the imaging area. Since the 2×2 editing mode is only used for very bright point-like sources for the purpose of reducing telemetry and since these observations are made at the XIS nominal position, the 2×2 editing mode data are calibrated such that the gain difference between 3×3/5×5 and 2×2 modes is minimal at the image center. Fig. 7.20 shows the difference of the 2×2 and 5×5 editing mode gains in the soft and hard energy bands at several different ACTY positions. At the center (ACTY=512), the difference is within $\sim$3 eV. For calibration purposes, 2×2 editing mode data are artificially generated on the ground using the 3×3 or 5×5 editing mode data for the Perseus cluster (Table 7.10).

7.3.2.4 Energy Calibration Notes for Users & Proposers

Users can exploit the calibration results presented above by using the `xisrmfgen` tool. Remaining issues include the following:

Si K In all clocking/editing modes, uncertainties of the gain and energy resolution calibration at the Si K edge remain prominent for the FI devices. It is currently advised to remove data between 1.8 and 2.0 keV from spectral fitting. For the BI device, a workaround has been implemented in the CALDB in 2012 which is mitigating this uncertainty.

Au M Some uncertainties still remain in the Au M band, with Au having been used for the surface coating of the mirrors. This is visible for very bright sources. Users need to remove data taken in the relevant energy band from spectral fitting.

Al K Some uncertainties still remain in the Al K band, with Al having been used for the electrodes in the CCD. This is visible for very bright sources. Users need to remove data taken in the relevant energy band from spectral fitting.

>10 keV The background level is higher than expected in the energy band above $\sim$10 keV. The cause for this is not yet identified.

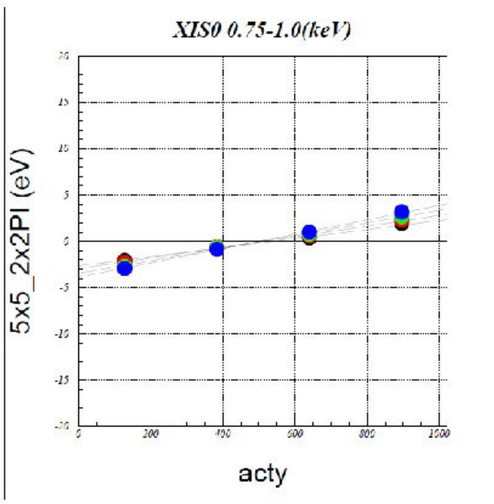

(a) XIS0, soft-band

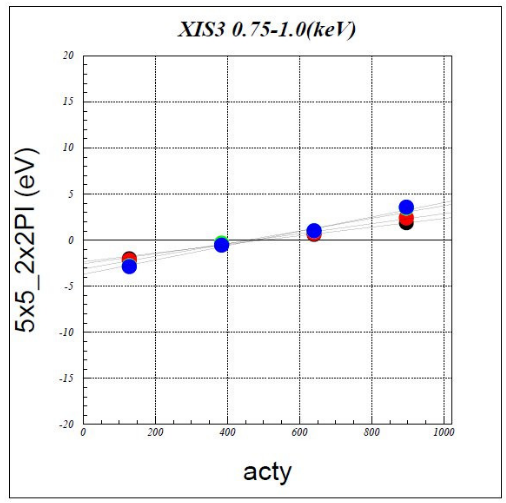

(b) XIS3, soft-band

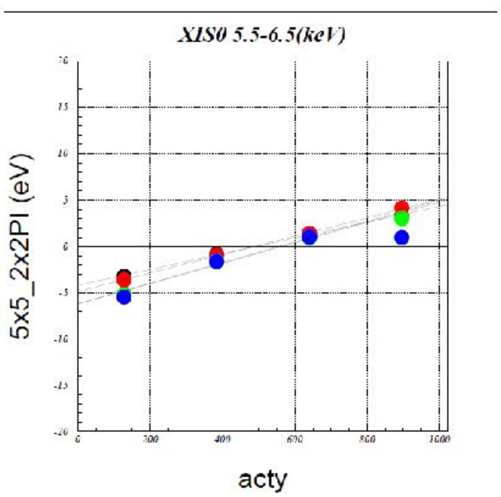

(c) XIS0, hard-band

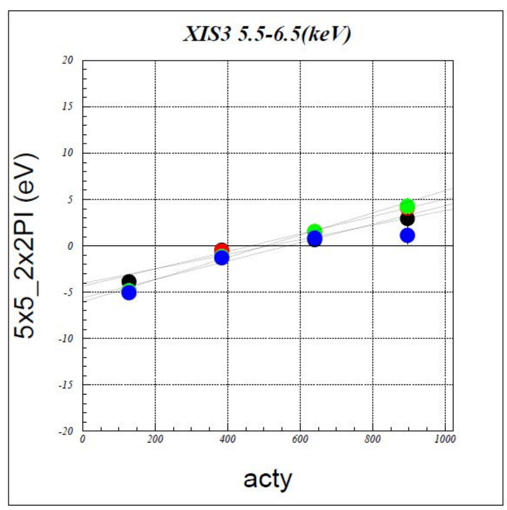

(d) XIS3, hard-band

Figure 7.20: Energy gain for the 2×2 and 5×5 editing modes as a function of ACTY position for XIS0 and XIS3 in the soft and hard energy band for several different epochs: 2008/02 (black), 2009/02 (red), 2010/02 (green), and 2011/02 (blue).

7.3.3 Contamination & Low Energy Quantum Efficiency Degradation

The quantum efficiency below ∼2 keV has been decreasing since launch due to accumulation of contaminating material on the optical blocking filter (OBF) of each sensor. The OBF is cooler than other parts of the satellite, thus it is prone to the accumulation of contamination. The contaminant consists of several different materials with time-varying composition. The time dependence of the thickness and the chemical composition of the contaminant at the XIS nominal position are monitored and calibrated, as well as the spatial dependence of the thickness across the field of view (Table 7.10).

7.3.3.1 Contamination Calibration Results

Time dependence of the chemical composition of the contaminant The chemical composition is modeled phenomenologically with time-varying columns of H, C, N and O. Three calibration sources — RX J1856.5−3754 (a super-soft isolated neutron star), PKS 2155−304 (a blazar), and 1E0102.2−7219 (a line-dominated supernova remnant) — are used to derive the chemical composition at each epoch of the observations. The spectral models by Burwitz et al. (2003) for RX J1856.5−3754, a simple power-law model for PKS 2155−304, and the model by Plucinsky et al. (2008) for 1E0102.2−7219 are used as standard models. Fig. 7.21 shows the result of XIS1 fitting for RX J1856.5−3754 using the 2012 contamination model for selected epochs.

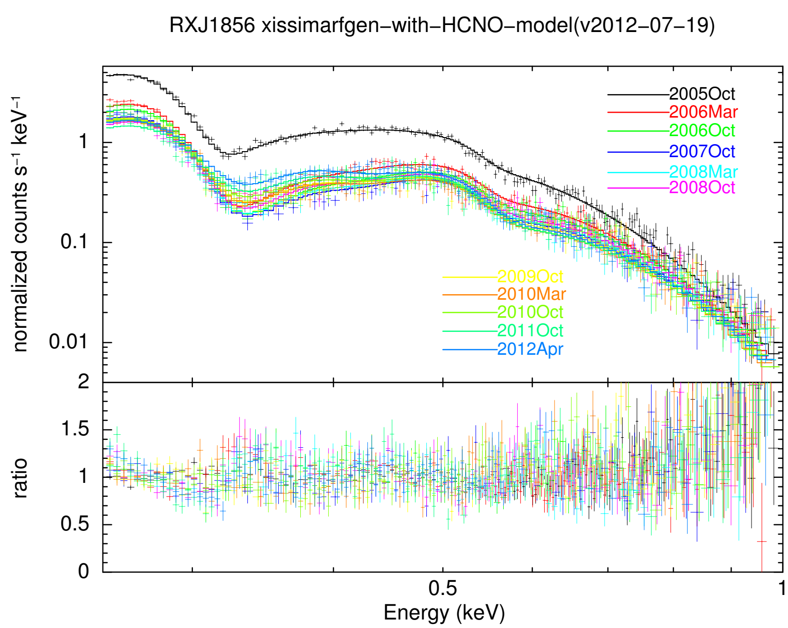

Figure 7.21: Results of spectral fitting of the BI spectrum of RX J1856.5−3754 with the 2012 contamination model at the XIS nominal position for several different epochs.

Time dependence of the thickness of the contaminant The time dependence of the thickness of the contaminant is modeled with phenomenological functions of time, separately for each composition and sensor. Fig. 7.22, 7.23, and 7.24 show the evolution of the thickness for different elements, while Fig. 7.25 shows the combined optical thickness and the relative reduction of the effective area for two different energies. The thickness increased rapidly for one year after launch and continued to increase at a moderate pace thereafter. The N component is used for the XIS1 only.

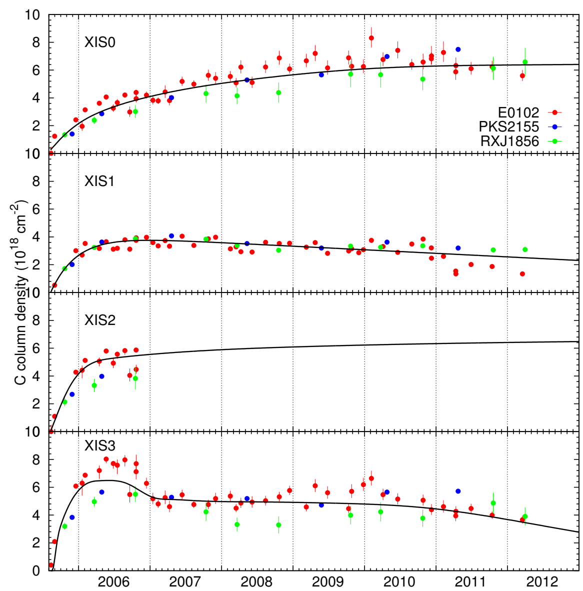

Figure 7.22: Time dependence of the C thickness at the XIS nominal position for each sensor. The solid curves indicate the phenomenological trend model.

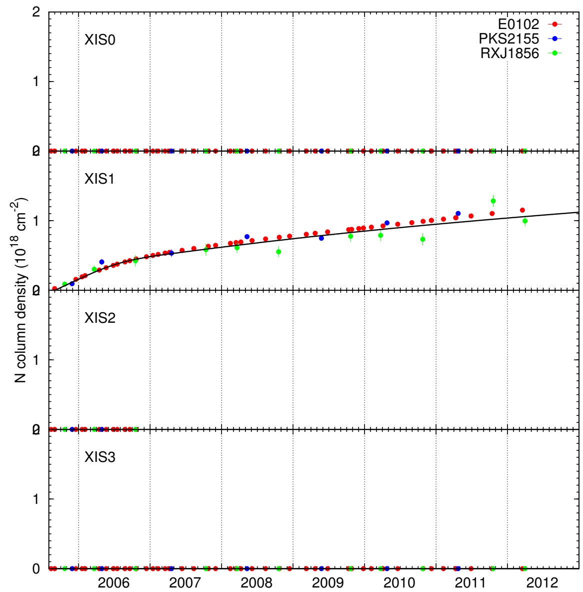

Figure 7.23: Time dependence of the N thickness at the XIS nominal position for each sensor. The solid curves indicate the phenomenological trend model.

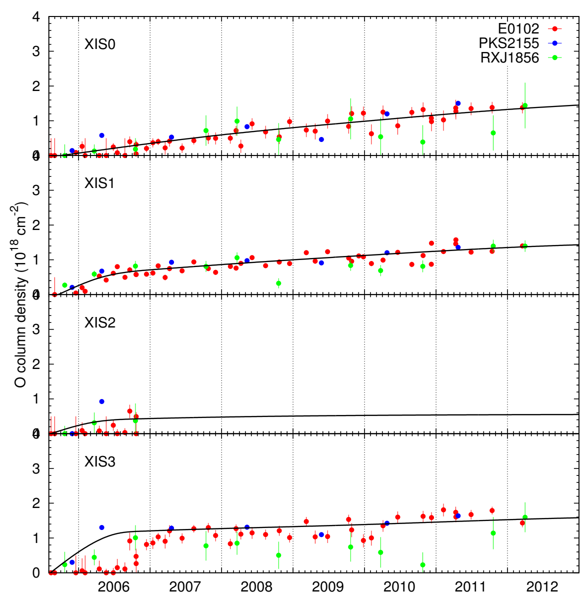

Figure 7.24: Time dependence of the O thickness at the XIS nominal position for each sensor. The solid curves indicate the phenomenological trend model.

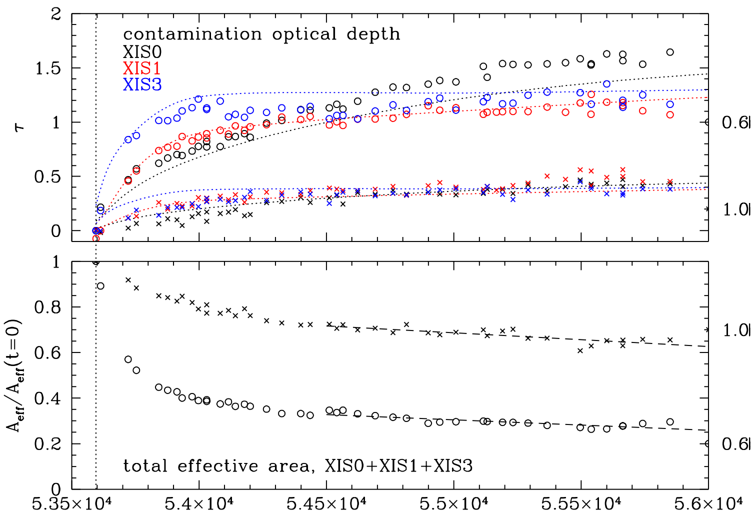

Figure 7.25: Time dependence of the combined optical depth (*top panel*) and the relative reduction of the effective area (*bottom panel*). In both panels circles are used for measurements at 0.65 keV and crosses for those at 1.0 keV.

Spatial dependence of the thickness of the contaminant The spatial distribution of the contaminants is monitored and calibrated using regular observations of a part of the Cygnus Loop, a thermal supernova remnant. The atmospheric fluorescent K lines of N I and O I, which illuminate the entire field of view when the telescope is oriented toward the day earth, are used as well. The model of the spatial dependence assumes a radially symmetric pattern (Koyama et al., 2007). The chemical composition and the thickness at the center are normalized to the values presented in Fig. 7.22, 7.23, and 7.24. Different sensors have different radial profiles (Fig. 7.26).

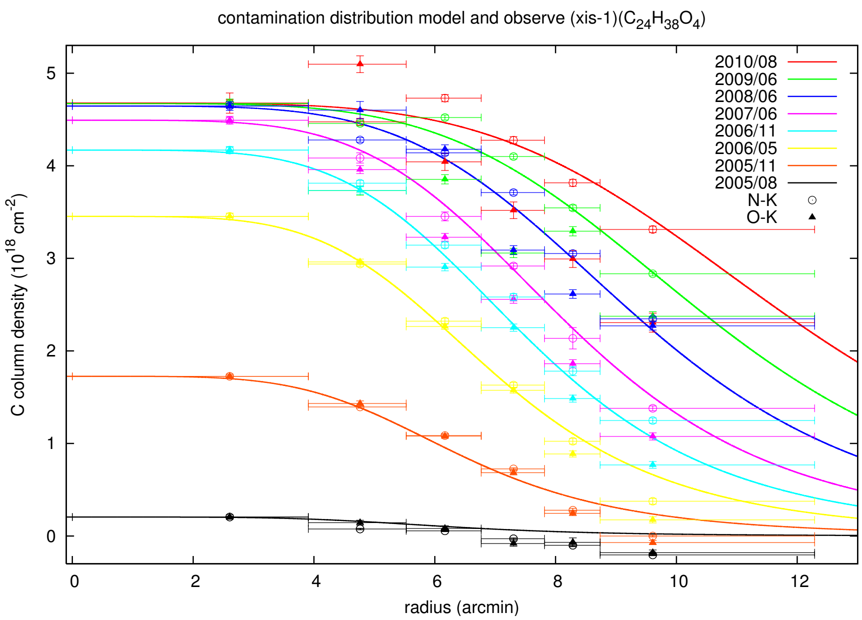

Figure 7.26: Spatial dependence of the thickness derived from day earth observation data at different epochs. Open circles and filled triangles represent the data points determined by the N and O lines, respectively. The best fit models are shown as solid curves.

7.3.3.2 Contamination Notes for Users & Proposers

The contaminant calibration results are available for use through the ARF generation tools `xissimarfgen` (Ishisaki et al., 2007) and `xisarfgen`. It is discouraged to use the generic contamination models in the `XSPEC` package (e.g., `xisabs`, `xiscoabs`, `xiscoabh`, `xispcoab`). For proposal writers ARF files are provided that assume a contamination thickness extrapolated to the middle of the next AO cycle, based on the current trend. Although a major revision of the contamination model was made in 2012, that model still shows some discrepancies compared to observations. Fig. 7.27 shows results of fitting E0102−72 data using the 2012 contamination model.

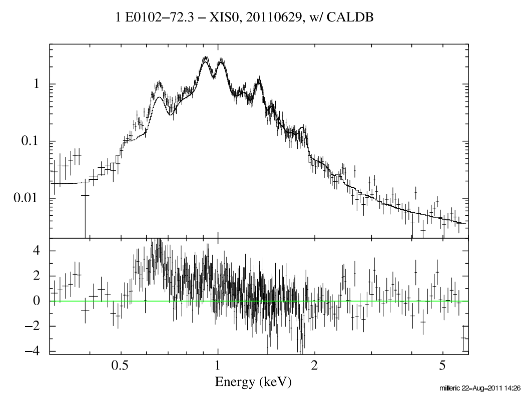

(a) XIS0

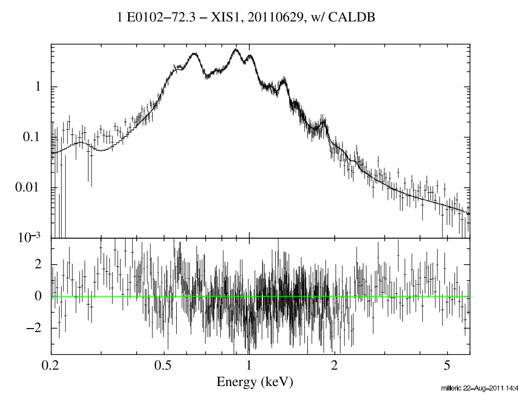

(b) XIS1

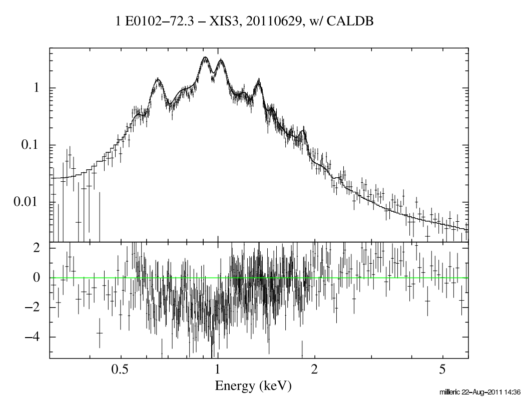

(c) XIS3

(d)

Figure 7.27: Results of fitting the 2012 contamination model using the E0102−72 data taken on 2011-06-29.

7.3.4 Non X-Ray Background

The Non X-ray Background (NXB) has several sources. The most dominant source are events produced by ionization losses of charged cosmic ray particles. Others include fluorescence X-rays from materials used in the spacecraft and the ^{55}Fe calibration sources attached to the door of each sensor (opened immediately after the launch). Most of the NXB events are discarded onboard as grade 7 events. The NXB of the XIS is known to be very stable on time scales of months and thus the NXB spectrum can be constructed using data obtained when the spacecraft is pointed toward the Earth at night. The NXB database is accessible as part of the CALDB, which is updated biannually in June and December.

7.3.4.1 NXB Calibration Results

NXB Intensities and spectra Fig. 7.28 shows the NXB spectrum for each sensor. The background rate in the 0.4–12 keV band is 0.1–0.2 counts s^{-1} for the FI CCDs and 0.3–0.6 counts s^{-1} for the BI CCD after grade selection. Table 7.11 shows the current best estimates for the strength of major XIS emission features, along with their 90% confidence errors.

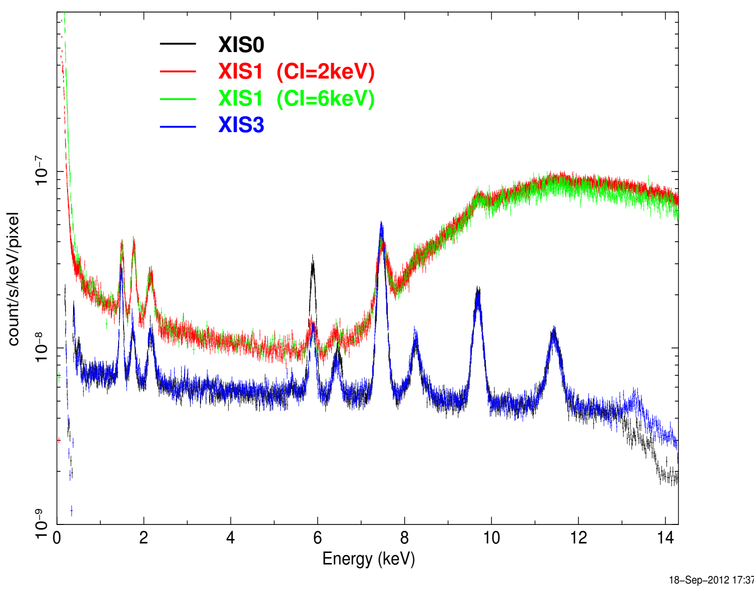

Figure 7.28: Non X-ray background (NXB) rate for XIS0 (black), XIS1 (red), and XIS3 (blue). The spectra are constructed from night Earth observations.

NXB cut-off rigidity dependence The total intensity of the NXB depends strongly on the geomagnetic cut-off rigidity (COR), as the dominant source of the background

Table 7.11: Strength of conspicuous emission lines in the NXB spectrum. The count rates are obtained from the entire CCD chip except for the corners irradiated by the calibration source. The errors are the 90% statistical uncertainties (Tawa et al., 2008).

Line	Energy [keV]	XIS0 [10^{-9} cps/pix]	XIS1 [10^{-9} cps/pix]	XIS2 [10^{-9} cps/pix]	XIS3 [10^{-9} cps/pix]
Al Kα	1.486	1.45 ± 0.11	1.84 ± 0.14	1.41 ± 0.10	1.41 ± 0.10
Si Kα	1.740	0.479 ± 0.081	2.27 ± 0.15	0.476 ± 0.080	0.497 ± 0.082
Au Mα	2.123	0.63 ± 0.093	1.10 ± 0.13	0.776 ± 0.097	0.619 ± 0.092
Mn Kα	5.895	6.92 ± 0.19	0.43 ± 0.14	1.19 ± 0.13	0.76 ± 0.11
Mn Kβ	6.490	1.10 ± 0.11	0.26 ± 0.13	0.40 ± 0.11	0.253 ± 0.094
Ni Kα	7.470	7.12 ± 0.19	7.06 ± 0.37	8.01 ± 0.20	7.50 ± 0.20
Ni Kβ	8.265	0.96 ± 0.10	0.75 ± 0.22	1.16 ± 0.11	1.18 ± 0.11
Au Lα	9.671	3.42 ± 0.15	4.15 ± 0.49	3.45 ± 0.15	3.30 ± 0.15
Au Lβ	11.51	2.04 ± 0.14	1.93 ± 0.48	1.97 ± 0.14	1.83 ± 0.14

originates from cosmic rays. Fig. 7.29 shows the NXB count rate as a function of the COR. The ftool `xisnxbgen` generates NXB spectra for an observation in such a way that the histogram of the COR is the same between the observation of the source and the night Earth observations. The night Earth data are retrieved from ±150 days of the observation of the source by default. The PIN's Upper Discriminator (PIN-UD) count rate is also useful as a proxy for the COR, and thus the XIS NXB level. Tawa et al. (2008) show that the PIN-UD provides a slightly better reproducibility of the XIS NXB than the COR. The reproducibility of the NXB in the 5–12 keV band is evaluated to be 3–4% of the NXB, when the PIN-UD is used as the NXB sorting parameter.

NXB spatial dependence The NXB is not uniform over the chip. It is stronger toward larger ACTY positions (Fig. 7.30). This is because some fraction of the NXB is produced in the frame-store region. The fraction can be different between the fluorescent lines and the continuum.

NXB time dependence The NXB level changes both continuously and discontinuously. The continuous changes are seen only in the low energy band for the BI sensor, in which a gradual increase in the NXB level is observed (Figure 7.31). The level is stable for the high energy band for the BI and the total band for the FI sensors.

7.3.4.2 NXB Notes for Users & Proposers

NXB change due to the XIS0 anomaly A putative micro-meteorite hit occurred for XIS0 in 2009-06-23. Since then, the XIS0 has been operated with an area discriminator masking the damaged area. In the masked area, the NXB level is zero, which causes an

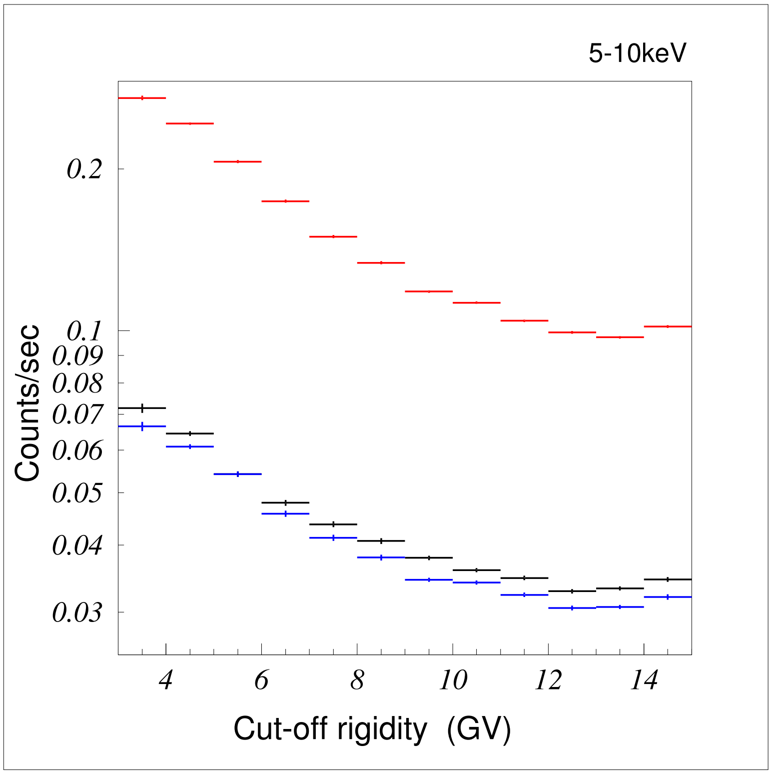

Figure 7.29: Cut-off rigidity dependence of the NXB (average intensity for 5–10 keV) for each sensor. The NXB flux varies by a factor of ∼2 depending on the cut-off rigidity.

apparent discontinuous change in the NXB database. Users generating their own NXB spectrum using `xisnxbgen` need to be aware that they are mixing the NXB data before and after the event if their observations are within ±150 days of the event (between January 24, 2009 and June 27, 2009). A recipe for mitigating this is described at `http://www.astro.isas.jaxa.jp/suzaku/analysis/xis/xis0_area_discrimination/`.

NXB change due to the XIS1 SCI increase The SCI level was increased from 2 to 6 keV in 2010. Due to the increased amount of charges, the NXB level has increased discontinuously. The increase is only seen in the second trailing rows, which are the over-next rows from the rows with charge injection. Users can achieve the same NXB level as for SCI=2 keV by masking events from the second trailing row1s. Details can be found at `http://www.astro.isas.jaxa.jp/suzaku/analysis/xis/xis1_ci_6_nxb/`.

NXB contamination due to the day Earth When the XIS field of view is close to the day Earth (i.e., Sun-lit Earth), fluorescent lines from the atmosphere contaminate the low energy part of the XIS data, especially for the BI chip. Most prominent are the O

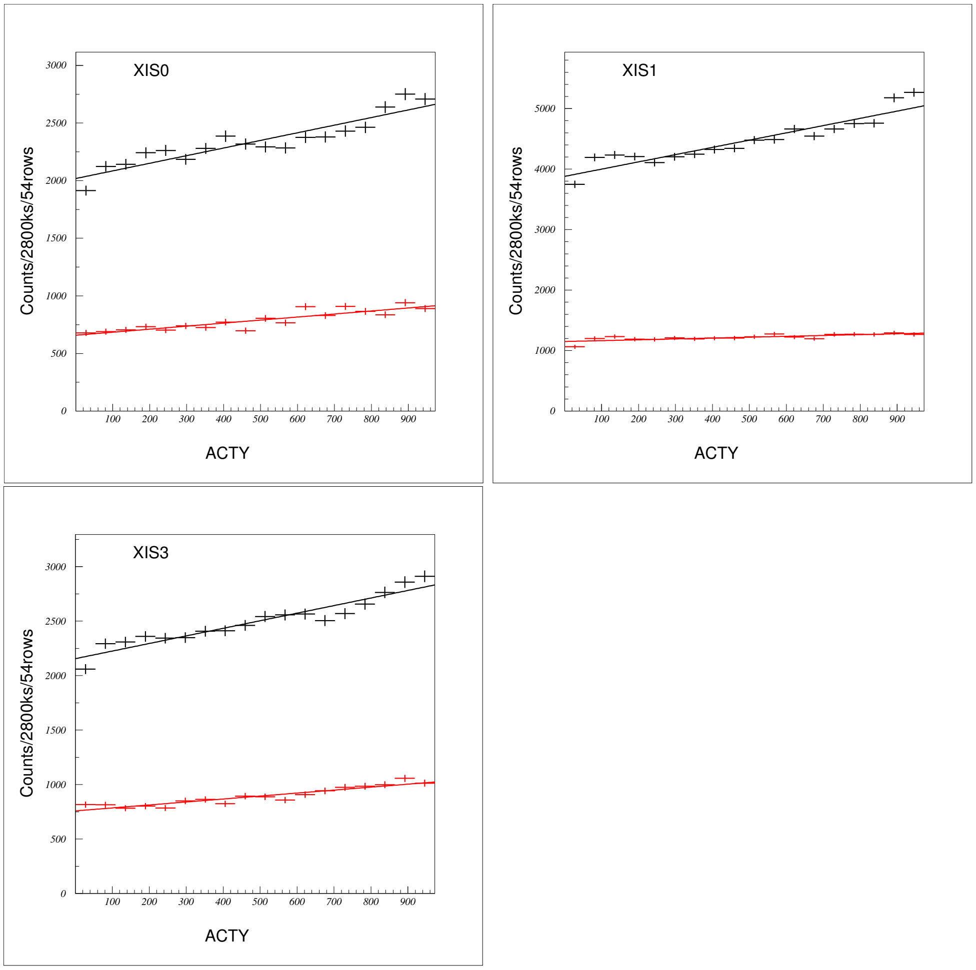

Figure 7.30: ACTY dependence of the NXB for XIS0, XIS1, and XIS3. Black lines indicate the continuum component (2.5–5.5 keV), while the red lines indicate the Ni Kα line component (7.2–7.8 keV). The NXB flux tends to be higher at larger ACTY, because some fraction of the NXB is produced in the frame store region.

and N lines. Although the standard event screening criterion (elevation angle from the day Earth >20 degrees) is sufficient to remove these features, some emission may remain due to the variable nature of the Earth's X-ray albedo. In this case, event screening with a higher elevation angle is recommended.

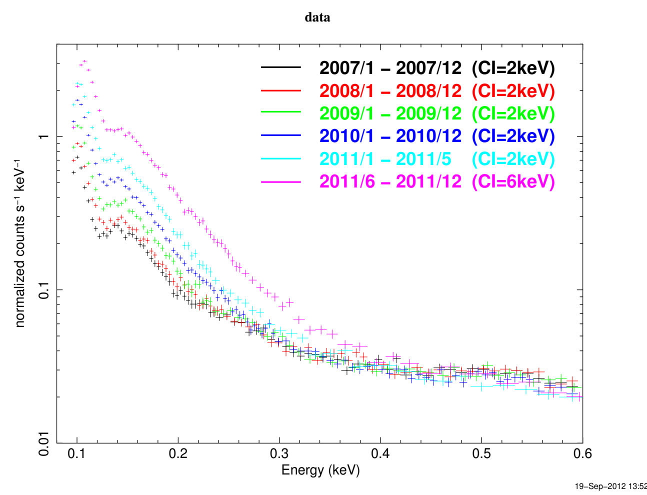

Figure 7.31: Soft NXB spectrum of XIS1 (0.1–0.6 keV) integrated over one year for several epochs. For the CI=6 keV data, the second trailing rows are not removed.

7.3.5 Flux Calibration

The stability of the relative normalization between the three XIS sensors is shown in Fig. 7.32. No significant change with time is found. The relative normalization remains constant. The mean and standard deviation are summarized in Table 7.12 separately for the XIS and HXD nominal positions.

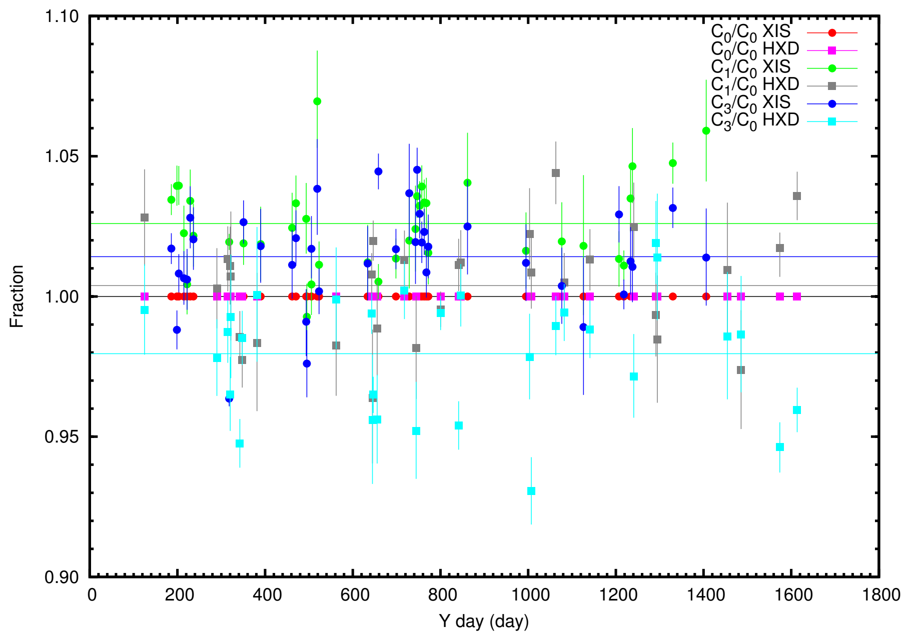

Figure 7.32: Relative flux normalization among different sensors. The ratio of the best-fit normalization values are compared between different combinations of two sensors, at the XIS and the HXD nominal positions. Observations of a power-law source in the Normal clocking mode were used. The average values are shown with solid lines.

Table 7.12: Relative normalization among different sensors.

Position	Ratio	Mean	Standard deviation
XIS-norm	XIS1/XIS0	1.026	0.016
	XIS3/XIS0	1.014	0.017
HXD-norm	XIS1/XIS0	1.004	0.019
	XIS3/XIS0	0.980	0.022

7.3.6 Putative Micro-Meteorite Hits

Sudden anomalies caused putatively by micro-meteorite hits have affected XIS0, XIS1, and XIS2. The entire XIS2 was lost in 2006. A part of the XIS0 was lost in 2009, which is masked by area discrimination since then. A very small hole was created in the optical blocking filter for the XIS1, but the sensor remains intact.

Event on 2006-11-09 for XIS2 The anomaly of XIS2 suddenly occurred on Nov. 9, 2006, 1:03 UT. About 2/3 of the image was flooded with a large amount of charge, which had leaked somewhere in the imaging region. When the anomaly occurred, the satellite was out of the SAA and the XIS sensors were conducting observations in the Normal mode (SCI on, without any options). Various tests to check the condition of XIS2 revealed that (1) the four readout nodes of the CCD and the corresponding analog chain were all working fine, (2) the charge injection was not directly related to the anomaly, but may have helped to spread the leaked charge. When the clock voltages were changed in the imaging region, the amount of leaked charge changed as well. This indicates a short between the electrodes and the buried channel. Possible mechanisms to cause the short include a micro-meteoroite impact on the CCD, as seen, e.g., on *XMM-Newton* and *Swift*. Although there is no direct evidence to indicate an micro-meteoroite impact, the phenomenon observed for XIS2 is not very different from what is expected from such an event. The low-earth orbit and the low-grazing-angle mirrors of *Suzaku* may have enhanced the probability of a micro-meteoroite impact. An attempt to reduce the leaked charge by changing the clock pattern and voltages in the imaging region was not successful. Therefore it was decided to stop operating the sensor. It is unlikely that operation of the XIS2 will be resumed in the future. More details can be found at
`http://www.astro.isas.jaxa.jp/suzaku/doc/suzakumemo/suzakumemo-2007-08.pdf`.

Event on 2009-06-23 for XIS0 XIS0 suddenly showed an anomaly on June 23, 2:00 UT. During Normal clocking operations, a part of segment A of XIS0 was flooded with a large amount of charges, which caused saturation of the analogue electronics. The anomaly was very similar to that which occurred in the XIS2 in 2007. It is therefore suspected that both anomalies have the same origin, possibly a micro-meteorite impact.The effect is confined to 1/8 of the area of XIS0. The XIS team continues to operate XIS0. Users need to be aware of several remaining artifacts after the event:. In the Psum clocking mode, the effect spreads to the entire XIS0 with severe data degradation. The XIS team discontinues the use of Psum clocking mode for the XIS0. More details can be found at
`http://www.astro.isas.jaxa.jp/suzaku/doc/suzakumemo/suzakumemo-2010-01.pdf`.

Event on 2009-12-18 for XIS1 XIS1 suddenly showed an anomaly some time between Dec 18, 2009 12:50 UT and 14:10 UT. A bright and persistent spot suddenly appeared at one end of segment C in all images taken during day Earth observations, while none was found during night Earth observations. It is speculated that the anomaly stems from optical light leaked from a hole with a size of $\sim$7.5 μm in the optical blocking filter created by a micro-meteorite hit. From diagnostic observations, it was concluded that the scientific impact of this anomaly is minimal. XIS1 has been and will be operated in the same way as before the anomaly. More details can be found at `http://www.astro.isas.jaxa.jp/suzaku/doc/suzakumemo/suzakumemo-2010-03v2.pdf`.

7.4 XIS Onboard Processing

7.4.1 Pulse Height Determination & Hot Pixel Rejection

When a CCD pixel absorbs an X-ray photon, the X-ray is converted to an electric charge, which in turn produces a voltage at the analog output of the CCD. This voltage ("pulse height") is proportional to the energy of the incident X-ray. In order to determine the true pulse height corresponding to the input X-ray energy, it is necessary to subtract the *dark levels* and correct possible *optical light leaks*.

Dark levels are non-zero pixel pulse heights caused by leakage currents in the CCD. In addition, optical and UV light might enter the sensor due to imperfect shielding ("light leak"), producing pulse heights that are not related to X-rays. The analysis of *ASCA* SIS data, which utilized an X-ray CCD in photon-counting mode for the first time, showed that the dark levels were different from pixel to pixel, and the distribution of the dark level did not necessarily follow a Gaussian function. On the other hand, light leaks are considered to be rather uniform over the CCD.

For the *Suzaku* XIS, the dark levels and the light leaks are calculated separately in the Normal mode. The dark levels are defined for each pixel and are expected to be constant for a given observation. The PPU calculates the dark levels in the Dark Initial operation; those are stored in the Dark Level RAM. The average dark level is determined for each pixel, and if the dark level is higher than the hot-pixel threshold, this pixel is labeled as a *hot pixel*. The dark levels can be updated by the Dark Update operation, and sent to the telemetry by the Dark Frame mode. The analysis of *ASCA* data showed that the dark levels tend to change mostly during the SAA passage of the satellite. The Dark Update operation is conducted after every SAA passages unless the telescope is pointed toward the day Earth.

Hot pixels are pixels which always output pulse heights larger than the hot-pixel threshold even without input signals. Hot pixels are not usable for observations, and their output has to be disregarded during scientific analysis. The XIS detects hot pixels on-board by the Dark Initial/Update mode, and their positions are registered in the Dark Level RAM. Thus, hot pixels can be recognized on-board, and they are excluded from the event detection processes. It is also possible to specify hot pixels manually. However, some pixels output pulse heights larger than the threshold intermittently. Such pixels are called flickering pixels. It is difficult to identify and remove flickering pixels on board. They are inevitably included in the telemetry and need to be removed in scientific analysis, for example by using the `FTOOLS` `sisclean`. Flickering pixels sometimes cluster around specific columns, which makes them relatively easy to identify.

The light leaks are calculated on board from the pulse height data after subtraction of the dark levels. A truncated average is calculated for 256×114 pixels (this size was 64×64 before January 18, 2006) in every exposure and its running average produces the light leak. In spite of the name, light leaks do not represent in reality optical/UV light leaks in the CCD. They mostly represent fluctuation of the CCD output correlated to the variations of the satellite bus voltage. The XIS has little optical/UV light leak,it is negligible unless the bright earth comes close to the XIS field of view.

The dark levels and the light leaks are merged in the Parallel-sum (P-Sum) mode, so the Dark Update mode is not available in the P-Sum mode. The dark levels, which are defined for each pixel as in the case of the Normal mode, are updated every exposure. It may be considered that the light leak is defined for each pixel in the P-Sum mode.

7.4.2 On-Board Event Analysis

The main purpose of the on-board processing of the CCD data is to reduce the total amount of data transmitted to the ground. For this purpose, the PPU searches for a characteristic pattern of the charge distribution (called an event) in the pre-processed (post dark level and light leak subtraction) frame data. When an X-ray photon is absorbed in a pixel, the photo-ionized electrons can spread into at most four adjacent pixels.

An event is recognized when a pixel has a pulse height which is between the lower and the upper event thresholds and is larger than those of eight adjacent pixels (e.g., it is the peak value in the 3×3 pixel grid). In the P-Sum mode, only the horizontally adjacent pixels are considered. The copied and the dummy pixels ensure that the event search is enabled on the pixels at the edges of each segment. The RAW XY coordinates of the central pixel are considered the location of the event. Pulse-height data for the adjacent 5×5 square pixels (or three horizontal pixels in the P-Sum mode) are sent to the Event RAM as well as the pixel location.

The MPU reads the Event RAM and edits the data to the telemetry format. The amount of information sent to the telemetry depends on the editing mode of the XIS. All the editing modes are designed to send the pulse heights of at least four pixels of an event to the telemetry, because the charge cloud produced by an X-ray photon can spread into at most four pixels. Information of the surrounding pixels may or may not be output to the telemetry depending on the editing mode. The 5×5 mode outputs the most detailed information to the telemetry, i.e., all 25 pulse-heights from the 5×5 pixels containing the event. The size of the telemetry data per event is reduced by a factor of two in the 3×3 mode, and another factor of two in the 2×2 mode. Details of the pulse height information sent to the telemetry are described in the next section.

7.4.3 Discriminators

Three kinds of discriminators, area, grade, and class discriminators, can be applied during the on-board processing. The grade discriminator is available only in the Timing mode. The class discriminator was implemented after the launch of *Suzaku* and was used since January, 2006. In most cases, guest observers need not change the default setting of these discriminators.

The class discriminator classifies the events into two classes, “X-rays” and “others,” and outputs only the ”X-ray” class to the telemetry when it is enabled. This class discriminator is always enabled to reduce the telemetry usage of non-X-ray events. The “other” class is close to, but slightly different from the ASCA grade 7. When the XIS points to a blank sky, more than 90% of the detected events are particle events (mostly corresponding to ASCA grade 7 events). If we reject these particle events on board, we can make a substantial saving in the telemetry usage. This is especially useful when the data rate is medium or low. The class discriminator realizes such a function in a simple manner. When all the eight pixels surrounding the event center exceed the Inner Split Threshold, the event is classified as from the “other” class, and the rest of the events as from the “X-ray” class. With such a simple method, we can reject more than three quarters of the particle events. The class discriminator works only for the 5×5 and 3×3 modes. It is not available in the 2×2 mode and the timing mode.

Fig. 7.5 shows the pixel pattern for which the pulse height or 1-bit information is sent to the telemetry. We do not assign grades to an event on board in the Normal Clock mode. This means that a dark frame error, if present, can be corrected accurately during ground processing even in the 2×2 mode. The definition of the grades in the P-Sum mode is shown in Fig. 7.33.

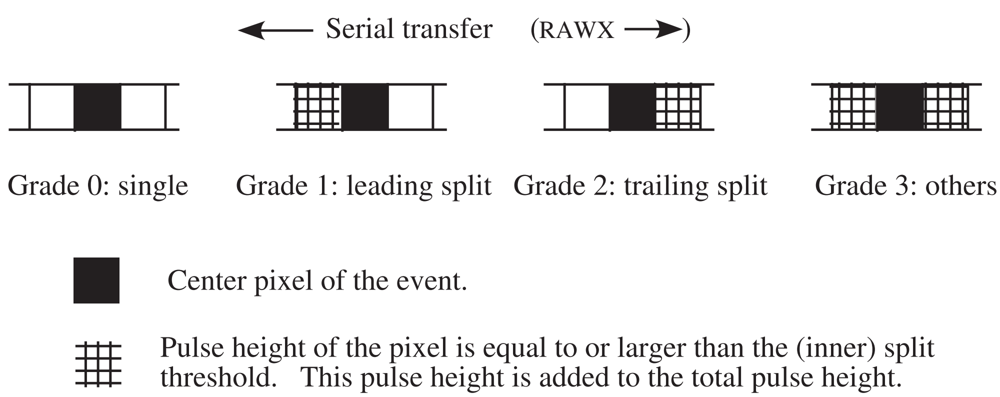

Figure 7.33: Definition of grades in the P-Sum/Timing mode. Total pulse height and the grade of the event are output to the telemetry. Note that the grades are defined referring to the direction of the serial transfer, so the central pixel of the grade 1 event has a *larger* RAW-X value than the second pixel, while the opposite is true for the grade 2 event.

Bibliography

Bautz, M. W., Kissel, S. E., Prigozhin, G. Y., LaMarr, B., Burke, B. E., & Gregory, J. A. 2004, Proc. of SPIE, 5501, 111

Burrows, D. N., Hill, J. E., Nousek, J. A., et al. 2004, Proc. of SPIE, 5165, 201

Burwitz, V., Haberl, F., Neuhäuser, R., Predehl, P., Trümper, J., & Zavlin, V. E. 2003, A&A, 399, 1109

Garmire, G. P., Bautz, M. W., Ford, P. G., Nousek, J. A., & Ricker, G. R., Jr. 2003, Proc. of SPIE, 4851, 28

Ishisaki, Y., et al. 2007, PASJ, 59, 113

Koyama, K., et al. 2007, PASJ, 59, 23

Miller, J. M., et al. 2010, ApJ, 724, 1441

Nakajima, H., et al. 2008, PASJ, 60, 1

Ozawa, M., et al. 2009, PASJ, 61, 1

Plucinsky, P. P., et al. 2008, Proc. of SPIE, 7011,

Serlemitsos, P. J., Soong, Y., Chan, K.-W., et al. 2007, PASJ, 59, 9

Strüder, L., Briel, U., Dennerl, K., et al. 2001, A&A, 365, L18

Tawa, N., et al. 2008, PASJ, 60, 11

Todoroki, S., Kitamoto, S., & Murakami, H. 2012, American Institute of Physics Conference Series, 1427, 251

Turner, M. J. L., Abbey, A., Arnaud, M., et al. 2001, A&A, 365, L27

Tsujimoto, M., et al. 2011, A&A, 525, A25

Uchiyama, H., et al. 2009, PASJ, 61, 9

Yamada, S., et al. 2011, PASJ, in prep.

Chapter 8

Hard X-Ray Detector (HXD)

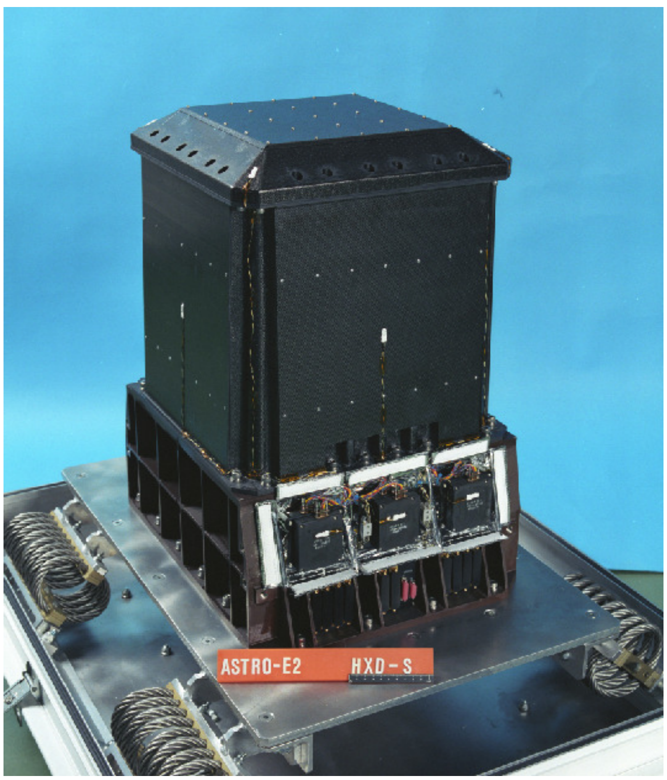

Figure 8.1: The Hard X-ray Detector before installation.

The Hard X-ray Detector (HXD, see Figure 8.1) is a non-imaging, collimated hard X-ray scintillating instrument sensitive in the $\sim 10\,\mathrm{keV}$ to $\sim 600\,\mathrm{keV}$ band. It has been developed jointly by the University of Tokyo, Aoyama Gakuin University, Hiroshima University, ISAS/JAXA, Kanazawa University, Osaka University, Saitama University, SLAC, and RIKEN. Its main purpose is to extend the bandpass of the *Suzaku* observatory to the highest feasible energies, thus allowing broad-band studies of celestial objects.

This AO-7 document is based on the calibration of the PIN and the GSO detectors as of October 2010 (`HEASOFT` 6.9). The recommended procedure for feasibility simulations is basically unchanged from previuos AOs, the same response and background files as provided for AO-6 can be used for simulations. Note that the HXD aim point is not supported anymore (see chapter 2 and section 5.5.2).

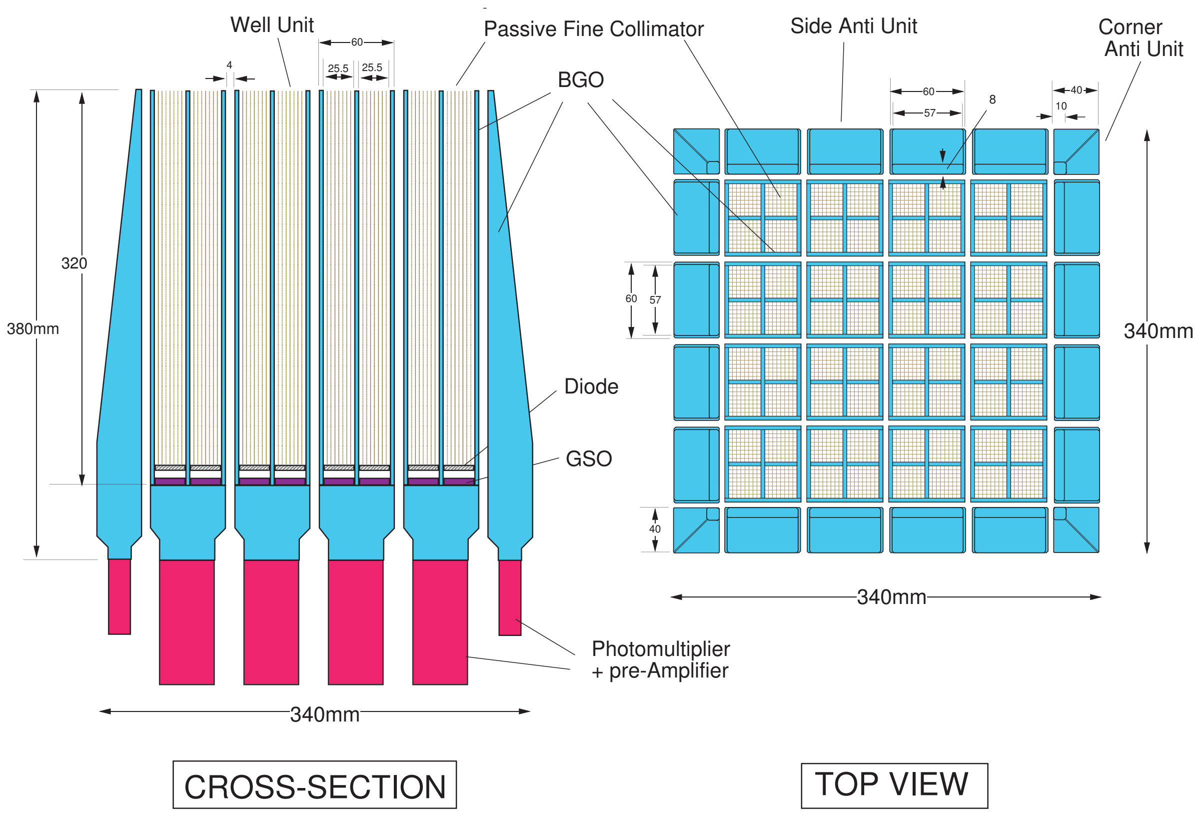

Figure 8.2: Schematic picture of the HXD instrument, which consists of two types of detectors: the PIN diodes located in the front of the GSO scintillator, and the scintillator itself.

The HXD sensor (HXD-S) is a compound-eye detector instrument, consisting of 16 main detectors (arranged as a 4 × 4 array) and the surrounding 20 crystal scintillators for active shielding. Each unit actually consists of two types of detectors: a GSO/BGO phoswich counter, and 2 mm-thick PIN silicon diodes located inside the well, but in front of the GSO scintillator. The PIN diodes are mainly sensitive below ∼ 60 keV, while the GSO/BGO phoswich counter (scintillator) is sensitive above ∼ 40 keV. The scintillator signals are read out by photomultiplier tubes (PMTs). A schematic drawing of the HXD is given in Fig. 8.2. The HXD features an effective area of $\sim 160\,\mathrm{cm}^2$ at 20 keV, and $\sim 260\,\mathrm{cm}^2$ at 100 keV (Fig. 3.5). The energy resolution ~ 4.5 keV (FWHM) for the PIN diodes, and $7.6/\sqrt{E}$ % (FWHM) for the scintillators, where E is energy in MeV. The HXD time resolution is 61 μs.

8.1 GSO/BGO Counter Units

Each main detector unit is of a well-type design with active anti-coincidence shields. The shields and the coarse collimator itself are made of Bismuth Germanate (BGO, $Bi_4Ge_3O_{12}$) crystals, while the X-ray sensing material "inside the well" consists of Gadolinium Silicate (GSO, Gd_2SiO_5(Ce)) crystals. The aspect ratio of the coarse collimators yields an acceptance angle for the GSO of 4.5° (FWHM). Each unit forms a 2×2 matrix, containing four 24 mm × 24 mm, 5 mm thick GSO crystals, each placed behind a PIN diode. BGO crystals are also placed underneath of the GSO sensors, and thus each well is a five-sided anti-coincidence system. The effective thickness of the BGO active shield is about 6 cm for any direction from the PIN and GSO, except for the pointing direction.

The reason for the choice of the two different crystals for the sensor and the shield is dictated by the large stopping ability of both, yet the very different rise/decay times, of ~ 700 ns for BGO, and ~ 120 ns for GSO, at a working temperature of -20° C. This allows for an easy discrimination of the shield vs. X-ray sensor signals, where a single PMT can discriminate between the two types of scintillators in which an event may have occurred. Any particle events or Compton events that are registered by both the BGO and GSO can be rejected by this phoswich technique, utilizing custom-made pulse-shaping LSI circuits.

In early 2010, a new GSO gain calibration with associated response files has been released. With this update, GSO data become usable down to 50 keV. See the *Suzaku* web pages for more details [1]. Note that proposers do not need to consider the details of the new responses, since the differences to the old ones are minor with respect to performing feasibility simulations (although not negligible in a real data analysis).

8.2 PIN-Si Diodes

The low energy response of the HXD is provided by 2 mm thick PIN silicon diodes, placed in front of each GSO crystal. The geometrical area of the diodes is $21.5 \times 21.5\,\mathrm{mm}^2$, while the effective area is limited to $\sim 16.5 \times 16.5\,\mathrm{mm}^2$ by the guard ring structure. The temperature of the PIN diodes is controlled to be $-15 \pm 3\,^{\circ}$C to suppress electrical noise caused by the leakage current, and they are almost fully depleted by applying a bias voltage

[1] http://heasarc.gsfc.nasa.gov/docs/suzaku/analysis/gso_newgain.html and http://www.astro.isas.jaxa.jp/suzakku/analysis/hxd/gsoarf2/

of 400∼500 V [2]. The PIN diodes absorb X-rays with energies below ∼ 70 keV, but gradually become transparent at harder X-rays, which reach and are registered by the GSO detectors. The X-rays are photoelectrically absorbed in the PIN diodes, and the signal is amplified, converted to digital form, and read out by the associated electronics. The PIN diodes are of course also actively shielded from particle events by the BGO shields, as they are placed inside the deep BGO wells. In addition, in order to reduce contamination by the cosmic X-ray background, passive shields called "fine collimators" are inserted in the well-type BGO collimator above the PIN diodes. The fine collimator is made of 50 μm thick phosphor bronze sheets, arranged to form 8 × 8 square meshes, 3 mm wide and 300 mm long, each.

The lower threshold of the PIN diodes has gradually become higher due to the increase of leakage current by cosmic-ray damage. Updated response files are regularly provided by the HXD team, for well defined "epochs" in time. As of August 2011 calibration epoch 11 is the newest/current one.

8.3 HXD Field of View

The field of view of the HXD changes with incoming energy. Below ∼ 100 keV the passive fine collimators define a $34' \times 34'$ FWHM square opening as shown in Figure 8.3. The narrow field of view compared to the *Beppo*-*SAX*-PDS and *RXTE*-HEXTE experiments is one of the key advantages of HXD observations. Above ∼ 100 keV the fine collimators become transparent and the BGO active collimator defines a $4.5^o \times 4.5\,^o$ FWHM square opening. In summary, the full PIN energy range and the lower quarter of the GSO range have a field of view of $34'$, while the GSO events above ∼ 100 keV have a wider field of view, up to 4.5^o.

8.4 In-Orbit HXD Background

Although the HXD is a non-imaging instrument, its instantaneous background can be reproduced through modeling, without requiring separate off-source observations. The HXD has been designed to achieve an extremely low in-orbit background ($\sim 10^{-4}$ cps cm^{-2} keV^{-1}), based on a combination of novel techniques: (1) the five-sided tight BGO shielding as mentioned above, (2) the use of the 20 shielding counters made of thick BGO crystals which surround the 16 main GSO/BGO counters, (3) sophisticated on-board signal processing and on-board event selection, employing both high-speed parallel hardware circuits in the analog electronics, and CPU-based signal handling in the digital electronics, and (4) the

[2]The bias voltage of one out of four high-voltage units has been reduced to 400 V since 2006 May 29, due to the in-orbit damage of a PIN diode. On October 3, 2006, another bias was also set to 400 V. In total, half of the PIN diodes are operated with a 400 V bias, and the other half with 500 V. This affected the total effective area of the PIN diodes on a ∼ 6% level, only.

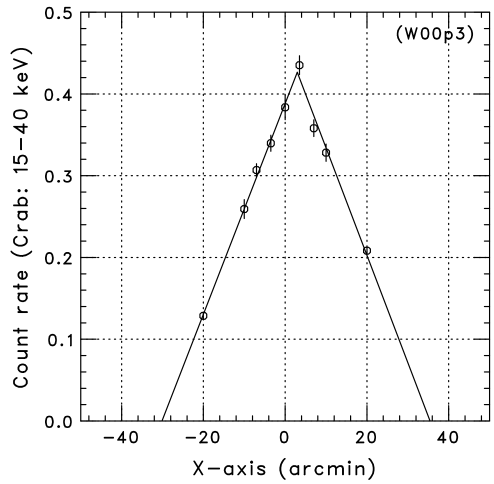

Figure 8.3: Angular response of a single fine-collimator along the satellite X-axis, obtained from offset observations of the Crab nebula.

careful choice of materials that do not become strongly activated under in-orbit particle bombardment. Finally, (5) the narrow field of view below $\sim 100\,\text{keV}$ defined by the fine collimator effectively reduces both the CXB contribution and the source confusion.

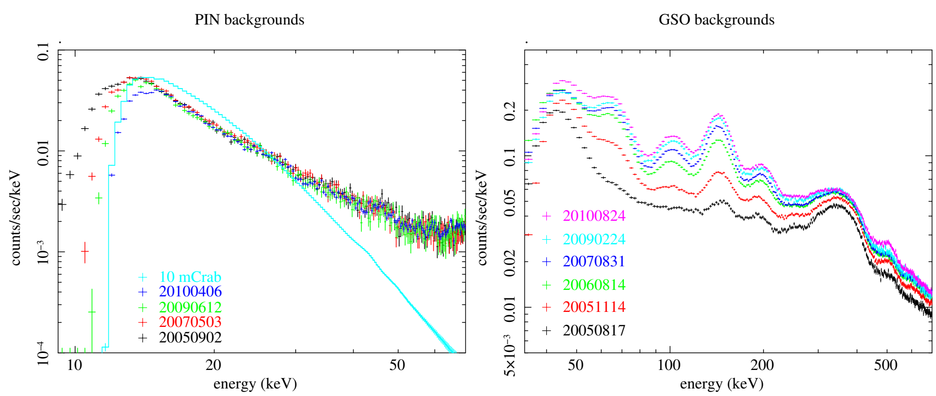

Figure 8.4: [Left] Comparison of average non X-ray background spectra of the PIN, obtained in various epochs. The Crab spectrum, scaled down by two orders of magnitude, is shown as well. [Right] Evolution of average GSO-NXB spectra.

The non X-ray background (NXB) of the PIN diodes, measured in orbit, is plotted in the left panel of Fig. 8.4. The average background count rate summed over the 64 PIN diodes is $\sim$0.6 counts s^{-1}, which is roughly equal to an intensity of 10 mCrab. In addition, almost no long-term growth has been observed in the PIN-NXB during the first three years of *Suzaku*, thanks to the small activation effect of silicon. In contrast, as shown in the right panel of Fig. 8.4, a significant long-term increase caused by in-orbit activation has been observed for the GSO-NXB, especially during the early phase of the mission. The background spectrum of the GSO contains several activation peaks, with intensities exponentially increasing with their half-lives. Since the longest half-life is about one year, the GSO-NXB level will have almost saturated.

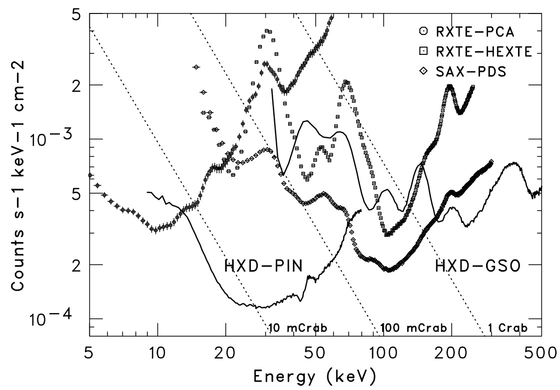

Figure 8.5: Comparison of the in-orbit detector background of the PIN/GSO, normalized by the individual effective areas, with that of the *RXTE*-PCA, *RXTE*-HEXTE, and *BeppoSAX*-PDS. Dotted lines indicate 1 Crab, 100 mCrab, and 10 mCrab intensities.

Figure 8.5 illustrates the comparison between detector backgrounds of several hard X-ray missions. The lowest background level per effective area is achieved by the HXD in an energy range of 12–70 and 150–500 keV. The in-orbit sensitivity of the experiment can be roughly estimated by comparing the background level with celestial source intensities indicated by dotted lines. Below 30 keV, the level is smaller than 10 mCrab, which means a sensitivity better than 0.3 mCrab can be obtained, if an accuracy of 3% is achieved in the background modeling.

Since the long-term variation of both PIN-NXB and GSO-NXB can be expected to be stable, the main uncertainties of the background come from temporal and spectral short-term variations. As shown in Fig. 8.6, the PIN-NXB displays significant short-term variability, with a peak-to-peak amplitude of a factor of 3, anti-correlated with the Cut-Off Rigidity (COR) over the orbit. Since the COR affects the flux of incoming primary cosmic-ray particles, most of the PIN-NXB is considered to originate in the secondary emission produced by interactions between cosmic-ray particles and materials surrounding the detector. When a selection criterion of COR>6, a standard value used in the pipeline processing, is applied for the event extraction, the amplitude decreases to a factor of $\sim$2. During this temporal variation of the PIN-NXB, its spectral shape also changes slightly (larger deviations from the average are observed at a higher energy range, Kokubun et al. 2007). In case of the GSO-NXB the temporal variation differs for different energy bands, as shown in the right panel of Fig 8.6. In the lowest energy range a rapid decline after the SAA passage is clearly observed, in addition to a similar anti-correlation with the COR. All these temporal and spectral behaviors have to be properly handled in the background

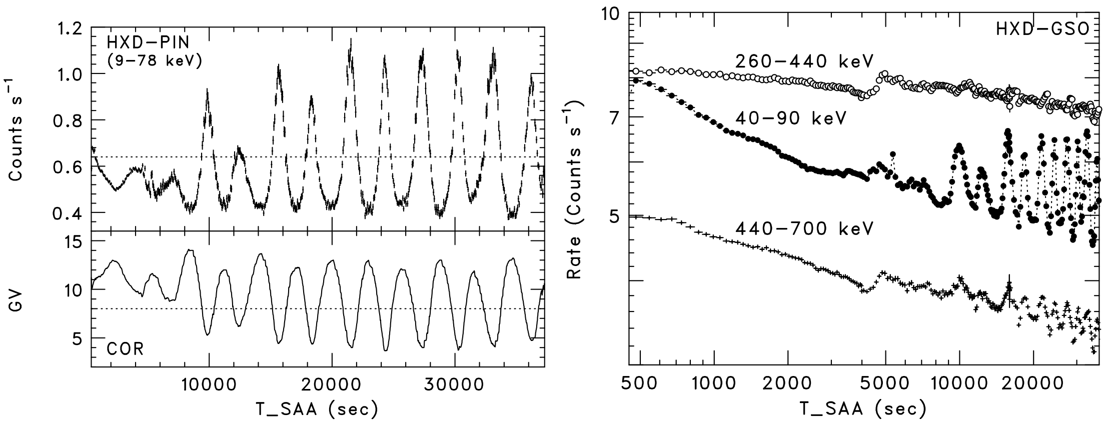

Figure 8.6: [Left] Light curve of the non X-ray background of the PIN, folded with the elapsed time after the SAA passage (*top*), and the average cut-off rigidity at the corresponding position (*bottom*). [Right] The same folded light curves for the GSO background, in the 40–90, 260–440, and 440-700 keV energy bands.

modeling.

8.5 Background Modeling

As is the case for every non-imaging instrument (and in particular, for those sensitive in the hard X-ray range), the limiting factor for the sensitivity of the HXD is the reproducibility of the background estimation. Since this is the first space flight of an HXD-type detector, and the reproduction of the in-orbit background is not at all an easy task, the modeling accuracy evolves with the experience with in-orbit data. The latest status of the estimation procedures and their uncertainties will be regularly posted on the *Suzaku* web-sites listed in Appendix B. For proposal preparation, methods, limitations, and reproducibilities (as a function of time-scale and energy range) of the current background modeling are briefly described below. Note that this document is based on "Suzaku-memo-2008-03" (Mizuno et al. 2008) and "Suzaku-memo-2008-01" (Fukazawa et. al 2008), which can be found at `http://www.astro.isas.jaxa.jp/suzaku/doc/suzakumemo`, and on Fukazawa et. al (2010, PASJ 61, S17). We recommend that proposers properly take into account the expected uncertainties for their observation, based on the following information. Note that all uncertainties are reported at the 90% confidence level in this section.

8.5.1 PIN Background Model

8.5.1.1 Modeling Methods

Since there is a strong anti-correlation between the PIN-NXB and the COR, the background modeling of the PIN is primarily based on the count rate of high-energy charged particles, directly measured by the PIN diodes. Due to large energy deposits in the silicon, penetrations of cosmic-ray particles cause large signals in the corresponding PIN diodes. Hence they activate the Upper Discriminator (UD) in the analog electronics and are then recorded as PIN-UD monitor count in the HK data. The PIN-UD rate is considered to directly indicate the flux of primary cosmic-ray particles. The background count rate at any time can be generally estimated based on the corresponding PIN-UD rate.

In the actual modeling procedure of the so called "tuned-bgd", the PIN-NXB rate is described by adding the raw PIN-UD rate and the integrated PIN-UD rate with a fixed decay time constant, to take into account the small effect of activation during SAA passages. In addition, several parameters such as GSO count rate, Earth elevation angle and cut-off rigidity, are included as input parameters.

The spectral shape of the PIN-NXB is assumed to depend on the COR and the elapsed time after the SAA passage. For each estimated rate it is extracted from a database of PIN-NXB spectra, which has been compiled from Earth occultation data.

8.5.1.2 Comparison With Sky Data

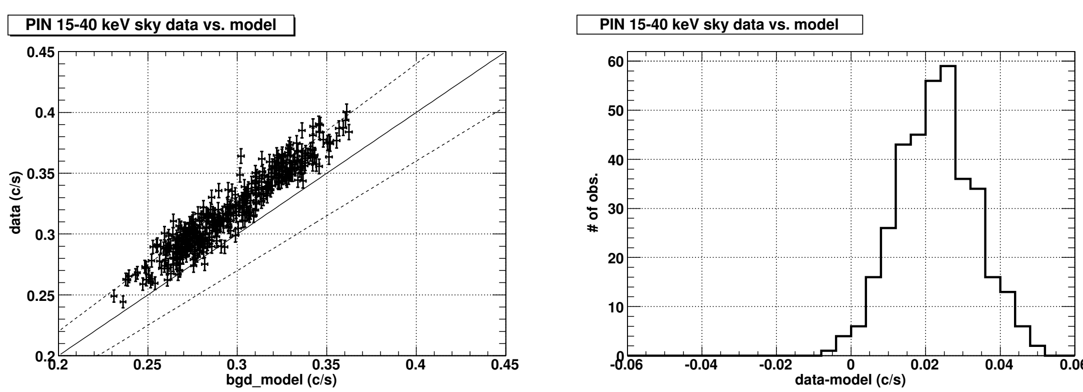

Figure 8.7: Comparison between the data and the NXB model count rate of sky observations with 10 ks integration time in the 15–40 keV band. Observations with no apparent hard X-ray objects in the XIS FOV were selected (see text for details of the data selection).

We first selected observations with no strong X-ray emission above 7 keV (less than 20% above the XIS-FI NXB in the entire XIS field-of-view) and compared the HXD-PIN data and the NXB model count rate (10 ks exposure) in the 15–40 keV band, as shown

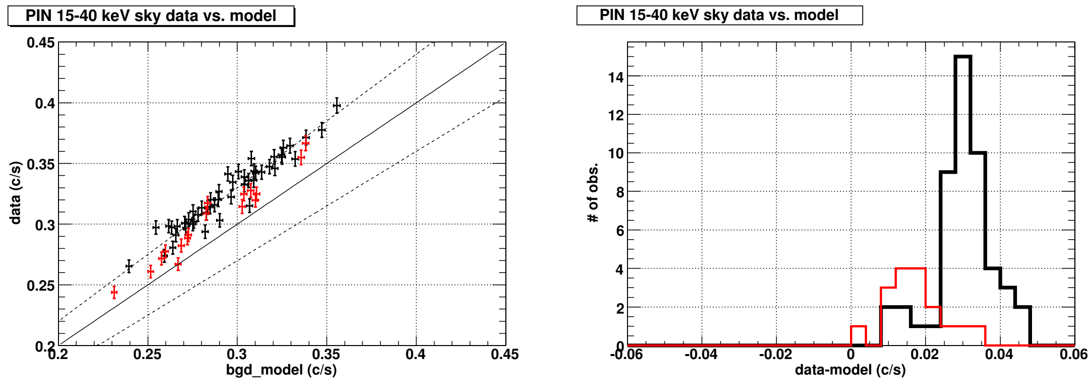

Figure 8.8: The same as Figure 8.7, but for observations of E0102-72 (black) and the Cygnus LOOP (red).

in Figure 8.7. The 90% confidence region (including a statistical uncertainty of $\sim 3.3\%$) of the residual is 5.8% of the mean NXB count rate, which is larger than that obtained from the Earth occultation data ($\sim 3.8\%$ including 3.1% statistical uncertainty, see § 3.2 of "Suzaku-memo-2008-03").

Figure 8.8 shows the same comparison of sky data and the NXB model for E0102−72 observations (the same sky region is observed regularly for XIS calibration purposes). Some observations do not satisfy the selection criteria using XIS due to sources or diffuse emission in the XIS field-of-view, but we used all E0102−72 observations in order to compare sky data and the NXB model for as big a data set as possible. We also plot the data and the NXB model for Cygnus LOOP multi-pointing observations (regions within a radius of 1.5 degrees were observed). We see a clear difference of the residual between the two sets of observations. Especially, the width of the residual for the E0102−72 data is much narrower than that seen in Fig. 8.7.

The 90% confidence region of the residual obtained from the E0102−72 observations is $\pm \sim 0.015$ counts s^{-1}, or $\pm \sim 5\%$ of the mean NXB rate, including the statistical uncertainty of $\sim 3.3\%$. This is somewhat larger, but comparable to, the residual distribution of 3.8% (including the statistical uncertainty of 3.1%) obtained from Earth occultation data. After subtracting the statistical uncertainty, the residual systematic uncertainty of the E0102−72 observations is estimated to be 3.8%, for a typical 10 ks exposure. As described above, the E0102−72 data might suffer from contamination from sources within the field-of-view, and thus this confidence region should be regarded as a conservative estimate. For longer exposures the systematic uncertainty is expected to become a bit smaller, though the lack of long-exposure sample observations makes it difficult to verify this effect at the moment.

In order to check the NXB reproducibility for a sample of observations, we also investigated the background subtraction for eight objects for which the source signal is expected to be negligible in the HXD-PIN. The spectra are summarized in Figure 8.9. The background-subtracted spectra and the CXB model of Boldt (1987) [3] are displayed as blue and green histograms, respectively. No systematic difference between them is seen up to 60 keV.

From these arguments, it is clear that the *current* NXB model reproducibility at the 90% confidence level (excluding the statistical error) is better than 5%, and will be as good as 3% in most observations with exposures longer than 10 ks. When analyzing HXD data, the user should carefully estimate the reproducibility depending on the given observational conditions. For simplicity, we suggest to employ 3% as nominal value of the 15–40 keV PIN NXB reproducibility at the 90% confidence level for the preparation of proposals (see, e.g., section 5.5.2).

8.5.2 GSO Background Model

8.5.2.1 Modeling Methods

The GSO background is higher than that of the PIN, and hence the background modeling accuracy is very important. The background model generation methods are similar to those applied for the PIN background.

8.5.2.2 Comparison With Dark Objects

We compared the NXB model with the on-source data of dark objects, for which the source signal is expected to be negligible in the HXD-GSO. Examples for the comparison of spectra for eight dark objects are summarized in Figure 8.10. Unlike for the PIN, the CXB is negligible in the GSO band. The overall spectral shape is similar between the data and the background model spectra, where the latter is solely based on a template derived from Earth occultation data. In most cases, the residuals amount to 1–1.5% of the data. For simplicity, we therefore suggest to employ 1.5% as nominal value of the GSO NXB reproducibility at the 90% confidence level for the preparation of proposals (see, e.g., section 5.5.2).

8.5.3 Theoretical Sensitivity

As a reference, Fig. 8.11 presents the theoretical sensitivity calculation results, that is, expected sensitivities defined by a certain systematic uncertainty of the background modeling, and those solely determined by the statistical uncertainty for a given exposure. In

[3] The spectral model is given by:
$9.412 \times 10^{-3} \times (E/\mathrm{keV})^{-1.29} \times \exp(-E/40\,\mathrm{keV})$ [photons s^{-1} cm^{-2} keV^{-1} FOV^{-1}]. For more details, see `http://heasarc.gsfc.nasa.gov/docs/suzaku/analysis/abc/node10.html`.

the plot, background reproducibility uncertainties of 3% and 1.5% are assumed as an example, for the PIN and the GSO, respectively. Since the actual statistical and systematic uncertainties that are to be expected for a proposed observation differ from case to case, they should be carefully verified using the data-NXB residual distribution plots.

8.6 Data Analysis Procedure

HXD data are accumulated on event by event basis. After on-board data selection, event data are further screened by the ground pipeline analysis process. By referring to the trigger and flag information (including the inter-unit anti-coincidence hit patterns), the pipeline assigns specific grades to the HXD events such as pure PIN events and pure GSO events. Detector responses and background files that match the particular (i.e., default) grade of events are provided by the HXD team. There are no user-specified parameters for the HXD.

8.7 Wide-Band All-Sky Monitor (WAM)

Tight active shielding of HXD results in a large array of guard counters surrounding the main detector parts. These anti-coincidence counters, made of $\sim 4\,\mathrm{cm}$ thick BGO crystals, have a large effective area for sub-MeV to MeV gamma-rays. With limited angular ($\sim 5^{\mathrm{o}}$) and energy ($\sim$ 30% at 662 keV) resolution, they work as a Wide-band All-sky Monitor (WAM).

Analog signals from normally four counters on each side of an HXD sensor are summed up and a pulse height histogram is recorded every second. If a transient event such as a Gamma-Ray Burst (GRB) is detected, light curves with finer (31.25 ms) time resolution are also recorded in four energy bands. The energy coverage of the WAM extends from $\sim 50\,\mathrm{keV}$ to $\sim 5\,\mathrm{MeV}$, and its effective area is $\sim 800\,\mathrm{cm}^2$ at 100 keV and $400\,\mathrm{cm}^2$ at 1 MeV. These data are shared among the PI and the HXD team, i.e., the PI can use the full WAM data set. Since such transient events, especially GRBs, require immediate distribution to the community, the HXD team will make the analysis products, such as light curves and spectra, public as soon as possible at:
`http://www.astro.isas.jaxa.jp/suzaku/HXD-WAM/WAM-GRB`.

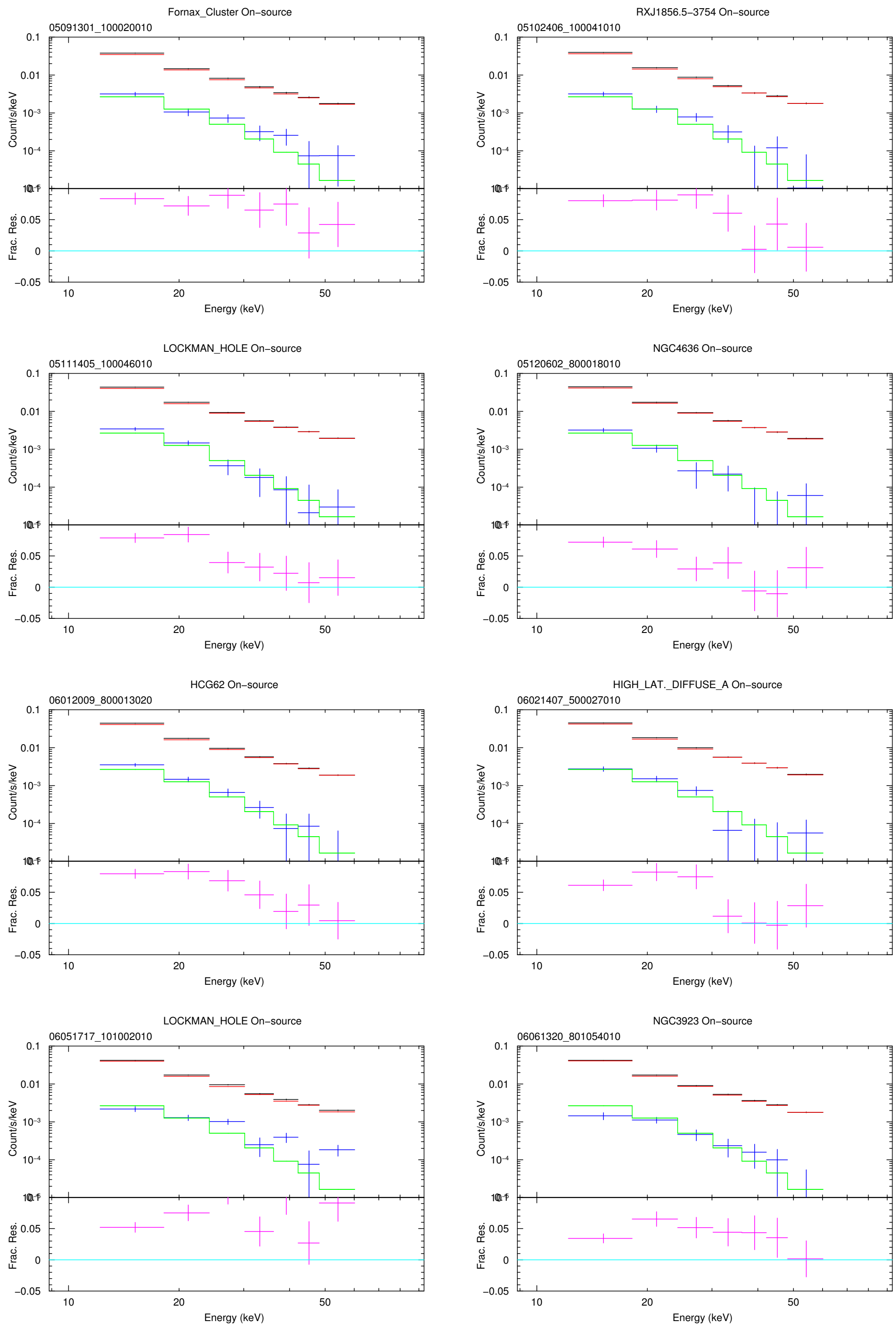

Figure 8.9: Comparison between the measured PIN spectra (black) and the PIN NXB model spectra (red) for observations of objects with no strong hard X-ray contribution. Their fractional residuals are given by purple crosses in the bottom panel of each figure. The blue and green histograms in the top panel indicate the background-subtracted spectrum and the typical CXB spectrum (Boldt 1987), respectively.

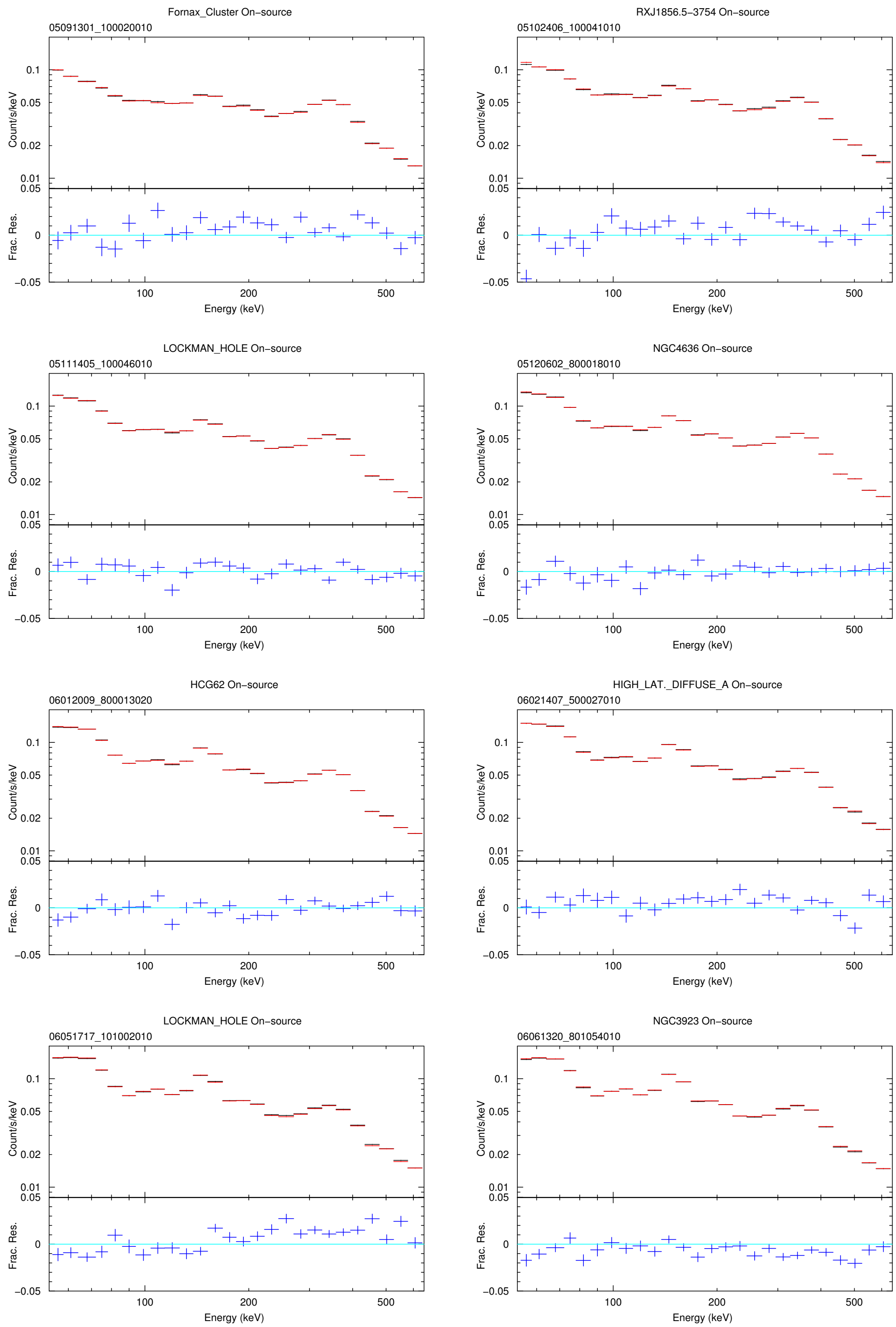

Figure 8.10: Comparison of the GSO spectra between the data (black) and BGD model (red) for observations of objects with no known strong hard X-rays. Their fractional residuals are given by blue crosses.

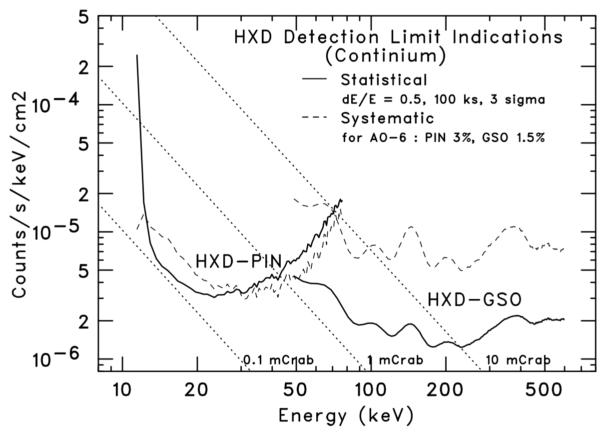

Figure 8.11: Calculated detection limits of the HXD, for continuum measurements. The solid lines denote the statistical 3σ limit for a 100 ks exposure, while the dashed lines show the assumed systematic uncertainties of 3% and 1.5% for the PIN- and GSO-NXB modeling, respectively.

Appendix A

Acronyms

The following table lists acronyms used in this document.

Acronym	Definition
AAVSO	American Association of Variable Stars Observers
AE	Analog Electronics
AO	Announcement of Opportunity
AGN	Active Galactic Nuclei
ARF	Ancillary Response File
ARK	Astrophysics Research Knowledgebase
ASCA	Advanced Satellite for Cosmology and Astrophysics
ASM	All-Sky Monitor (on *RXTE*)
BGD	Background
BGO	Bismuth Germanate
BI	Back-Illuminated
CALDB	Calibration Database
CCD	Charge-Coupled Device
CI	Charge Ingestion
Co-I	Co-investigator
CPU	Central Processing Unit
CTE	Charge Transfer Efficiency
CTI	Charge Transfer Inefficiency
CXB	Cosmic X–ray Background
DDT	Director Discretionary Time
DE	Digital Electronics
Dec	Declination
DP	Data Processor
DSN	Deep Space Network
EA	Effective Area
EEF	Encircled Energy Function
EOB	Extensible Optical Bench
EPIC	European Photon Imaging Camera (on *XMM-Newton*)
ESA	European Space Agency
FI	Front-Illuminated
FWHM	Full-Width Half-Maximum
FITS	Flexible Image Transport System
FOV	Field Of View
FSA	Frame Store Area
FTOOLS	FITS Tools

Acronym	Definition
GO	Guest Observer
GOF	Guest Observer Facility
GRB	Gamma-Ray Burst
GSFC	Goddard Space Flight Center
GSO	Gadolinium Silicate
HEASARC	High Energy Astrophysics Science Archive Research Center
HESS	High Energy Stereoscopic System
HETG	High Energy Transmission Grating (on *Chandra*)
HEXTE	High Energy X-ray Timing Experiment (on *RXTE*)
HPD	Half-Power Diameter
HRI	High Resolution Imager (on *ROSAT*)
HV	High Voltage
HXD	Hard X–Ray Detector
ISAS	Institute of Space and Astronautical Science
INTEGRAL	INTErnational Gamma-Ray Astrophysics Laboratory
JAXA	Japan Aerospace Exploration Agency
LETG	Low Energy Transmission Grating (on *Chandra*)
LSI	Large Scale Integration
MIT	Massachusetts Institute of Technology
MPU	Main Processing Unit
NRA	NASA Research Announcement
NASA	National Aeronautics and Space Administration
NOI	Notice Of Intent
NSPIRES	NASA Solicitation and Proposal Integrated Review and Evaluation System
NXB	Non-X–ray Background
OBF	Optical Blocking Filter
PDS	Phoswich Detector System (on *Bepppo-SAX*)
PH	Pulse Height
PIN	Positive Intrinsic Negative
PI	Principal Investigator
PI	Pulse Invariant
PIMMS	Portable Interactive Multi-Mission Simulator
PM	Photo-Multiplier
PPU	Pixel Processing Unit
PSF	Point Spread Function
PSPC	Position-Sensitive Proportional Counter (on *ROSAT*)
P-Sum	Parallel-Sum
QDE	Quantum Detection Efficiency
RA	Right Ascension
RAM	Random Access Memory
RDD	Residual Dark-current Distribution
RGS	Reflection Grating Spectrometer (on *XMM-Newton*)
RFA	Research Focus Area
RMF	Redistribution Matrix File
ROSAT	RÖntgen SATellite
RPS	Remote Proposal Submission
RXTE	Rossi X-ray Timing Explorer
SAA	South Atlantic Anomaly

Acronym	Definition
SAX	Satellite per Astronomia X
S/C	Spacecraft
SGR	Soft Gamma-ray Repeater
SLAC	Stanford Linear Accelerator Center
SMC	Small Magellanic Cloud
SN	SuperNova
SWG	Science Working Group
TBD	To Be Determined
TCE	TEC Control Electronics
TCU	Thermal Control Unit
TEC	Thermo-Electric Cooler
TOO	Target Of Opportunity
US	United States
USC	Uchinoura Space Center
UV	Ultra Violet
VHS	Very High State
VSNET	Variable Star NETwork
WAM	Wide-band All-sky Monitor
XIS	X–Ray Imaging Spectrometer
XRB	X-ray Binary
XRS	X–Ray Spectrometer
XRT	X–Ray Telescope
XRT-I	X–Ray Telescope for one of the four XIS detectors

Appendix B

Important Web/E-Mail Addresses

Primary *Suzaku* Sites

Japan: `http://www.astro.isas.jaxa.jp/suzaku/`

US : `http://suzaku.gsfc.nasa.gov/`

ESA: `http://www.rssd.esa.int/suzaku`

***Suzaku* GOF:**

`http://suzaku.gsfc.nasa.gov/`

The "Proposal & Tools" button is of particular note.

Tools:

Viewing	`http://heasarc.gsfc.nasa.gov/Tools/Viewing.html`
PIMMS	`http://heasarc.gsfc.nasa.gov/docs/software/tools/pimms.html`
MAKI	`http://heasarc.gsfc.nasa.gov/Tools/maki/maki.html`
XSPEC	`http://heasarc.gsfc.nasa.gov/docs/xanadu/xspec/index.html`
WebPIMMS	`http://heasarc.gsfc.nasa.gov/Tools/w3pimms.html`
WebSPEC	`http://heasarc.gsfc.nasa.gov/webspec/webspec.html`

Questions:

The US GOF can be reached using the web form available at the bottom of every page within the Suzaku GOF site.

Technical Description

Japan: `http://www.astro.isas.jaxa.jp/suzaku/research/proposal/ao7/`

US: `http://suzaku.gsfc.nasa.gov/docs/suzaku/prop_tools/suzaku_td/`

ESA: `http://www.rssd.esa.int/index.php?project=ASTROE2&page=AODocs`

US (ftp): `ftp://legacy.gsfc.nasa.gov/suzaku/nra_info/suzaku_td.ps.gz`

RPS (for Japanese proposals)

`http://rps.astro.isas.jaxa.jp/cgi-bin/RPS/SUZAKU/RPS.pl`

RPS (for US proposals)

`http://heasarc.gsfc.nasa.gov/ark/suzaku/`

RPS (for ESA proposals)

`http://www.rssd.esa.int/RPS/SUZAKU/RPS.pl`

(Or email `rps@rssd.esa.int`)